

DomainCQA: Crafting Expert-Level QA from Domain-Specific Charts

Ling Zhong^{1*} Yujing Lu^{1*} Jing Yang^{1*} Weiming Li^{1*} Peng Wei² Yongheng Wang¹
Manni Duan^{1†} Qing Zhang^{1†}

¹Zhejiang Lab ²National Astronomical Observatory, Chinese Academy of Science

{zhongling, luyujing, yangjing0128, liwm, wangyh, duanmanni, qing.zhang}@zhejianglab.org
weipeng01@nao.cas.cn

Abstract

Chart Question Answering (CQA) benchmarks are essential for evaluating the capability of Multimodal Large Language Models (MLLMs) to interpret visual data. However, current benchmarks focus primarily on the evaluation of general-purpose CQA but fail to adequately capture domain-specific challenges. We introduce DomainCQA, a systematic methodology for constructing domain-specific CQA benchmarks, and demonstrate its effectiveness by developing AstroChart, a CQA benchmark in the field of astronomy. Our evaluation shows that chart reasoning and combining chart information with domain knowledge for deeper analysis and summarization, rather than domain-specific knowledge, pose the primary challenge for existing MLLMs, highlighting a critical gap in current benchmarks. By providing a scalable and rigorous framework, DomainCQA enables more precise assessment and improvement of MLLMs for domain-specific applications.

1. Introduction

The success of Multimodal Large Language Models (MLLMs) has sparked growing interest in their ability to process and analyze scientific charts, which play a crucial role in conveying complex research data. [1, 8, 10, 11, 22, 25, 26, 34, 38]. Among various chart-related tasks, Chart Question Answering (CQA) has emerged as a fundamental challenge, requiring MLLMs to extract, interpret, and reason about chart-based information in response to natural language queries.

However, a key open question remains: *Do these models truly engage with the content of the chart, or do they rely on superficial correlations?* Addressing this uncertainty requires a well-designed benchmark that systematically evaluates the capability of models in chart interpretation, nu-

merical reasoning, and insight derivation.

Existing CQA benchmarks are mostly general-purpose. FigureQA [17], DVQA [16], LEAF-QA [6], and PlotQA [33] predominantly feature basic chart types, such as bar chart, line chart, and scatter chart, limiting both the variety of visual representations and the complexity of question design. While CharXiv [39] and SciCap [15] expand chart diversity by collecting charts from scientific papers, their questions remain focused on visual recognition and basic comprehension, without requiring advanced reasoning or domain knowledge. These benchmarks overlook the significant differences in charts across domains and the crucial role of domain knowledge in CQA. A comprehensive benchmark assesses not only chart recognition but also advanced analytical reasoning and inference. To our knowledge, no comprehensive CQA benchmark specifically evaluates MLLMs on scientific chart interpretation within a specialized domain.

To bridge this gap, we introduce **DomainCQA**, a methodology for building domain-specific CQA benchmarks, which can be applied to fields such as astronomy, biology, geophysics, etc. DomainCQA follows a structured approach to benchmark construction, consisting of three key steps: chart selection, question-answer pair generation, and benchmark quality assurance. The benchmark includes two types of question-answer (QA) pairs: fundamental question-answer (FQA) pairs, which assess MLLMs' general chart interpretation skills, and advanced question-answer (AQA) pairs, which evaluate enhanced domain-specific reasoning. Charts are carefully selected based on complexity and relevance to ensure a well-balanced dataset. Diverse QA pairs are then systematically generated from these charts. Finally, DomainCQA uses a crowdsourced evaluation framework to validate the QA pairs, ensuring high quality.

To demonstrate its effectiveness, we construct an astronomical benchmark called **AstroChart** using the DomainCQA methodology, tailored for the astronomy domain. AstroChart comprises 560 charts and 1,890 QA pairs, in-

*Equal contribution

†Corresponding author

cluding 1509 FQA pairs focused on graphical interpretation and 381 AQA pairs assessing knowledge-based interpretation. We evaluate 17 state-of-the-art (SOTA) MLLMs on this benchmark to measure their ability to interpret astronomical charts, with further analysis of successes and failure patterns.

Our contributions include: (1) proposing DomainCQA, a general methodology for constructing domain-specific Chart QA benchmarks with a three-phase pipeline; (2) introducing AstroChart, the first domain-specific CQA benchmark for astronomy; (3) conducting a comprehensive evaluation of 17 SOTA MLLMs on AstroChart to assess their chart understanding capabilities; and (4) revealing chart reasoning and combining chart information with domain knowledge for deeper analysis and summarization as the primary challenges in domain-specific chart understanding. The AstroChart benchmark is publicly available at [HuggingFace Dataset](#).

2. Related Work

Here we provide an overview of MLLMs’ progress in chart understanding and examine existing CQA benchmarks, highlighting their limitations in evaluating domain-specific scientific chart interpretation.

2.1. MLLMs for Chart Understanding

Recent advancements in MLLMs have significantly improved the ability of chart understanding. These developments span both proprietary and open-source models, each introducing unique enhancements.

Proprietary MLLMs such as GPT-4o[1], Claude 3.5[3], Qwen-VL[4], and GLM-4V[12] have demonstrated strong performance in chart interpretation and multimodal reasoning. The exact techniques used to enhance chart understanding remain proprietary, but their capabilities indicate that training on chart-specific datasets [32], exposure to structured financial and scientific visualizations [46], and leveraging multimodal alignment strategies [45] could significantly improve performance. Despite these strengths, challenges persist in visual-numerical comprehension and cross-modal reasoning.

Open-source MLLMs are advancing rapidly, providing researchers and developers with accessible and customizable alternatives to proprietary models. These models can be broadly divided into two categories: those that enhance general vision-language capabilities and those that specialize in chart-specific understanding.

Vision-Language Advances: mPLUG-Owl[42–44], SPHINX[22], and LLaVA[25–27] enhance vision-language alignment through vision-language projectors. InternVL[10] improves vision encoding to narrow the performance gap between open-source and proprietary models. CogVLM[14, 38] refines feature fusion, while

MiniCPM[41] optimizes efficiency for edge applications. At large scale, Pixtral Large[2] stands as the most powerful open-source MLLM for general vision tasks and high-quality chart interpretation.

Chart-Specific MLLMs: Models such as UniChart[30], ChartLlama[13], Matcha[23], ChartInstruct[31], ChartAssistant[32], and TinyChart[45] are MLLMs specifically designed for chart understanding. These models fine-tune vision-language architectures with large-scale chart instruction data[13, 31, 32], optimizing structured insight extraction from visualized data. Among them, TinyChart employs Program-of-Thought (PoT) reasoning to enhance numerical comprehension, achieving strong performance in chart-related tasks despite its compact 3-billion-parameter size.

2.2. Benchmarks for CQA Evaluation

A CQA benchmark consists of two key components: charts and corresponding QA pairs, both essential for evaluating the chart comprehension capabilities of a model.

Initial efforts in CQA benchmarking focused on synthetic charts, with datasets such as DVQA[16] and FigureQA[17] generating both chart structures and underlying data synthetically. Subsequently, PlotQA[33], LEAF-QA[6], and LEAF-QA++[37] began using real-world numerical data while still relying on synthetic chart visualizations. In both cases, QA pairs were generated using fixed templates, limiting linguistic diversity and natural language variability.

A shift toward real-world chart datasets emerged with ChartQA[29], OpenCQA[18], MMC-Benchmark[24], and CharXiv[39], which introduced charts sourced from real-world datasets. These benchmarks cover a wide range of standard scientific chart types. To improve question diversity, they adopted human-authored QA pairs, with OpenCQA pioneering open-ended CQA, where models generate free-form answers instead of selecting from predefined choices. With the advancement of LLMs, some studies have even leveraged them to generate diverse, high-quality, open-ended QA pairs, such as SciGraphQA[20] and ChartX[40].

Despite these efforts, existing benchmarks primarily focus on general-purpose or broad scientific content, making them insufficient for evaluating MLLMs’ ability to interpret domain-specific scientific charts. This gap underscores the need for dedicated benchmarks tailored to specialized fields, which we address in the next section.

3. Building a Domain CQA Benchmark

We propose DomainCQA, a methodology for constructing domain-specific CQA benchmarks. It provides a structured approach for developing benchmarks tailored to different

scientific domains. DomainCQA categorizes QA pairs into two types:

- **Fundamental Question-Answer (FQA) Pairs:** Corresponding to QA pairs in existing general-purpose CQA benchmarks, evaluating basic chart comprehension and reasoning skills.
- **Advanced Questions-Answer (AQA) Pairs:** Designed to assess MLLMs’ ability to interpret complex encodings, recognize non-trivial trends, and understand domain-specific notations in charts.

This approach ensures that the developed benchmarks evaluate both basic chart comprehension and domain-specific reasoning, providing a robust assessment of MLLMs’ scientific chart understanding.

In summary, DomainCQA follows a structured process consisting of chart selection, question-answer pair generation, and benchmark quality assurance. Fig. 1 provides an overview of the benchmark construction process.

3.1. Chart Selection

DomainCQA selects charts separately for FQA pairs and AQA pairs, ensuring that each set aligns with the specific evaluation requirements of its question type.

Charts for FQA pairs are randomly sampled from domain-related scientific publications, including peer-reviewed journal articles, conference proceedings, and research preprints, to construct a dataset that represents the diversity of scientific visualizations in the domain.

This random sampling is designed to preserve the complexity distribution of charts found in this domain’s publications, ensuring that the dataset reflects the real-world difficulty levels encountered in scientific literature. Maintaining this distribution is crucial for evaluating MLLMs in a setting that aligns with actual domain-specific chart interpretation challenges.

Specifically, we follow a three-step chart selection process:

1. **Chart collection:** We compile a comprehensive set of charts from scientific publications in the domain, filtering out non-informative visualizations (such as decorative figures and flowcharts) to retain only data-driven charts relevant to scientific analysis.
2. **Complexity quantification:** To calculate chart complexity, we introduce the Chart Complexity Vector (CCV), which evaluates a chart across ten key aspects of complexity: {Annotation, Color, Legend, Pattern} (visual complexity), {Axis, Element, Formula, Scale} (data interpretation complexity), and {Subplot, Type} (structural complexity). Each aspect is assigned a binary score of either 0 (simple) or 1 (complex). For example, in the Type aspect, common chart types such as bar, line, and scatter plots are assigned a score of 0, while less common and more intricate chart types receive a score of 1.

As a result, the complexity of a chart is represented as a ten-dimensional binary vector. The definition and examples of CCV scoring can be found in Appendix A.1 and Appendix A.3.

3. **Chart sampling:** We apply Gibbs sampling[5], a Markov Chain Monte Carlo method, to select charts while preserving the original complexity distribution. This iterative process progressively refines the selection, ensuring that the sampled charts retain the same complexity characteristics as those observed in the domain while minimizing unintended biases.

The detailed procedure of charts for FQA pairs selection is outlined in Algorithm 1.

Algorithm 1 Gibbs sampling for chart selection in FQA pairs

Require: Chart dataset D from a domain’s scientific publications with precomputed $CCV(c)$ for each chart c in D

Ensure: Selected benchmark charts S

- 1: **Initialize:** Randomly select an initial set $S \subset D$ of size $target_size$
 - 2: **repeat**
 - 3: **for** each chart $c^* \in S$ **do**
 - 4: Select an aspect α in CCV
 - 5: Fix all other aspects and sample a new value $v \sim P(\alpha|S, D)$
 - 6: Find a candidate chart $c_{new} \in D$ where $\alpha(c_{new}) = v$
 - 7: **if** $CCV(S \cup \{c_{new}\} - \{c^*\})$ maintains distribution **then**
 - 8: Replace c^* with c_{new} in S
 - 9: **end if**
 - 10: **end for**
 - 11: **until** convergence (complexity distribution stabilizes)
- return** S
-

Charts for AQA pairs are inherently more complex than those for FQA pairs, as they require specialized domain knowledge for accurate interpretation. To investigate this complexity, we conduct an experiment to assess whether randomly selected charts can effectively produce high-quality AQA pairs.

From 20 randomly selected astronomical charts, we generate 20 AQA pairs using MLLM, while incorporating the corresponding paper’s contextual content as background knowledge. To assess their quality, we conduct an evaluation study with four domain experts, where each expert independently rates all 20 AQA pairs based on two key criteria:

1. **Professional:** The question is clearly phrased and requires expert-level domain knowledge to answer.
2. **Accuracy:** The AI-generated answer is scientifically ac-

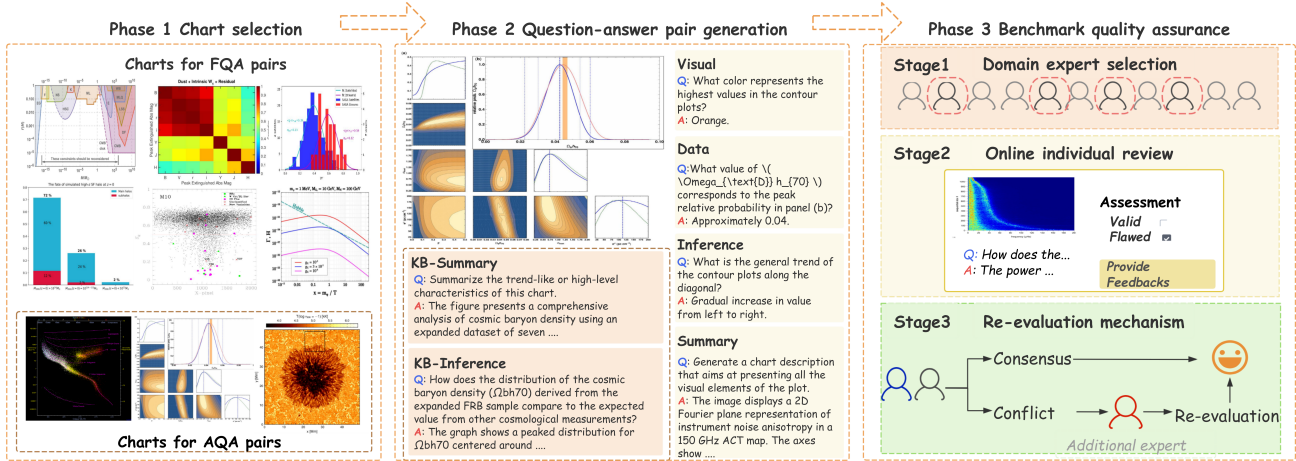


Figure 1. The construction of the DomainCQA benchmark follows a three-step pipeline: **Chart selection:** FQA pairs charts are randomly sampled from scientific publications while maintaining domain complexity, whereas AQA pairs charts are key ‘chart abstracts’ identified using Chain-of-Thought (CoT) reasoning and a Voting Schema (VoT). **Question-answer pair generation:** We generate FQA pairs and AQA pairs by leveraging charts and MLLMs. **Benchmark quality assurance:** All question-answer pairs are reviewed through a structured expert evaluation process, ensuring accuracy through independent assessment and consensus-based refinement.

curate and aligned with domain knowledge.

Inter-rater agreement was measured using Krippendorff’s Alpha[19], revealing very low agreement on both aspects (Professional: $\alpha = -0.11$, 95% CI $[-0.46, 0.24]$; Accuracy: $\alpha = 0.01$, 95% CI $[-0.24, 0.21]$). Since the raters are domain experts, this level of disagreement suggests that the generated QA pairs contained inconsistencies or ambiguities that made evaluation difficult according to a consistent domain standard.

Obviously, this inconsistency or ambiguity stems from the selected charts, as the question-answer pair generation process was identical across all charts. Thus, to ensure the quality of the generated AQA pairs, we aim to select charts that are closely tied to domain knowledge, such as the *chart abstract*, a highly informative visualization that encapsulates the study’s key findings. Fig. 2 is an example of a chart abstract from the field of astronomy and provides the related conclusion corresponding to the chart.

To locate the chart abstract of a paper using MLLMs, we employ a Chain-of-Thought (CoT) reasoning framework combined with a Voting Schema (VoT) to ensure robust and scientifically grounded selection.

In brief, the CoT process begins by extracting the caption of each chart, surrounding description, and key textual sections (e.g., abstract and conclusion). Using this extracted information, the MLLM applies CoT reasoning to generate a concise summary for each chart, as well as the summary of the entire paper. Finally, the best-matching chart is identified by comparing the summary of each chart with the overall summary of the paper.

Selection robustness is further enhanced by integrating

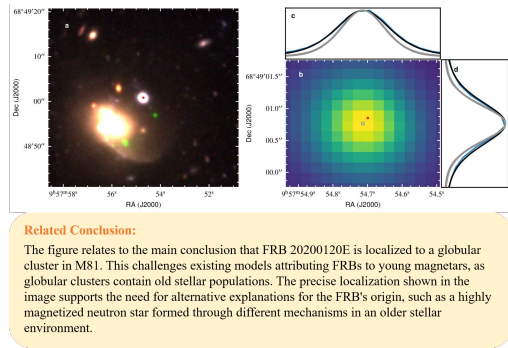


Figure 2. An example of a *chart abstract* from the field of Astronomy.

VoT, where multiple MLLMs independently identify the chart abstract and only the one selected by a majority vote is retained. Algorithm 2 presents the details of the charts for the AQA pairs selection process.

3.2. Question-Answer Pair Generation

We generate two types of QA pairs using MLLMs: FQA pairs and AQA pairs. Specifically, FQA pairs are divided into four categories, and AQA pairs fall into two categories, each derived from their corresponding charts. Below are the details of these types:

- FQA pairs:
 - *Visual:* Assesses the model’s ability to interpret graphical components of the chart.
 - *Data:* Evaluates the model’s ability to retrieve data and perform math reasoning from the chart.

Algorithm 2 CoT&VoT for chart selection in AQA pairs

Require: Research paper P with N charts $\{C_1, C_2, \dots, C_N\}$

Require: Set of k Multimodal Large Language Models (MLLMs) $\{M_1, M_2, \dots, M_k\}$

Ensure: Selected the chart abstract C^* of P

- 1: **for** each MLLM $M_j \in \{M_1, \dots, M_k\}$ **do**
 - 2: Extract abstract and conclusion
 - 3: Generate the paper’s summary P_j with M_j
 - 4: **for** each chart C_i **do**
 - 5: Extract caption and surrounding description
 - 6: Generate its summary S_{ij} using M_j .
 - 7: Compute relevance score R_{ij} based on alignment between S_{ij} and P_j .
 - 8: **end for**
 - 9: Select the most relevant chart, C_j^* based on R_{ij} .
 - 10: **end for**
 - 11: Identify the chart abstract C^* appearing in the majority of $\{C_1^*, \dots, C_m^*\}$ across all models.
 - 12: **return** C^* (final selected chart abstract)
-

- *Inference*: Tests the model’s ability to analyze patterns and relationships in the chart.
- *Summary*: Measures the model’s ability to generate summaries of the chart’s visual elements.
- AQA pairs (Knowledge-Based reasoning tasks):
 - *KB-Inference*: Assesses the model’s ability to apply domain knowledge for deep reasoning and identifying connections in the chart.
 - *KB-Summary*: Evaluates the model’s ability to generate summaries by combining chart information with domain knowledge.

3.3. Benchmark Quality Assurance

To ensure the reliability of the generated benchmark, DomainCQA also implements a systematic *expert verification framework* (Fig. 1, phase 3) that governs the entire process of reviewing and validating every QA pair. This framework defines the review criteria, expert selection process, evaluation workflows, and consensus mechanisms, all of which are implemented through our online assessment platform.

Each QA pair is assessed on the following criteria:

- **Valid**: The question is well-formed and unambiguous, and the provided answer is correct.
- **Flawed**: The question is unclear, or misleading, or the answer contains factual inaccuracies.

Domain experts independently review all QA pairs within the platform. If discrepancies arise, the framework enforces additional rounds of evaluation and refinement until a consensus is reached. By systematically validating every QA pair, we ensure that DomainCQA generates a high standard and valuable benchmark for downstream tasks.

4. AstroChart: First CQA Benchmark for Astronomy

In this section, we apply the DomainCQA methodology to the field of astronomy, leveraging its framework to construct a domain-specific CQA benchmark: *AstroChart*.

AstroChart is a comprehensive and challenging benchmark designed to evaluate chart understanding in astronomy. It consists of 560 astronomical charts and 1,890 QA pairs, providing a rigorous testbed for assessing MLLMs’ multimodal reasoning and scientific chart interpretation capabilities.

4.1. Chart Selection

Charts for FQA pairs: From all astronomical research papers published on arXiv between 2007 and 2023, we initially extracted 513,000 visual assets, excluding those that were unclear or excessively small. We then filtered out non-chart visuals, such as images and diagrams, ultimately retrieving 457,000 scientific charts from these papers. Then with Gibbs sampling, we selected 303 charts for constructing fundamental questions in AstroChart.

Charts for AQA pairs: To identify suitable chart abstracts in astronomy, we focus on high-quality papers, as influential studies often feature well-structured and informative visualizations. To mitigate selection bias, we select the top 1% most-cited papers per year within each of astronomy’s six major subdomains, as shown in Fig. 3. From these selected papers, we extract their chart abstracts using the CoT&VoT method (Algorithm 2) and finally get 257 charts. This process is carried out with voting from two proprietary MLLMs, Claude 3.5 and GPT-4o.

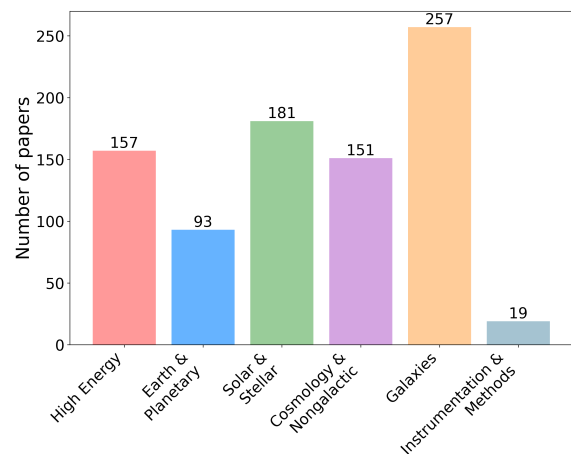


Figure 3. Top 1% most-cited papers selected from six major subdomains of astronomy

In total, AstroChart includes 560 selected charts from

astronomy research, with 303 charts for FQA pairs and 257 charts for AQA pairs. The graphic assets of AstroChart can be found in Appendix B. The overall complexity of each chart is assessed using the L1 norm of its CCV, i.e., the sum of the vector’s elements. Fig. 4 compares the complexity distribution of AstroChart with other generic CQA benchmarks.

Clearly, ChartQA[29], OpenCQA[18], and PlotQA[33] primarily consist of relatively simple charts, with most complexity scores concentrated at lower values. In contrast, CharXiv[39] and AstroChart exhibit broader distributions, with AstroChart containing a higher proportion of complex domain-specific charts, particularly in the 6-10 complexity range. The distribution of CCV scores across ten dimensions in AstroChart can be found in Appendix A.2.

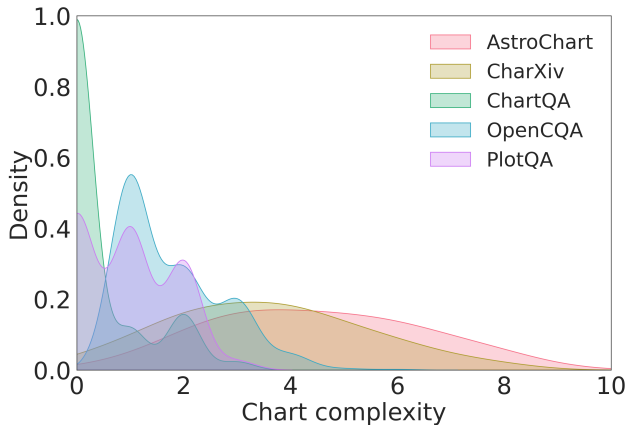


Figure 4. Distribution of chart complexity in benchmarks

4.2. Question-Answer Pair Generation

We use Claude 3.5 to generate question-answer pairs, employing specialized prompts tailored to each category, and ensure the generated question-answer pairs closely aligned with the corresponding charts. Detailed prompt designs are provided in Appendix C.

This process resulted in a total of 1890 QA pairs, including 1509 FQA pairs and 381 AQA pairs. Examples are provided in Appendix D. Tab. 1 presents a detailed distribution of these QA pairs across different categories.

The generated questions exhibit diversity even within a single category. For example, among the 603 FQA pairs in the visual category, 211 focuses on color aspects, 133 addresses structural elements, 213 involves OCR-related inquiries, and 45 pertains to chart-type classification. This variation highlights the range of question types captured within the visual category.

Type of QA Pairs	Category	Aspect	Count
FQA Pairs	Visual	Color	211
		Style	133
		Text	213
		Layout	45
	Data	Point	130
		Interval	102
		Calculation	84
	Inference		289
	Summary		302
AQA Pairs	KB-Inference		200
	KB-Summary		181
Total			1890

Table 1. Number of questions in categories of AstroChart.

4.3. AstroChart Manual Verification

We first check if the selected charts ensure the generation of high-quality AQA pairs. We perform an evaluation on 20 randomly selected AQA pairs with four astronomy experts and assess the agreement using Krippendorff’s Alpha. We notice a great improvement of agreement in both aspects (Professional $\alpha = 0.63$, 95% CI [0.49, 0.74]; Accuracy $\alpha = 0.64$, 95% CI [0.52, 0.75]).

Then, we conduct a comprehensive verification of AstroChart to ensure complete accuracy. Four astronomy experts review all 1,890 QA pairs in AstroChart through our online assessment platform. Each QA pair is independently evaluated by two randomly assigned experts. In case of disagreement, additional evaluation rounds are conducted until a consensus was reached. Details of the online assessment platform can be viewed in Appendix E.

This rigorous validation process ensures reliability of AstroChart, establishing it as a valuable benchmark for assessing MLLM performance in astronomical chart understanding.

5. Evaluation of MLLMs on AstroChart

In this section, we evaluate 17 SOTA MLLMs, including both proprietary and open-source models, on the AstroChart to assess their ability to interpret astronomical charts and reason about complex visual data. We also aim to highlight areas where future models can focus to enhance performance in domain-specific chart understanding.

5.1. Experimental Setup

Models: The proprietary MLLMs include GPT-4o[1], GLM-4V[12], GLM-4V-Plus[12] and Qwen-VL-Max[4]. The open-source MLLMs, ordered by ascending model size, are TinyChart-3B[45], Deepseek-Janus-Pro-7B[7], Llava1.5-7[25], Llava1.6-Mistral-7B[27], Qwen-VL-Chat-7B[4], MiniCPM-Llama3-V2.6-8B[41], InternVL2-8B[11], mPLUG-Owl2-8.2B[44], Llava1.6-

Vicuna-13B[27], SPHINX-v2-13B[22], CogVLM-19B[14], Llava1.6-Yi-34B[27] and Pixtral-large-124B[2]. Detailed information about the architecture of MLLMs can be found in Appendix F.

Setup: All proprietary models are accessed via API, while open-source models are deployed locally and tested on a single Nvidia A100-80G GPU. We conduct a zero-shot evaluation, providing only the chart and question as prompts for each MLLM to answer questions in AstroChart.

Metrics: we use an evaluation framework designed to handle both numerical responses and open-ended responses, the details can be found in Appendix G:

- For numerical responses, we distinguish between data retrieval and data derivation. For data retrieval (e.g., plotted points or data ranges), we normalize the relative error by the axis range, ensuring a bounded and scale-aware evaluation. Data derivation (e.g., the number of bars, colors, or legends, as well as math reasoning) refers to counting visual elements or performing calculations based on the chart, and correctness is determined by exact numerical matching, ensuring that only fully correct answers are considered accurate.
- For open-ended responses, we use an LLM-based judging framework inspired by [28], in which a dedicated judging LLM, separate from the 17 MLLMs used in the evaluation, assesses the quality of answers generated by the evaluated models. The judging LLM assigns a score between 0 and 1 based on predefined assessment criteria, ensuring consistency and scalability in evaluation.

We adopt the aforementioned metrics evaluation framework and use DeepSeek-V3[9] as the LLM to compute LLM-scoring as accuracy to evaluate the performance of 17 MLLMs. Additionally, we employed other metrics such as ROUGE-L[21], BLEU-4[35], and L3Score[36]. As all metrics exhibit a similar overall trend, we omit them due to space constraints; details can be found in Appendix H.

5.2. Results

The evaluation results of MLLMs on AstroChart, including overall scores as well as performance across different categories of FQA pairs and AQA pairs, are presented in Tab. 2. We also provide Failure Cases of AstroChart in Appendix I.

Each score in the table represents the average accuracy for the corresponding class. For simplicity, we omit the percentage symbol and present the values directly in the table and throughout this subsection.

Overall Performance: The results reveal significant performance differences across models, highlighting their strengths and limitations in astronomical chart understanding. GPT-4o achieves the highest score, demonstrating

the superiority of proprietary models, while Pixtral-Large-124B stands out as the best-performing open-source model, even surpassing most proprietary alternatives. TinyChart-3B ranks the lowest, reinforcing the general trend that larger models tend to perform better.

However, model size alone does not fully determine performance. Pixtral-Large-124B’s strong results, despite being smaller than proprietary models, suggest that architectural advancements and targeted optimizations in chart understanding play a crucial role. These findings indicate that while proprietary models still lead, some open-source models are narrowing the gap, and strategic improvements in model design and training could further enhance MLLM performance in astronomical chart interpretation.

Category Performance: The performance of MLLMs across different question categories, including Visual, Data, Inference, and Summary in FQA pairs, as well as KB-Inference and KB-Summary in AQA pairs, reveals notable differences in difficulty and model capabilities. Fig. 5 illustrates the performance distribution of all models across these categories.

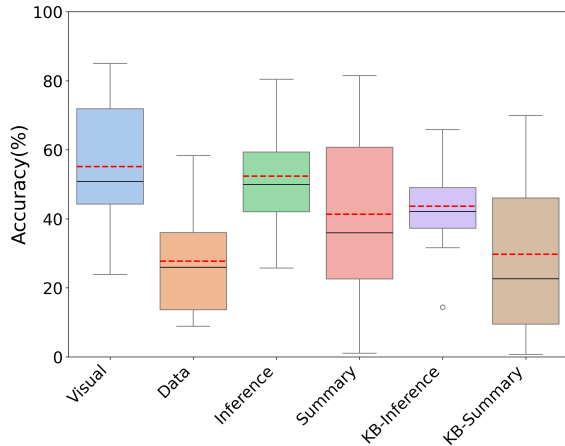


Figure 5. Box plot of accuracy evaluation across six different question categories in AstroChart. Note that the red dashed lines indicate the average accuracy.

Visual questions achieve the highest average accuracy, indicating that models perform relatively well in interpreting graphical components such as colors, styles, text, and layout. This suggests that MLLMs exhibit a strong ability to recognize visual elements and extract fundamental structural information from charts.

Data questions consistently show low performance across all models, as depicted in the box plot. Despite efforts, none of the models perform well in retrieving numerical values or performing math reasoning, with the latter proving even more challenging. This is likely due to factors such as OCR limitations, axis misinterpretation, and difficulties in extracting data from dense or complex charts.

Models	Fundamental Question								Advanced Question				Overall	
	Visual				Data				Inference	Summary	KB-Inference	KB-Summary		
	All	Color	Style	Text	Layout	All	Point	Interval						Calculation
Proprietary Multimodal Large Language Models														
GPT-4o	84.29%	85.54%	82.59%	84.69%	81.33%	56.72%	60.94%	62.64%	42.98%	80.42%	81.46%	65.85%	69.94%	75.31%
GLM-4V	74.88%	77.09%	70.44%	74.84%	78.67%	36.01%	32.54%	46.16%	29.05%	59.34%	63.81%	48.55%	46.02%	58.69%
GLM-4V-Plus	74.64%	77.32%	70.26%	74.84%	74.22%	43.05%	43.55%	50.13%	33.69%	61.56%	60.73%	57.70%	59.45%	61.89%
Qwen-VL-Max	68.83%	72.46%	60.30%	68.73%	76.00%	45.06%	41.13%	48.14%	47.38%	70.00%	77.78%	59.85%	65.41%	65.19%
Open-source Multimodal Large Language Models														
TinyChart-3B	27.79%	45.82%	21.04%	13.57%	28.00%	13.26%	18.35%	11.80%	7.14%	25.74%	1.06%	14.35%	0.72%	16.76%
Deepseek-Janus-Pro-7B	65.88%	73.90%	66.96%	55.92%	72.00%	32.41%	35.51%	38.09%	20.71%	57.85%	52.62%	46.60%	28.67%	51.33%
Llava1.5-7B	23.85%	33.69%	23.85%	12.86%	27.11%	10.87%	11.05%	9.89%	11.79%	42.04%	15.03%	37.25%	9.50%	23.10%
Llava1.6-Mistral-7B	44.56%	58.00%	39.63%	32.54%	49.33%	14.70%	17.68%	11.74%	13.69%	46.89%	22.55%	38.75%	12.49%	32.72%
Qwen-VL-Chat-7B	44.29%	53.43%	40.81%	33.52%	59.11%	13.62%	19.19%	8.22%	11.55%	39.58%	24.54%	31.80%	14.59%	31.12%
MiniCPM-Llama3-V2.6-8B	71.91%	76.24%	69.04%	70.14%	68.22%	33.90%	30.07%	45.23%	26.07%	56.12%	60.73%	49.05%	44.64%	56.32%
InternVL2-8B	48.12%	53.99%	43.85%	43.85%	51.33%	25.94%	25.80%	29.14%	22.26%	49.90%	28.05%	39.40%	7.46%	36.66%
mPLUG-Owl2-8.2B	25.58%	33.74%	25.41%	16.29%	29.11%	9.26%	10.42%	8.45%	8.45%	37.75%	10.30%	32.05%	7.68%	21.24%
Llava1.6-Vicuna-13B	49.45%	65.31%	44.74%	35.96%	50.44%	15.38%	19.99%	10.49%	14.17%	44.15%	24.21%	39.05%	15.25%	34.53%
SPHINX-v2-13B	31.43%	46.64%	29.41%	19.27%	20.89%	8.89%	14.85%	1.47%	8.69%	37.51%	6.59%	31.60%	3.76%	21.99%
CogVLM2-19B	65.70%	73.97%	50.56%	65.92%	70.89%	30.60%	32.78%	38.91%	17.14%	53.49%	56.92%	44.80%	33.76%	51.29%
Llava1.6-Vi-34B	50.81%	66.10%	44.22%	39.48%	50.22%	23.17%	22.04%	25.86%	21.67%	47.99%	35.93%	42.10%	22.65%	39.76%
Pixtral-large-124B	85.03%	84.74%	82.67%	86.38%	86.89%	58.34%	61.21%	64.09%	46.90%	79.72%	79.97%	62.95%	63.76%	74.57%

Table 2. Accuracy evaluation on AstroChart benchmark. Bold numbers indicate the best-performing model among proprietary and open-source MLLMs, respectively.

This persistent low accuracy underscores that precise data retrieval remains a significant challenge for MLLMs, particularly in astronomy, where charts often feature non-trivial axis scales and complex visual encodings.

The scores for Inference and KB-Inference are quite similar across models, suggesting that most MLLMs, regardless of size, have enough domain knowledge to perform these tasks effectively. The presence of domain knowledge in the questions may help larger models focus on relevant knowledge areas, leading to consistent and accurate answers. While proprietary models and larger open-source models, such as Pixtral-Large-124B, achieve higher scores due to stronger contextual reasoning and multimodal alignment, even smaller models like Deepseek-Janus-Pro-7B perform well, showing low variance in their results (Fig. 6 top).

KB-Summary exhibits moderately lower performance than Summary. This suggests that it is challenging for models to extract information from charts while also identifying and retrieving relevant domain-specific knowledge. Proprietary and larger open-source models, benefiting from richer training data and stronger multimodal alignment, still perform better overall, but the gap between KB-Summary and Summary indicates the complexity of combining chart interpretation with domain knowledge without explicit textual cues (Fig. 6 bottom).

5.3. Discussion

Our results indicate that current MLLMs struggle with combining chart information with specific domain knowledge for more comprehensive analysis and accurate summarization without textual cues. In addition, issues with data retrieval and math reasoning need improvement. Therefore, to enhance MLLMs’ capabilities, the focus should be mainly on improving their data processing abilities and integrating

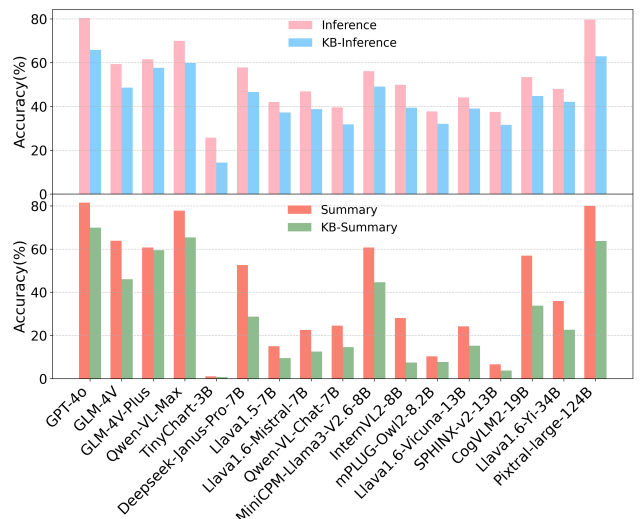


Figure 6. Accuracy of MLLMs on different evaluation categories: Inference vs. KB-Inference and Summary vs. KB-Summary in AstroChart.

chart and domain knowledge for more effective analysis and summarization.

6. Conclusion & Future Work

This paper introduced DomainCQA, a structured methodology for constructing domain-specific CQA benchmarks, and applied it to develop AstroChart, the first Chart QA benchmark for astronomy. Through a comprehensive evaluation of 17 SOTA MLLMs, we identified chart reasoning and the combination chart information with domain knowledge for deeper analysis and summarization as the primary bottlenecks in domain-specific chart understanding. While these models exhibit strong general reasoning

abilities, they struggle with deciphering complex visual encodings, performing numerical reasoning, and integrating domain knowledge to derive meaningful conclusions.

Future work will expand DomainCQA to include domains like biology, physics, and materials science, while exploring advanced multimodal training and dataset augmentation to enhance MLLMs' ability to process and reason with complex visual data.

References

- [1] Josh Achiam, Steven Adler, Sandhini Agarwal, Lama Ahmad, Ilge Akkaya, Florencia Leoni Aleman, Diogo Almeida, Janko Altenschmidt, Sam Altman, Shyamal Anadkat, et al. GPT-4 technical report. *arXiv preprint arXiv:2303.08774*, 2023. 1, 2, 6
- [2] Pravesh Agrawal, Szymon Antoniak, Emma Bou Hanna, Baptiste Bout, Devendra Chaplot, Jessica Chudnovsky, Diogo Costa, and et al. Baudouin De Monicault. Pixtral 12b, 2024. 2, 7
- [3] Anthropic. The claude 3 model family: Opus, Sonnet, Haiku, 2024. 2
- [4] Jinze Bai, Shuai Bai, Shusheng Yang, Shijie Wang, Sinan Tan, Peng Wang, Junyang Lin, Chang Zhou, and Jingren Zhou. Qwen-VL: A versatile vision-language model for understanding, localization, text reading, and beyond. *arXiv preprint arXiv:2308.12966*, 2023. 2, 6
- [5] George Casella and Edward I. George. Explaining the gibbs sampler. *The American Statistician*, 46:167–174, 1992. 3
- [6] Ritwick Chaudhry, Sumit Shekhar, Utkarsh Gupta, Pranav Maneriker, Prann Bansal, and Ajay Joshi. Leaf-qa: Locate, encode & attend for figure question answering. In *2020 IEEE Winter Conference on Applications of Computer Vision (WACV)*, pages 3501–3510, 2020. 1, 2
- [7] Xiaokang Chen, Zhiyu Wu, Xingchao Liu, Zizheng Pan, Wen Liu, Zhenda Xie, Xingkai Yu, and Chong Ruan. Januspro: Unified multimodal understanding and generation with data and model scaling. *arXiv preprint arXiv:2501.17811*, 2025. 6
- [8] Zhe Chen, Weiyun Wang, Hao Tian, Shenglong Ye, Zhangwei Gao, Erfei Cui, Wenwen Tong, Kongzhi Hu, Jiapeng Luo, Zheng Ma, et al. How far are we to GPT-4V? closing the gap to commercial multimodal models with open-source suites. *arXiv preprint arXiv:2404.16821*, 2024. 1
- [9] DeepSeek-AI. Deepseek-v3 technical report, 2024. 7
- [10] Xiaoyi Dong, Pan Zhang, Yuhang Zang, Yuhang Cao, Bin Wang, Linke Ouyang, Xilin Wei, Songyang Zhang, Haodong Duan, Maosong Cao, Wenwei Zhang, Yining Li, Hang Yan, Yang Gao, Xinyue Zhang, Wei Li, Jingwen Li, Kai Chen, Conghui He, Xingcheng Zhang, Yu Qiao, Dahua Lin, and Jiaqi Wang. InternLM-XComposer2: Mastering free-form text-image composition and comprehension in vision-language large model. *arXiv preprint arXiv:2401.16420*, 2024. 1, 2
- [11] Xiaoyi Dong, Pan Zhang, Yuhang Zang, Yuhang Cao, Bin Wang, Linke Ouyang, Songyang Zhang, Haodong Duan, Wenwei Zhang, Yining Li, Hang Yan, Yang Gao, Zhe Chen, Xinyue Zhang, Wei Li, Jingwen Li, Wenhai Wang, Kai Chen, Conghui He, Xingcheng Zhang, Jifeng Dai, Yu Qiao, Dahua Lin, and Jiaqi Wang. InternLM-XComposer2-4KHD: A pioneering large vision-language model handling resolutions from 336 pixels to 4k hd. *arXiv preprint arXiv:2404.06512*, 2024. 1, 6
- [12] Team GLM, Aohan Zeng, Bin Xu, Bowen Wang, Chenhui Zhang, Da Yin, Diego Rojas, Guanyu Feng, Hanlin Zhao, Hanyu Lai, Hao Yu, Hongning Wang, Jiadai Sun, Jiajie Zhang, Jiale Cheng, Jiayi Gui, Jie Tang, Jing Zhang, Juanzi Li, Lei Zhao, Lindong Wu, Lucen Zhong, Mingdao Liu, Minlie Huang, Peng Zhang, Qinkai Zheng, Rui Lu, Shuaiqi Duan, Shudan Zhang, Shulin Cao, Shuxun Yang, Weng Lam Tam, Wenyi Zhao, Xiao Liu, Xiao Xia, Xiaohan Zhang, Xiaotao Gu, Xin Lv, Xinghan Liu, Xinyi Liu, Xinyue Yang, Xixuan Song, Xunkai Zhang, Yifan An, Yifan Xu, Yilin Niu, Yuantao Yang, Yueyan Li, Yushi Bai, Yuxiao Dong, Zehan Qi, Zhaoyu Wang, Zhen Yang, Zhengxiao Du, Zhenyu Hou, and Zihan Wang. Chatglm: A family of large language models from glm-130b to glm-4 all tools, 2024. 2, 6
- [13] Yucheng Han, Chi Zhang, Xin Chen, Xu Yang, Zhibin Wang, Gang Yu, Bin Fu, and Hanwang Zhang. Chartllama: A multimodal llm for chart understanding and generation, 2023. 2
- [14] Wenyi Hong, Weihang Wang, Ming Ding, Wenmeng Yu, Qingsong Lv, Yan Wang, Yean Cheng, Shiyu Huang, Junhui Ji, Zhao Xue, et al. Cogvlm2: Visual language models for image and video understanding. *arXiv preprint arXiv:2408.16500*, 2024. 2, 7
- [15] Ting-Yao Hsu, C Lee Giles, and Ting-Hao Huang. SciCap: Generating captions for scientific figures. In *Findings of the Association for Computational Linguistics: EMNLP 2021*, pages 3258–3264. Association for Computational Linguistics, 2021. 1
- [16] Kushal Kafle, Brian Price, Scott Cohen, and Christopher Kanan. Dvqa: Understanding data visualizations via question answering. In *Proceedings of the IEEE conference on computer vision and pattern recognition*, pages 5648–5656, 2018. 1, 2
- [17] Samira Ebrahimi Kahou, Adam Atkinson, Vincent Michalski, Ákos Kádár, Adam Trischler, and Yoshua Bengio. FigureQA: An annotated figure dataset for visual reasoning, 2018. 1, 2
- [18] Shankar Kantharaj, Xuan Long Do, Rixie Tiffany Leong, Jia Qing Tan, Enamul Hoque, and Shafiq Joty. OpenCQA: Open-ended question answering with charts. In *Proceedings of the 2022 Conference on Empirical Methods in Natural Language Processing*, pages 11817–11837, Abu Dhabi, United Arab Emirates, 2022. Association for Computational Linguistics. 2, 6
- [19] Klaus Krippendorff. Computing krippendorff's alpha-reliability. 2011. 4
- [20] Shengzhi Li and Nima Tajbakhsh. Scigraphqa: A large-scale synthetic multi-turn question-answering dataset for scientific graphs, 2023. 2
- [21] Chin-Yew Lin. ROUGE: A package for automatic evaluation of summaries. In *Text Summarization Branches Out*, pages

- 74–81, Barcelona, Spain, 2004. Association for Computational Linguistics. 7
- [22] Dongyang Liu, Renrui Zhang, Longtian Qiu, Siyuan Huang, Weifeng Lin, Shitian Zhao, Shijie Geng, Ziyi Lin, Peng Jin, Kaipeng Zhang, Wenqi Shao, Chao Xu, Conghui He, Junjun He, Hao Shao, Pan Lu, Hongsheng Li, Yu Qiao, and Peng Gao. Sphinx-x: Scaling data and parameters for a family of multi-modal large language models, 2024. 1, 2, 7
- [23] Fangyu Liu, Francesco Piccinno, Syrine Krichene, Chenxi Pang, Kenton Lee, Mandar Joshi, Yasemin Altun, Nigel Collier, and Julian Eisenschlos. MatCha: Enhancing visual language pretraining with math reasoning and chart derendering. In *Proceedings of the 61st Annual Meeting of the Association for Computational Linguistics (Volume 1: Long Papers)*, pages 12756–12770, Toronto, Canada, 2023. Association for Computational Linguistics. 2
- [24] Fuxiao Liu, Xiaoyang Wang, Wenlin Yao, Jianshu Chen, Kaiqiang Song, Sangwoo Cho, Yaser Yacoob, and Dong Yu. MMC: Advancing multimodal chart understanding with large-scale instruction tuning. In *Proceedings of the 2024 Conference of the North American Chapter of the Association for Computational Linguistics: Human Language Technologies (Volume 1: Long Papers)*, pages 1287–1310, Mexico City, Mexico, 2024. Association for Computational Linguistics. 2
- [25] Haotian Liu, Chunyuan Li, Yuheng Li, and Yong Jae Lee. Improved baselines with visual instruction tuning, 2023. 1, 2, 6
- [26] Haotian Liu, Chunyuan Li, Qingyang Wu, and Yong Jae Lee. Visual instruction tuning, 2023. 1
- [27] Haotian Liu, Chunyuan Li, Yuheng Li, Bo Li, Yuanhan Zhang, Sheng Shen, and Yong Jae Lee. LLaVA-NeXT: Improved reasoning, ocr, and world knowledge, 2024. 2, 6, 7
- [28] Yang Liu, Dan Iter, Yichong Xu, Shuohang Wang, Ruochen Xu, and Chenguang Zhu. G-eval: NLG evaluation using gpt-4 with better human alignment. In *Proceedings of the 2023 Conference on Empirical Methods in Natural Language Processing*, pages 2511–2522, 2023. 7
- [29] Ahmed Masry, Xuan Long Do, Jia Qing Tan, Shafiq Joty, and Enamul Hoque. ChartQA: A benchmark for question answering about charts with visual and logical reasoning. In *Findings of the Association for Computational Linguistics: ACL 2022*, pages 2263–2279, Dublin, Ireland, 2022. Association for Computational Linguistics. 2, 6
- [30] Ahmed Masry, Parsa Kavehzadeh, Xuan Long Do, Enamul Hoque, and Shafiq Joty. UniChart: A universal vision-language pretrained model for chart comprehension and reasoning. In *Proceedings of the 2023 Conference on Empirical Methods in Natural Language Processing*, pages 14662–14684, Singapore, 2023. Association for Computational Linguistics. 2
- [31] Ahmed Masry, Mehrad Shahmohammadi, Md Rizwan Parvez, Enamul Hoque, and Shafiq Joty. ChartInstruct: Instruction tuning for chart comprehension and reasoning. In *Findings of the Association for Computational Linguistics: ACL 2024*, 2024. 2
- [32] Fanqing Meng, Wenqi Shao, Quanfeng Lu, Peng Gao, Kaipeng Zhang, Yu Qiao, and Ping Luo. Chartassistant: A universal chart multimodal language model via chart-to-table pre-training and multitask instruction tuning. In *Findings of the Association for Computational Linguistics: ACL 2024*, pages 7775–7803, Bangkok, Thailand, 2024. Association for Computational Linguistics. 2
- [33] Nitesh Methani, Pritha Ganguly, Mitesh M. Khapra, and Pratyush Kumar. Plotqa: Reasoning over scientific plots. In *The IEEE Winter Conference on Applications of Computer Vision (WACV)*, 2020. 1, 2, 6
- [34] Aitor Ormazabal, Che Zheng, Cyprien de Masson d’Autume, Dani Yogatama, Deyu Fu, Donovan Ong, Eric Chen, Eugenie Lamprecht, Hai Pham, Isaac Ong, et al. Reka Core, Flash, and Edge: A series of powerful multimodal language models. *arXiv preprint arXiv:2404.12387*, 2024. 1
- [35] Kishore Papineni, Salim Roukos, Todd Ward, and Wei-Jing Zhu. Bleu: a method for automatic evaluation of machine translation. In *Proceedings of the 40th Annual Meeting of the Association for Computational Linguistics*, pages 311–318, Philadelphia, Pennsylvania, USA, 2002. Association for Computational Linguistics. 7
- [36] Shraman Pramanick, Rama Chellappa, and Subhashini Venugopalan. Spiqa: A dataset for multimodal question answering on scientific papers. *NeurIPS*, 2024. 7
- [37] Hrituraj Singh and Sumit Shekhar. STL-CQA: Structure-based transformers with localization and encoding for chart question answering. In *Proceedings of the 2020 Conference on Empirical Methods in Natural Language Processing (EMNLP)*, pages 3275–3284, 2020. 2
- [38] Weihang Wang, Qingsong Lv, Wenmeng Yu, Wenyi Hong, Ji Qi, Yan Wang, Junhui Ji, Zhuoyi Yang, Lei Zhao, Xixuan Song, Jiazheng Xu, Bin Xu, Juanzi Li, Yuxiao Dong, Ming Ding, and Jie Tang. Cogvlm: Visual expert for pretrained language models, 2023. 1, 2
- [39] Zirui Wang, Mengzhou Xia, Luxi He, Howard Chen, Yitao Liu, Richard Zhu, Kaiqu Liang, Xindi Wu, Haotian Liu, Sadhika Malladi, Alexis Chevalier, Sanjeev Arora, and Danqi Chen. Charxiv: Charting gaps in realistic chart understanding in multimodal llms. *arXiv preprint arXiv:2406.18521*, 2024. 1, 2, 6
- [40] Renqiu Xia, Bo Zhang, Hancheng Ye, Xiangchao Yan, Qi Liu, Hongbin Zhou, Zijun Chen, Min Dou, Botian Shi, Junchi Yan, et al. Chartx & chartvlm: A versatile benchmark and foundation model for complicated chart reasoning. *arXiv preprint arXiv:2402.12185*, 2024. 2
- [41] Yuan Yao, Tianyu Yu, Ao Zhang, Chongyi Wang, Junbo Cui, Hongji Zhu, Tianchi Cai, Haoyu Li, Weilin Zhao, Zhihui He, et al. Minicpm-v: A gpt-4v level mllm on your phone. *arXiv preprint arXiv:2408.01800*, 2024. 2, 6
- [42] Jiabo Ye, Haiyang Xu, Haowei Liu, Anwen Hu, Ming Yan, Qi Qian, Ji Zhang, Fei Huang, and Jingren Zhou. mplug-owl3: Towards long image-sequence understanding in multimodal large language models, 2024. 2
- [43] Qinghao Ye, Haiyang Xu, Guohai Xu, Jiabo Ye, Ming Yan, Yiyang Zhou, Junyang Wang, Anwen Hu, Pengcheng Shi, Yaya Shi, Chaoya Jiang, Chenliang Li, Yuanhong Xu, Hehong Chen, Junfeng Tian, Qi Qian, Ji Zhang, and Fei Huang. mplug-owl: Modularization empowers large language models with multimodality, 2023.

- [44] Qinghao Ye, Haiyang Xu, Jiabo Ye, Ming Yan, Anwen Hu, Haowei Liu, Qi Qian, Ji Zhang, Fei Huang, and Jingren Zhou. `mplug-owl2`: Revolutionizing multi-modal large language model with modality collaboration, 2023. [2](#), [6](#)
- [45] Liang Zhang, Anwen Hu, Haiyang Xu, Ming Yan, Yichen Xu, Qin Jin, Ji Zhang, and Fei Huang. `Tinychart`: Efficient chart understanding with visual token merging and program-of-thoughts learning, 2024. [2](#), [6](#)
- [46] Jinbo Zhao. `Awesome-mllm-datasets`, 2023. [2](#)

Appendix Table of Contents

A Details of Chart Complexity Vector (CCV)	13
A.1. The Definition of CCV	13
A.2. Proportion of Complexity Aspects in AstroChart	14
A.3. Examples of CCV in AstroChart	14
B Visualization of Samples in AstroChart	17
C Prompts for question-answer pair generation in AstroChart	18
D Examples of AstroChart	25
E Expert Proofreading Website Screenshot	55
F. Details of MLLMs in Evaluation	56
G Details of Evaluation Metrics	57
G.1. Evaluation of Numerical Responses	57
G.2. Evaluation of Open-ended Responses	57
H Other Evaluation Metrics and Results	59
I. Failure cases of AstroChart	60
I.1 . Failure cases of Visual question-answer pair	60
I.2 . Failure cases of Data question-answer pair	60
I.3 . Failure cases of Inference question-answer pair	60
I.4 . Failure cases of Summary question-answer pair	60
I.5 . Failure cases of KB-Inference question-answer pair	60
I.6 . Failure cases of KB-Summary question-answer pair	60

A. Details of Chart Complexity Vector (CCV)

A.1. The Definition of CCV

Tab. 3 defines the Chart Complexity Vector (CCV), which quantifies chart complexity across ten attributes categorized into visual complexity (annotation, color, legend, pattern), data interpretation complexity (axis, element, formula, scale), and structural complexity (subplot, type). Each attribute is assigned a binary score of 0 (simple) or 1 (complex) based on specific criteria.

#	Attributes	Complexity Definition (0 or 1)
Visual Complexity		
1	Annotation Complexity	0: No annotations are used. 1: Extensive annotations such as descriptive text, arrows, or markers.
2	Color Complexity	0: Monochrome or up to two distinct colors. 1: More than two distinct colors or employs a color bar.
3	Legend Complexity	0: Contains no legend or a minimal legend (no more than three categories). 1: Contains a complex legend (more than three categories or intricate representations).
4	Pattern Complexity	0: No more than two distinct graphical patterns. 1: More than two distinct graphical patterns.
Data Interpretation Complexity		
5	Axis Complexity	0: Single axis. 1: Multiple dependent axes (e.g., secondary y-axis, dual x-axis).
6	Element Complexity	0: Contains a single graphical element. 1: Contains more than two graphical elements.
7	Scale Complexity	0: Employs a linear scale. 1: Utilizes logarithmic, power-law, or mixed scales.
8	Formula Complexity	0: Does not contain any mathematical formulas. 1: Includes mathematical formulas.
Structural Complexity		
9	Subplot Complexity	0: A single-panel chart. 1: Multiple interrelated subplots are present.
10	Type Complexity	0: Uses basic chart types (e.g., bar, line, scatter, histogram, pie) with a sparse dataset. 1: Uses complex chart types (e.g., heatmaps, network graphs, mixed-element charts, multiple chart combinations) and/or handles high-density data (e.g., dense bar, line, scatter, or histogram charts).

Table 3. Definitions of CCV Attributes

A.2. Proportion of Complexity Aspects in AstroChart

Tab. 4 summarizes the distribution of simple and complex charts across different Chart Complexity Vector (CCV) attributes in the AstroChart benchmark. The results indicate that Color Complexity (78%) and Type Complexity (68%) are the most frequently observed complex attributes, suggesting a prevalence of multi-colored and structurally diverse charts. In contrast, Axis Complexity (92%) and Element Complexity (65%) are predominantly simple, implying that most charts use a single axis and contain limited graphical elements. These statistics provide insight into the complexity characteristics of charts in AstroChart.

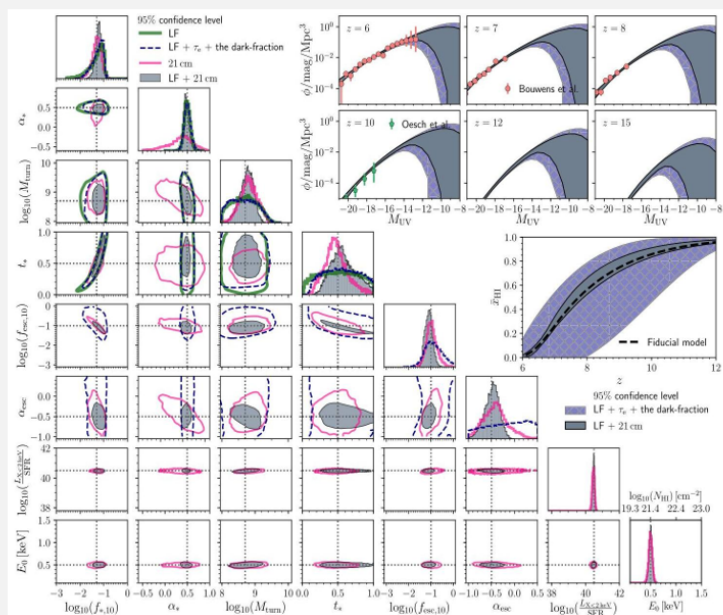
#	Attributes	Simple	Complex
Visual Complexity			
1	Annotation Complexity	59%	41%
2	Color Complexity	22%	78%
3	Legend Complexity	53%	47%
4	Pattern Complexity	49%	51%
Data Interpretation Complexity			
5	Axis Complexity	92%	8%
6	Element Complexity	65%	35%
7	Scale Complexity	58%	42%
8	Formula Complexity	63%	37%
Structural Complexity			
9	Subplot Complexity	58%	42%
10	Type Complexity	32%	68%

Table 4. The proportion of simple/complex charts across different complexity aspects in AstroChart

A.3. Examples of CCV in AstroChart

Fig. 7 and Fig. 8 illustrate the process of computing CCV for each astronomical chart.

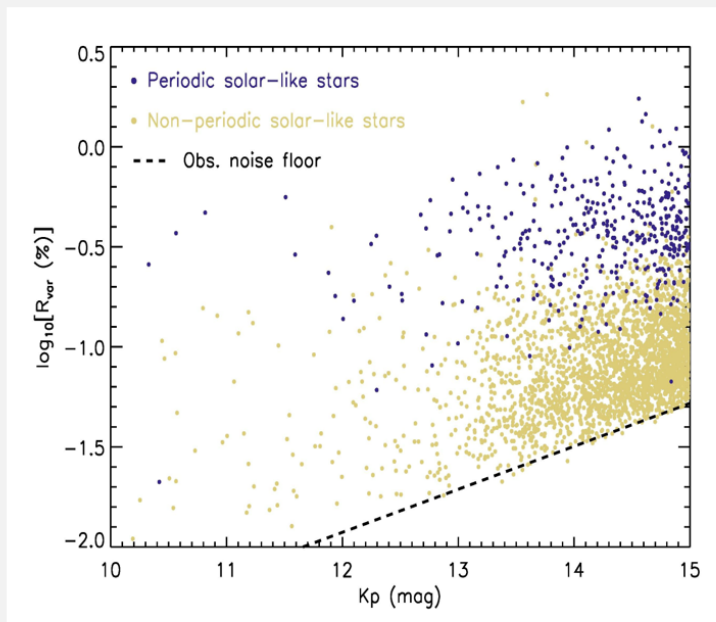
CCV Example



CCV for the chart	
Annotation Complexity	1
Color Complexity	1
Legend Complexity	1
Pattern Complexity	1
Axis Complexity	0
Element Complexity	1
Scale Complexity	1
Formula Complexity	1
Subplot Complexity	1
Type Complexity	1
All	9

Figure 7. Example for CCV in AstroChart

CCV Example



CCV for the chart

Annotation Complexity	0
Color Complexity	1
Legend Complexity	1
Pattern Complexity	1
Axis Complexity	0
Element Complexity	1
Scale Complexity	0
Formula Complexity	0
Subplot Complexity	0
Type Complexity	0

All 4

Figure 8. Example for CCV in AstroChart

B. Visualization of Samples in AstroChart

Fig. 9 visualizes sample charts from the AstroChart benchmark, illustrating its diversity and complexity.

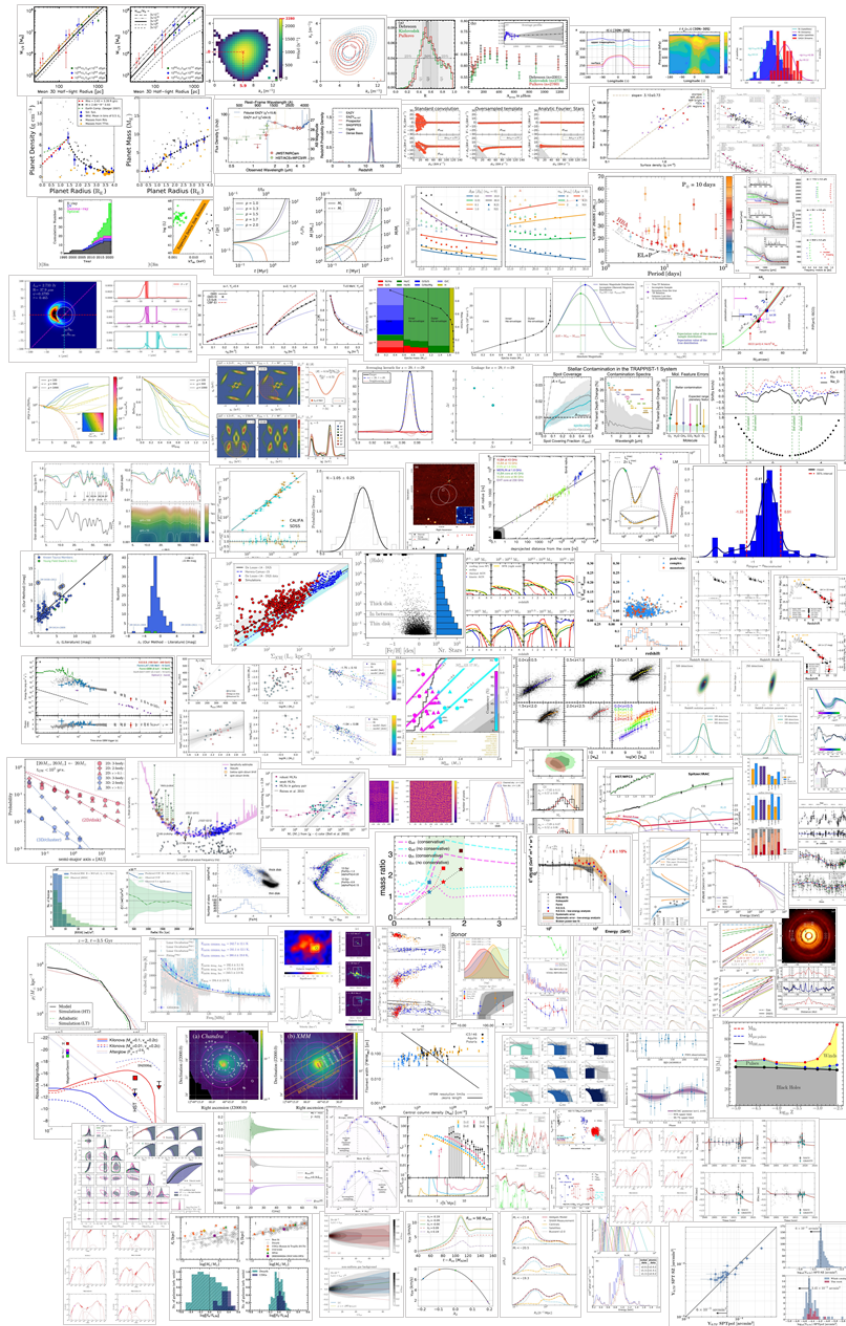


Figure 9. Visualization of Sample Charts in AstroChart

C. Prompts for question-answer pair generation in AstroChart

We employed Claude 3.5 to generate question-answer pairs, designing distinct prompts for each category of questions. Specifically, for the two primary types: FQA pair and AQA pair. We implemented different input configurations. For the FQA pair, the input consisted of the chart along with its corresponding caption. For the AQA pair, the input additionally included descriptive content from the associated paper. This differentiation was essential, as knowledge-based questions often require contextual background derived from the broader content of the paper.

To generate different question-answer pair types, we formulated targeted prompts:

- **FQA pairs:**
 - *Visual questions-answer pair* (Fig. 10) The questions should focus on the graphical elements of the chart, including colors, labels, text, formulas, and chart types.
 - *Data questions-answer pair* (Fig. 11) The questions should require retrieving specific data points or a range of values from the chart.
 - *Inference questions-answer pair* (Fig. 12) The questions should involve numerical calculations, comparisons, or analytical reasoning beyond direct data extraction from the chart.
 - *Summary questions-answer pair* (Fig. 13) The task is to generate a comprehensive summary describing all visual elements of the chart, including colors, labels, texts, formulas, chart types, and structural components.
- **AQA pairs:**
 - *KB-Inference questions-answer pair* (Fig. 14) The question requires astronomical domain knowledge and analytical reasoning, with a focus on explaining chart relationships using scientific insights, without directly referencing the article’s conclusion.
 - *KB-Summary questions-answer pair* (Fig. 15) The questions should extract and articulate the most important conclusion or inference derived from the chart.

Example For Prompt

Visual Question-Answer Pair

Role:

You are an AI visual assistant who can analyze a scientific paper graph.

Task:

You are provided with an image. Generate three visual questions based solely on the provided image and information.

For each question, provide the following:

Question: The question itself.

Answer: The final, concise answer.

Requirements:

The questions should focus on the graphical elements of the chart, including colors, text, formulas, and chart types. Avoid questions related to identifying maximum or minimum values. Instead, emphasize the interpretation and analysis of visual components, ensuring the questions assess the model's ability to understand and describe chart elements accurately. Avoid questions related to the data range problem. Answers should be within 10 words.

Figure 10. Prompt for visual question-answer pair generation.

Example For Prompt

Data Question-Answer Pair

Role:

You are an AI visual assistant who can analyze a scientific paper graph.

Task:

You are provided with an image. Generate three data questions based solely on the provided image and information.

For each question, provide the following:

Question: The question itself.

Answer: The final, concise answer.

Requirements:

The question should require retrieving specific data points or a range of data points from the chart. Avoid questions that simply read numbers directly from the image or involve identifying maximum or minimum values. Emphasize numerical data retrieval and interpretation to assess the model's ability to extract meaningful information from the chart. Answers should be within 10 words.

Figure 11. Prompt for data question-answer pair generation.

Example For Prompt

Inference Question-Answer Pair

Role:

You are an AI visual assistant who can analyze a scientific paper graph.

Task:

You are provided with an image, caption, and description. Generate two inference questions based solely on the provided image and information.

For each question, provide the following:

Question: The question itself.

Answer: The final, concise answer.

Requirements:

The question requires numerical calculations, comparisons, or analytical reasoning beyond direct data extraction from the image. Ensure the questions involve identifying patterns, relationships, or trends within the chart. Only include questions that have clear, verifiable answers. Answer should be within 20 words.

Figure 12. Prompt for inference question-answer pair generation.

Example For Prompt

Summary Question-Answer Pair

Role:

You are an AI visual assistant who can analyze a scientific paper graph.

Task:

You are provided with an image and its caption. Generate a chart summary based solely on the provided image and information.

For each question, provide the following:

Question: The question itself.

Answer: The final, concise answer.

Requirements:

Generate a chart summary that describes all visual elements of the chart, including colors, labels, text, formulas, chart types, and structural components. The summary should provide a clear and structured overview. Answers should be within 100 words.

Figure 13. Prompt for summary question-answer pair generation.

Example For Prompt

KB-Inference Question-Answer Pair

Role:

You are an AI visual assistant who can analyze a scientific paper graph.

Task:

You are provided with an image which can reveal the conclusion of the article, and the conclusion of the article that related for the figure.

Generate one kb-inference question and the answer based solely on the provided image and information.

For each question, provide the following:

Question: The question itself.

Answer: The final, concise answer.

Requirements:

The question requires astronomical domain knowledge and analytical reasoning. The questions should be answerable based on the given conclusion of the related article while avoiding direct references to 'the paper's conclusion' or similar phrases. Focus on explaining relationships in the chart using relevant scientific insights. The answer should be within 50 words.

Figure 14. Prompt for KB-inference question-answer pair generation.

Example For Prompt

KB-Summary Question-Answer Pair

Role:

You are an AI visual assistant who can analyze a scientific paper graph.

Task:

You are provided with an image which can reveal the conclusion of the article, the conclusion of the article that related for the figure and the caption of this figure.

Generate a kb-summary question-answer pair according to the conclusion and the given figure that aims to summarize the trend-like or high-level characteristics of the chart.

For each question, provide the following:

Question: The question itself.

Answer: The final, concise answer.

Requirements:

Generate a concise summary that integrates chart data with relevant astronomical domain knowledge. The summary should clearly explain key insights from the chart while incorporating scientific context, demonstrating the model's ability to synthesize visual information and domain expertise. The answer should be within 100 words.

Figure 15. Prompt for KB-summary question-answer pair generation.

D. Examples of AstroChart

We generated a total of 1890 question-answer pairs, consisting of 1,509 FQA pairs and 381 AQA pairs. The FQA pairs are further divided into four subcategories:

- **Visual question-answer pairs:** 603 in total, covering four Types—Text (Fig. 16), Color (Fig. 17), Style (Fig. 18), and Layout (Fig. 19, Fig. 20).
- **Data question-answer pairs:** 315 in total, categorized into Calculation (Fig. 21, Fig. 22), Point (Fig. 23), and Interval (Fig. 24, Fig. 25).
- **Inference questions-answer pair:** 289 pairs (Fig. 26, Fig. 27, Fig. 28, Fig. 29, Fig. 30).
- **Summary questions-answer pair:** 302 pairs (Fig. 31, Fig. 32, Fig. 33, Fig. 34, Fig. 35).

The AQA pairs are divided into two types:

- **KB-Inference questions-answer pair:** 200 pairs (Fig. 36, Fig. 37, Fig. 38, Fig. 39, Fig. 40).
- **KB-Summary questions-answer pair:** 181 pairs (Fig. 41, Fig. 42, Fig. 43, Fig. 44, Fig. 45).

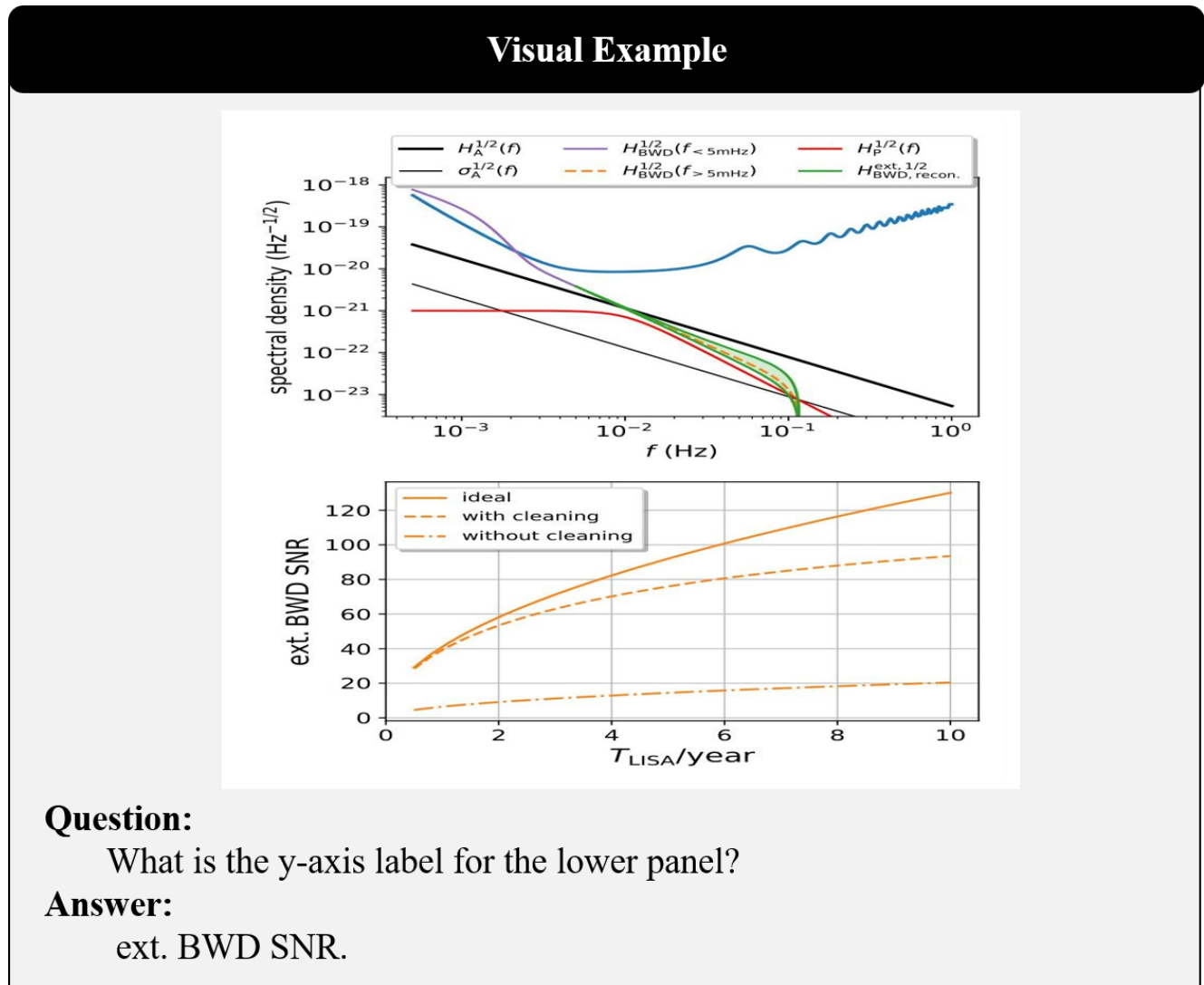
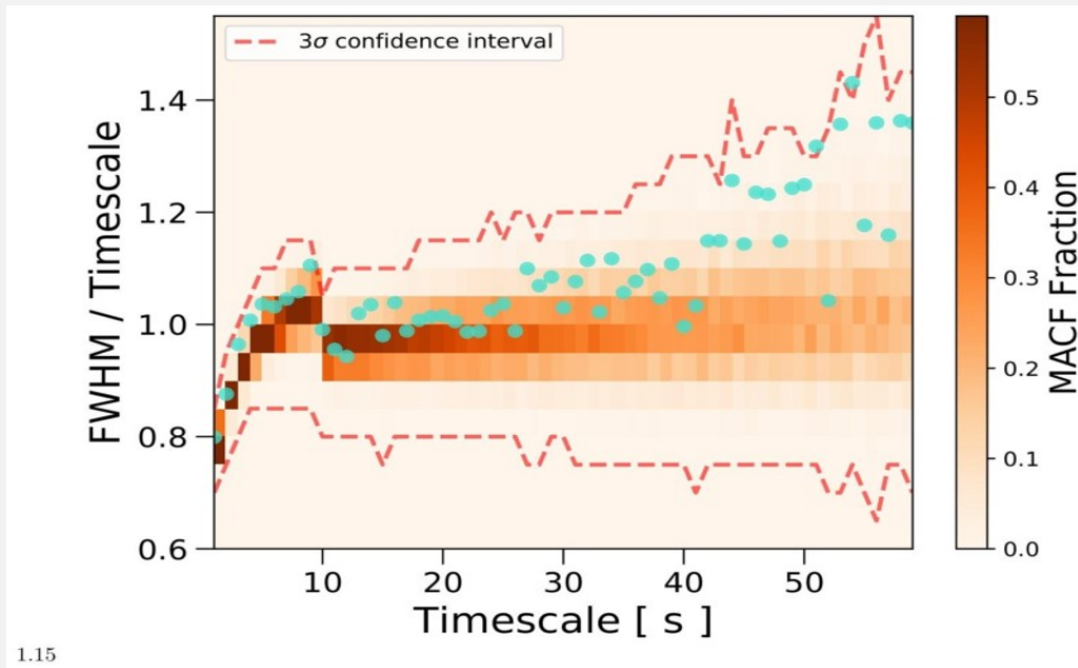


Figure 16. Example for visual question-answer pair.

Visual Example



Question:

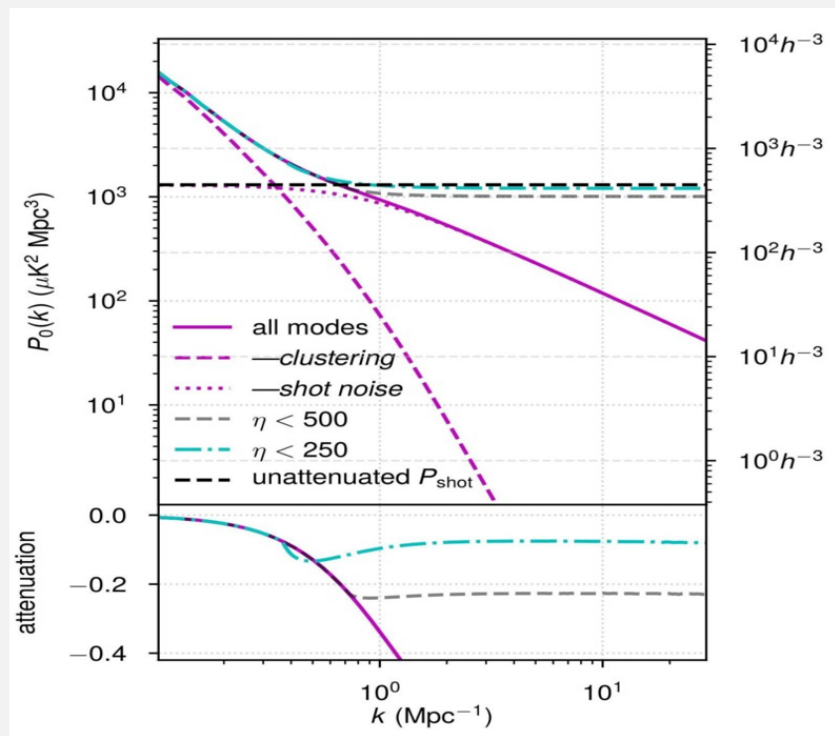
What color are the data points representing VERITAS observations in the graph?

Answer:

The VERITAS observation data points are turquoise or light blue.

Figure 17. Example for visual question-answer pair.

Visual Example



Question:

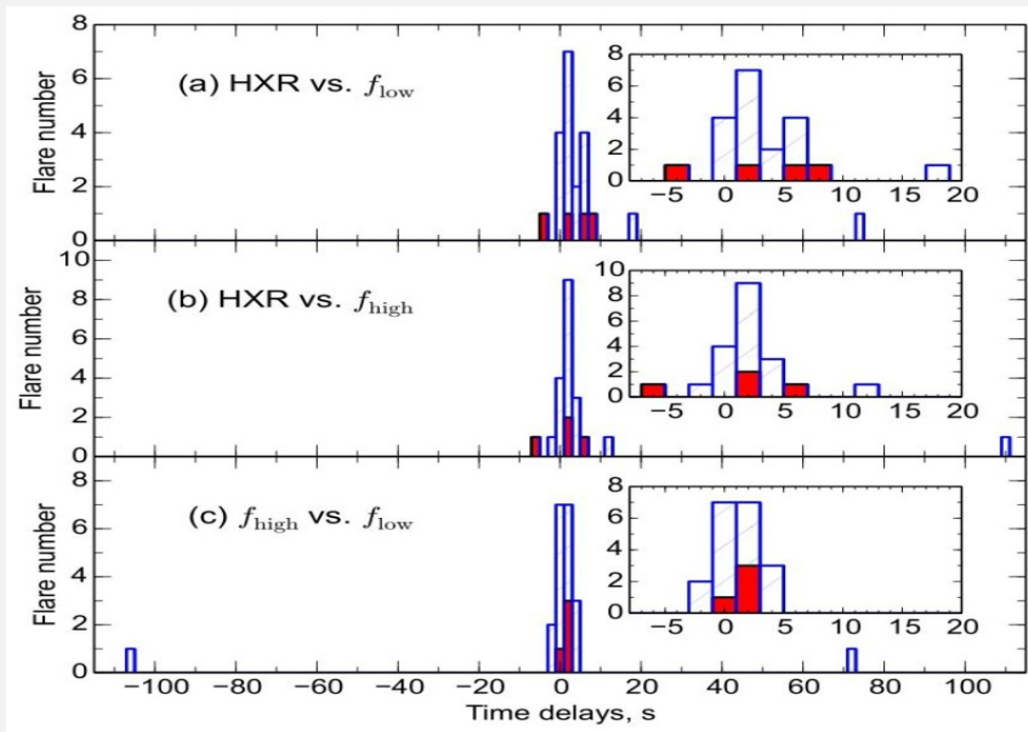
How many different line styles are used in the upper panel of the graph?

Answer:

Four: solid, dashed, dotted, and dash-dotted.

Figure 18. Example for visual question-answer pair.

Visual Example



Question:

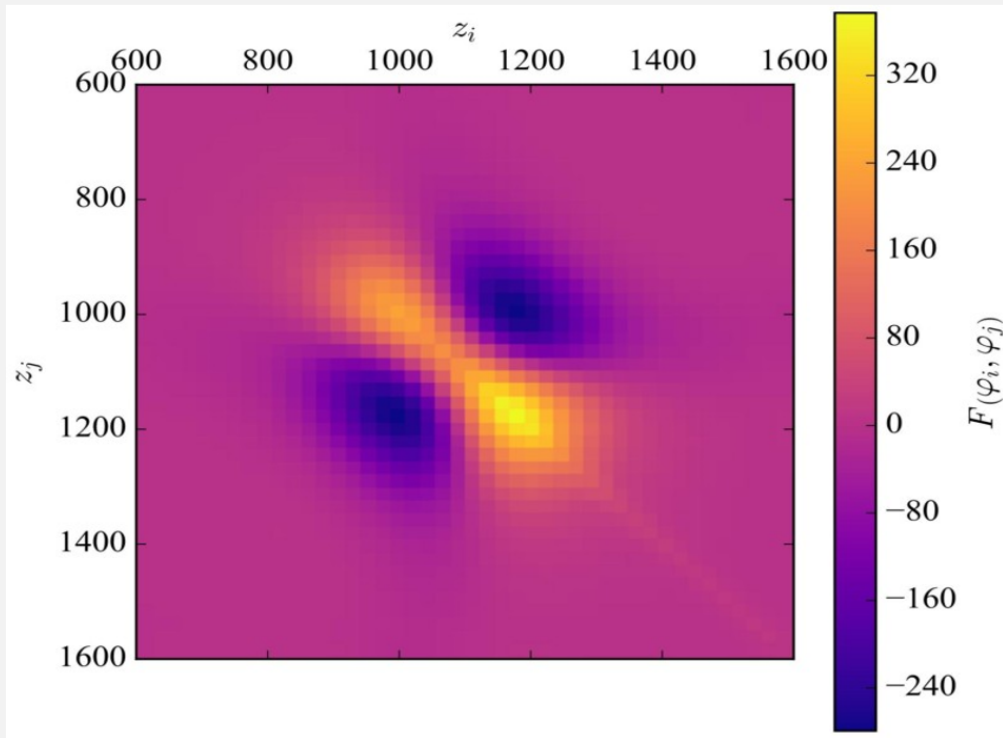
How many subplots are present in the main figure?

Answer:

There are three main subplots labeled (a), (b), and (c).

Figure 19. Example for visual question-answer pair.

Visual Example



Question:

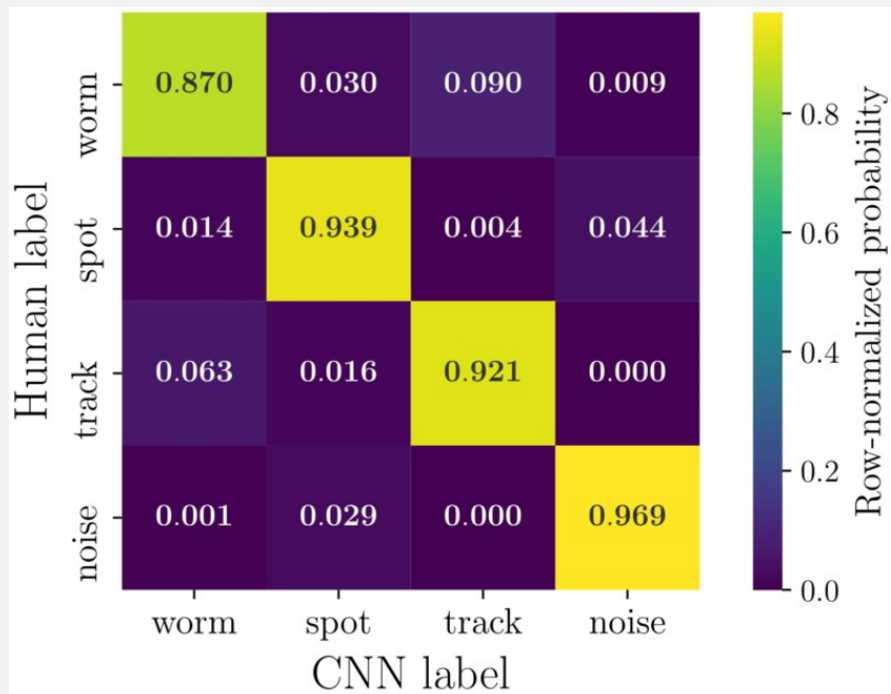
What type of chart is used to represent the data in this image?

Answer:

A marginalised matrix plot or heatmap.

Figure 20. Example for visual question-answer pair.

Data Example



Question:

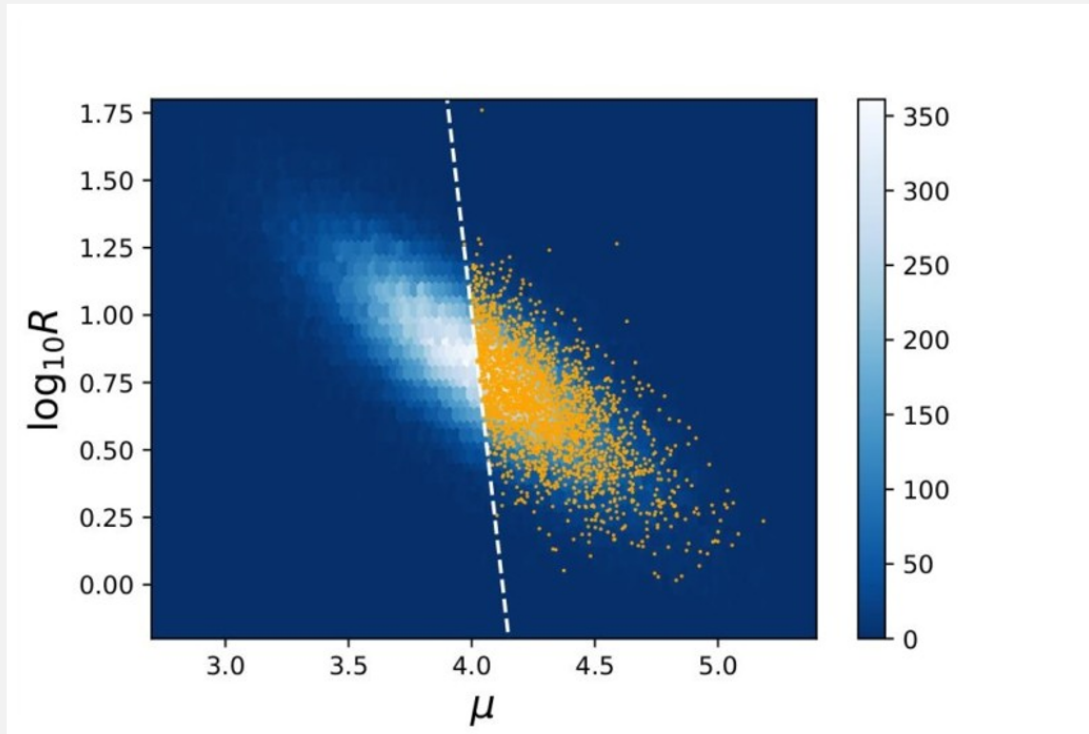
What is the total misclassification rate for the "worm" category?

Answer:

The total misclassification rate for "worm" is 0.13.

Figure 21. Example for data question-answer pair.

Data Example



Question:

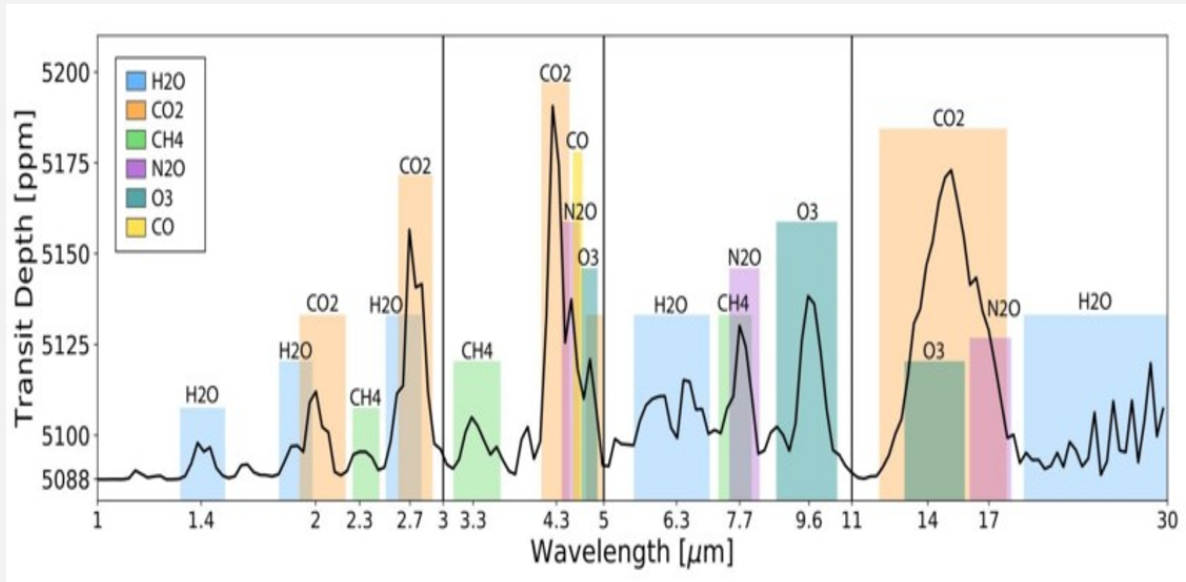
If the selection boundary slope (a_1) was increased by 50%, how would this affect the number of selected galaxies?

Answer:

Increasing the slope would likely reduce the number of selected galaxies, as fewer would fall above the steeper selection line.

Figure 22. Example for data question-answer pair.

Data Example



Question:

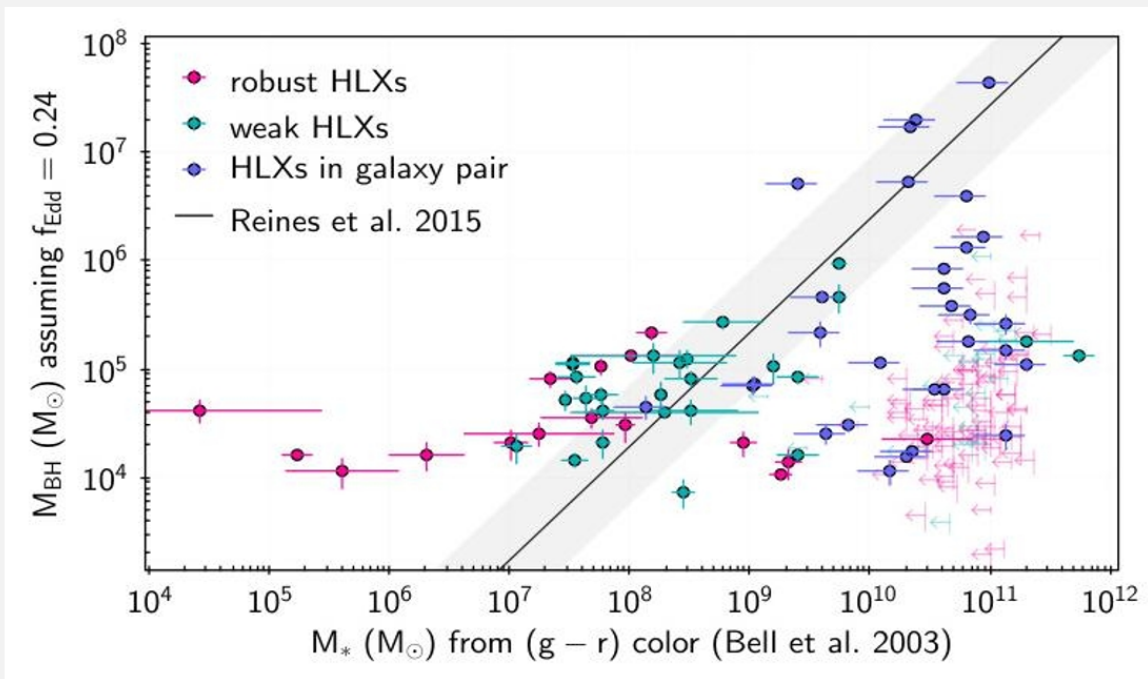
At which transit depth does the first CO₂ band appear in the chart?

Answer:

Approximately 5142 ppm.

Figure 23. Example for data question-answer pair.

Data Example



Question:

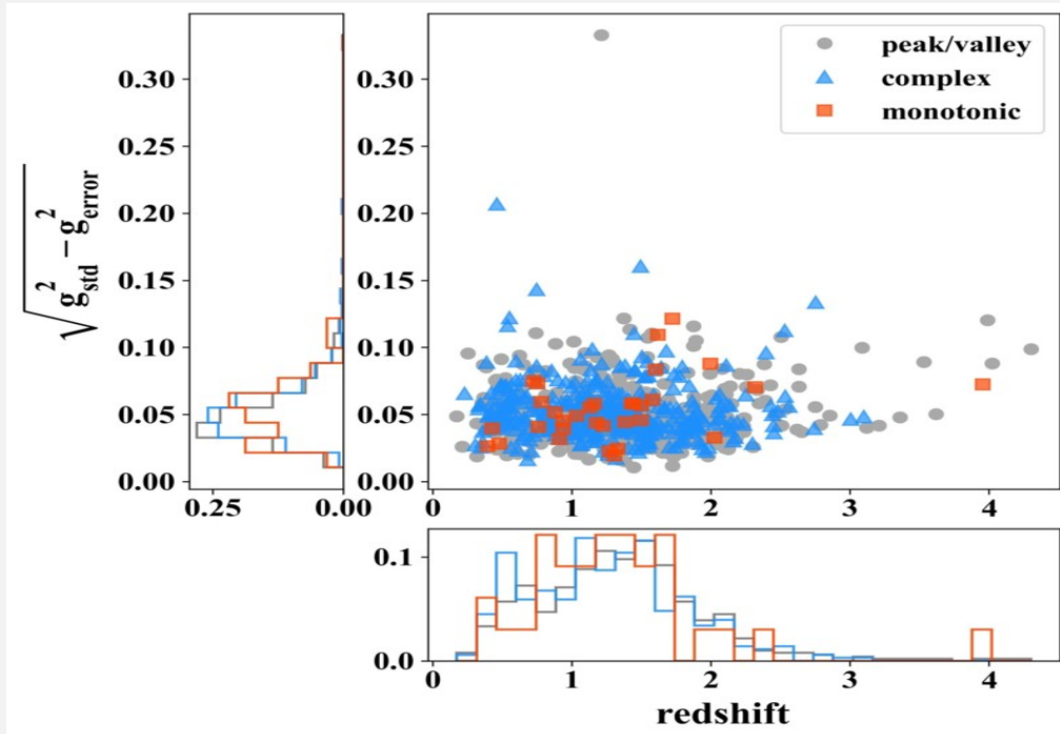
What is the range of the black hole mass among all data points?

Answer:

From 10^3 to 10^8 solar masses.

Figure 24. Example for data question-answer pair.

Data Example



Question:

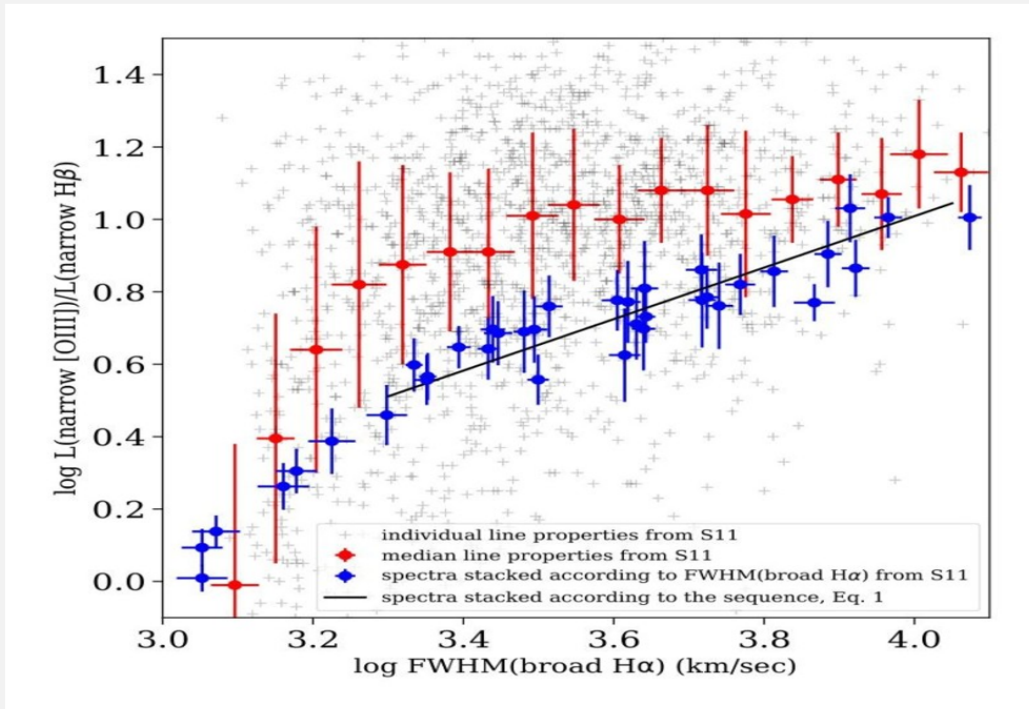
What is the approximate range of redshift values shown in the main scatter plot?

Answer:

From approximately 0.1 to about 4.3.

Figure 25. Example for data question-answer pair.

Inference Example



Question:

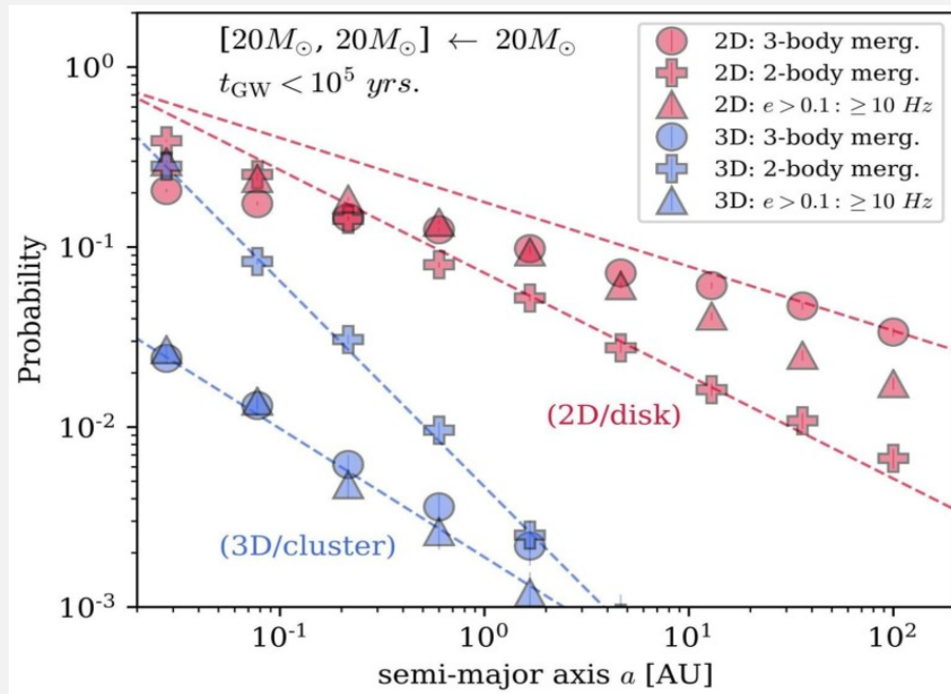
How does the trend of blue data points compare to the black line?

Answer:

The blue points follow the black line closely, with some fluctuations around it.

Figure 26. Example for inference question-answer pair.

Inference Example



Question:

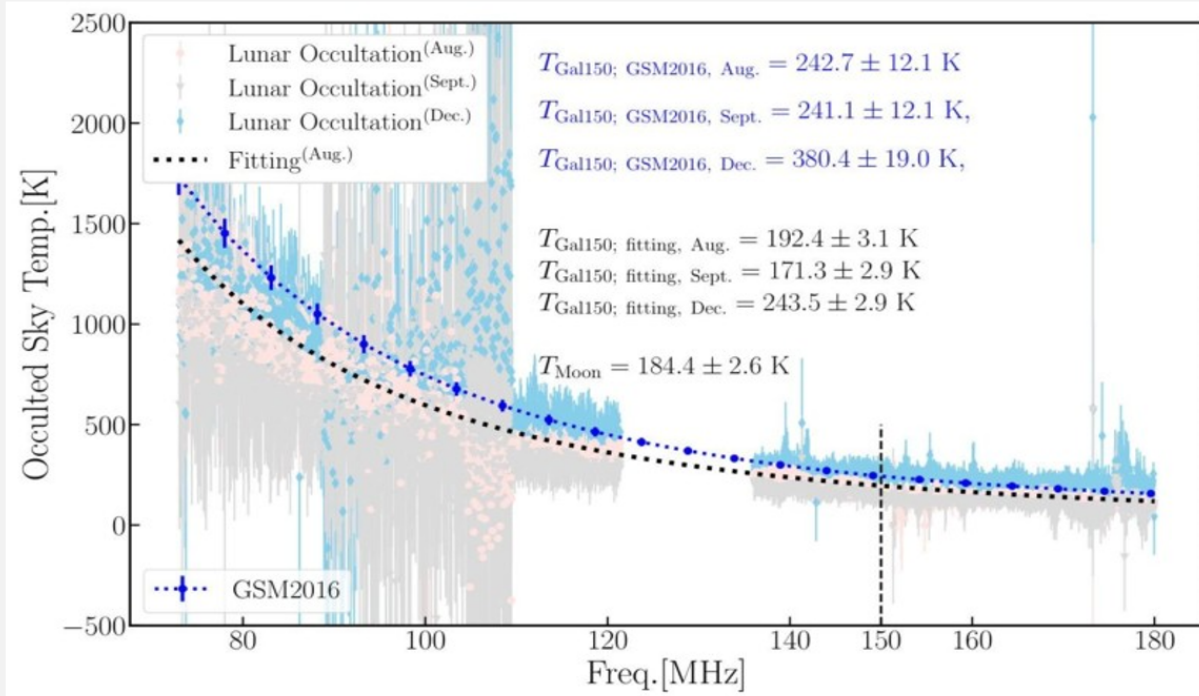
What trend can be observed in merger probabilities as the semi-major axis increases?

Answer:

Merger probabilities generally decrease as the semi-major axis increases for both 2D and 3D interactions.

Figure 27. Example for inference question-answer pair.

Inference Example



Question:

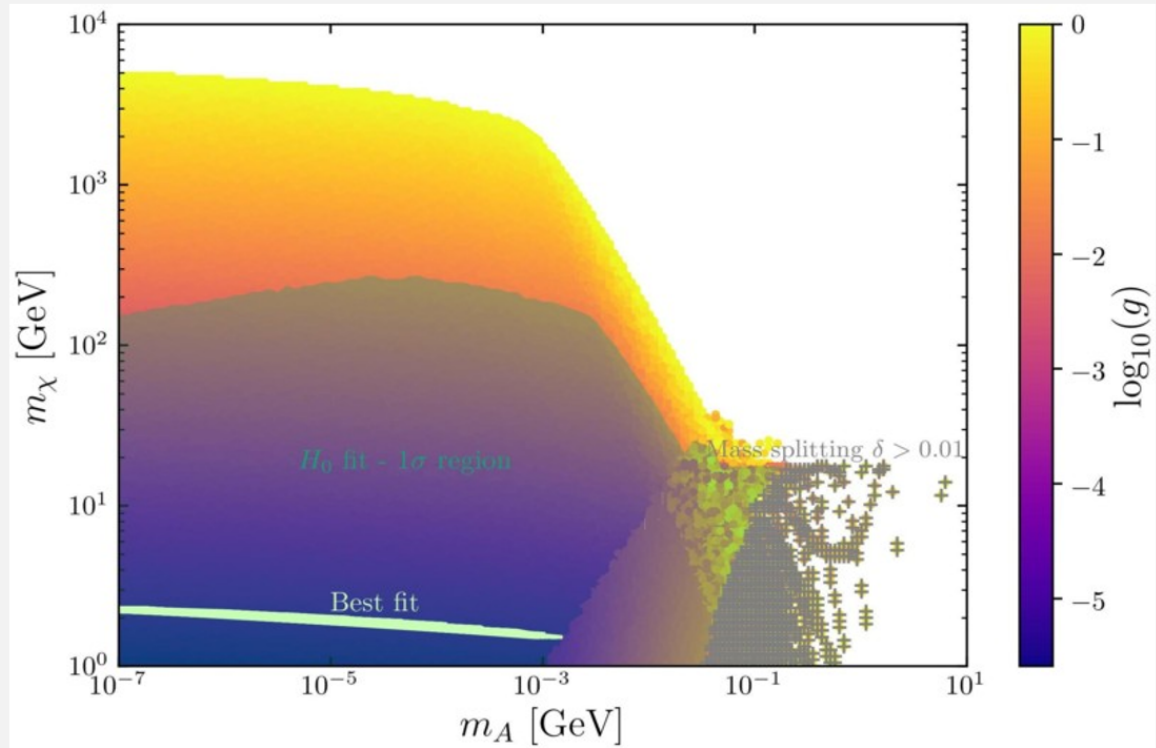
How does the fitted temperature for August compare to the GSM2016 temperature for August?

Answer:

The fitted temperature (192.4 K) is lower than the GSM2016 temperature (242.7 K).

Figure 28. Example for inference question-answer pair.

Inference Example



Question:

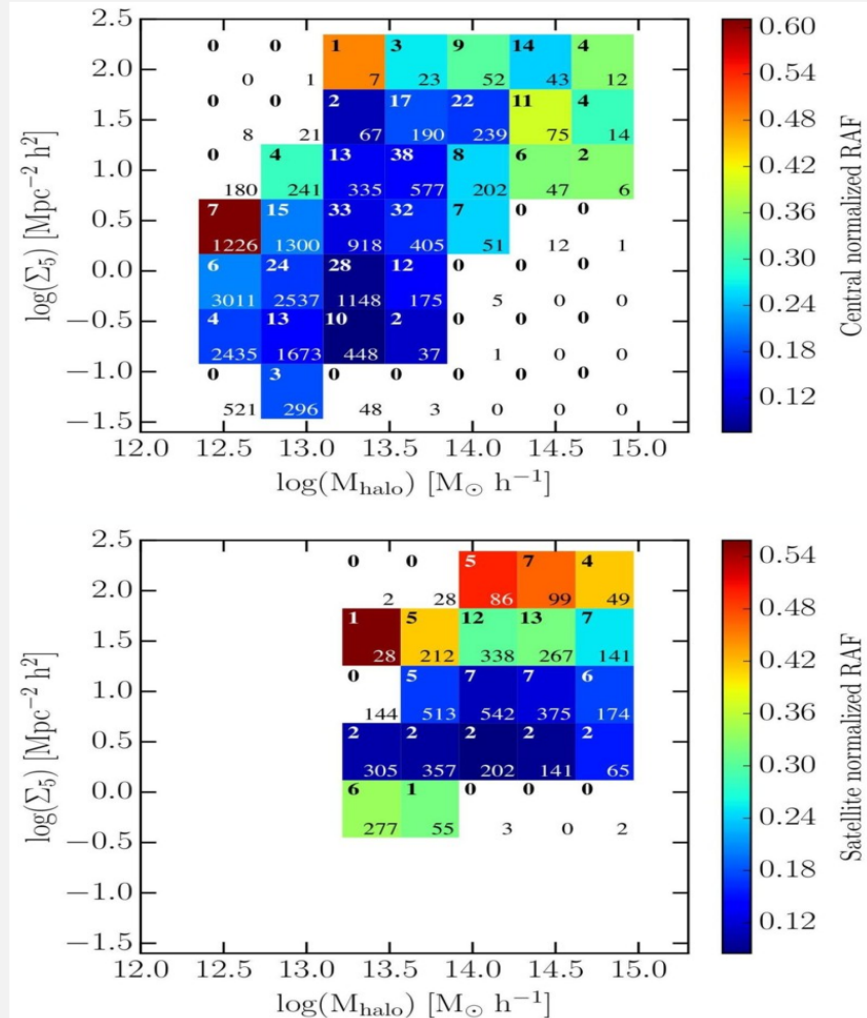
If the mediator mass m_A increases from 10^{-7} GeV to 10^{-3} GeV, how does the maximum allowed dark matter mass m_χ change?

Answer:

The maximum allowed m_χ decreases from about 5000 GeV to approximately 2000 GeV, a reduction of roughly 60%.

Figure 29. Example for inference question-answer pair.

Inference Example



Question:

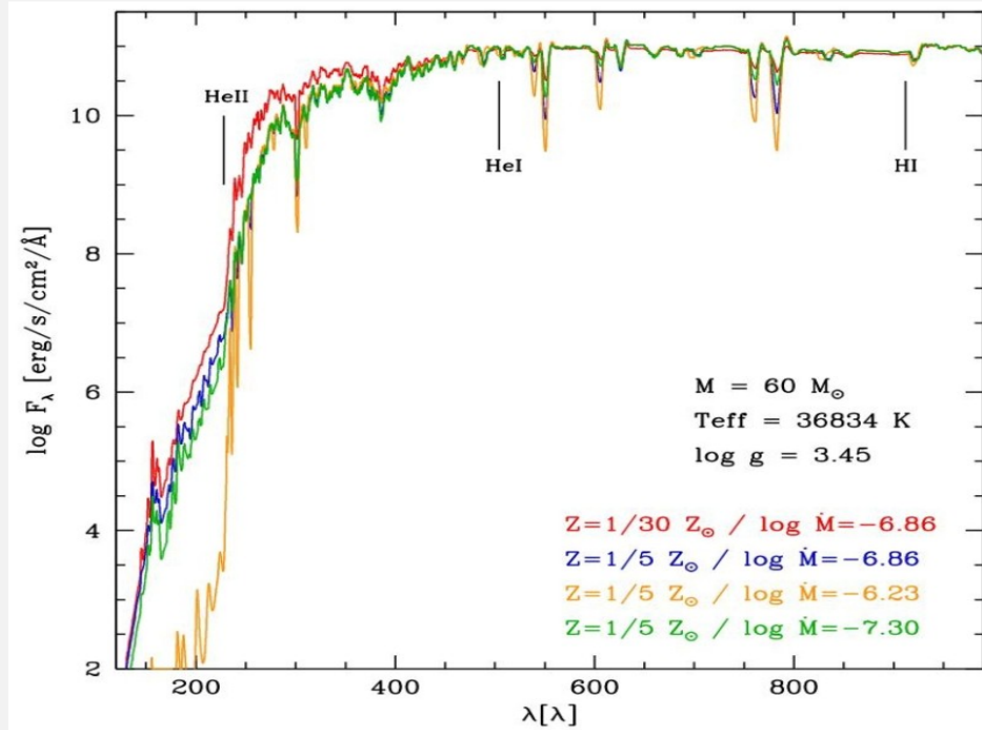
How does the dependence of RAF on local density differ between central and satellite galaxies?

Answer:

Satellite RAF depends on local density, while central RAF shows little dependence.

Figure 30. Example for inference question-answer pair.

Summary Example



Question:

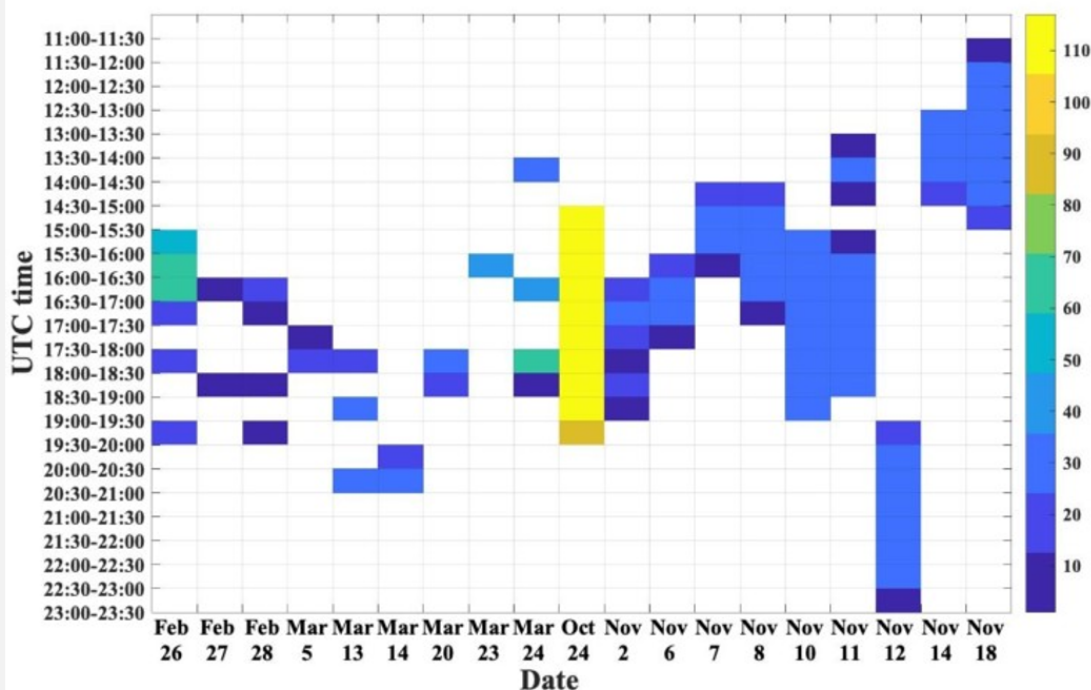
Generate a chart description that aims at presenting all the visual elements of the plot. Answers should be within 100 words.

Answer:

This chart displays spectral energy distributions (SEDs) for a $60 M_{\odot}$ star model at different metallicities and mass-loss rates. It shows $\log F_{\lambda}$ versus wavelength (λ) in Angstroms. Four colored lines represent different scenarios: red ($Z=1/30 Z_{\odot}$), blue ($Z=1/5 Z_{\odot}$), orange ($Z=1/5 Z_{\odot}$ with increased mass-loss), and green ($Z=1/5 Z_{\odot}$ with reduced mass-loss). The graph includes labels for HeII, HeI, and HI ionization edges. Additional model parameters like T_{eff} , $\log g$, and mass are provided. The chart illustrates how metallicity and mass-loss rates affect the star's spectral properties.

Figure 31. Example for summary question-answer pair.

Summary Example



Question:

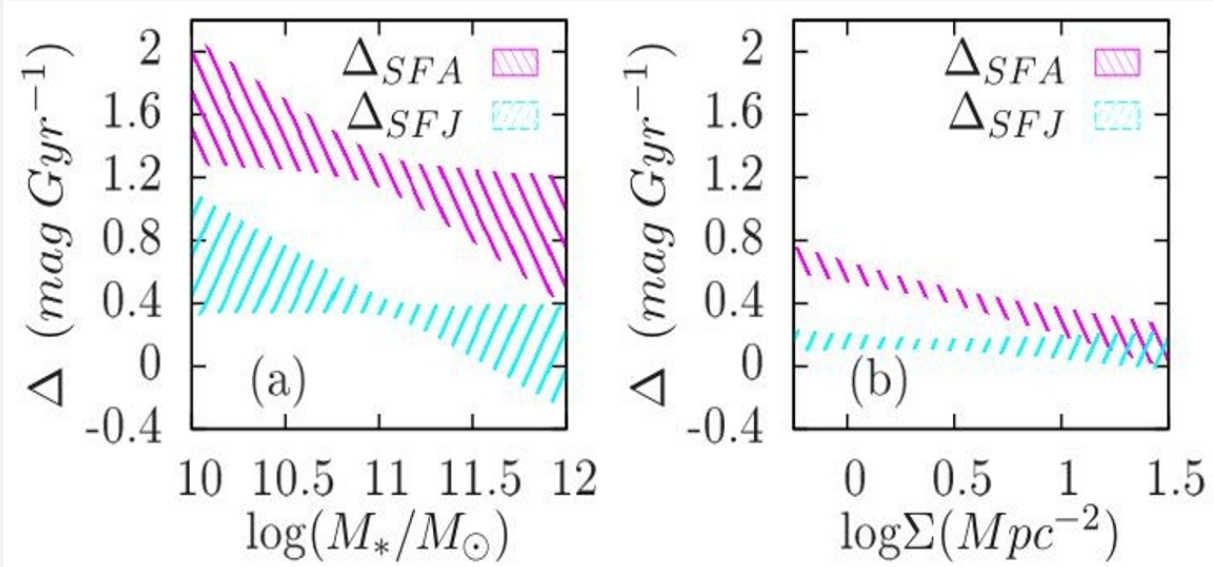
Generate a chart description that aims at presenting all the visual elements of the plot. Answers should be within 100 words.

Answer:

The chart is a heat map showing sodium lidar data availability. The x-axis displays dates from February to November, while the y-axis shows UTC time in half-hour increments from 11:00 to 23:30. Colored grid cells represent data quantity collected in each time slot. Colors range from dark blue (least data) to yellow (most data). The chart reveals patterns in nightly observation periods and data collection intensity across different dates and times.

Figure 32. Example for summary question-answer pair.

Summary Example



Question:

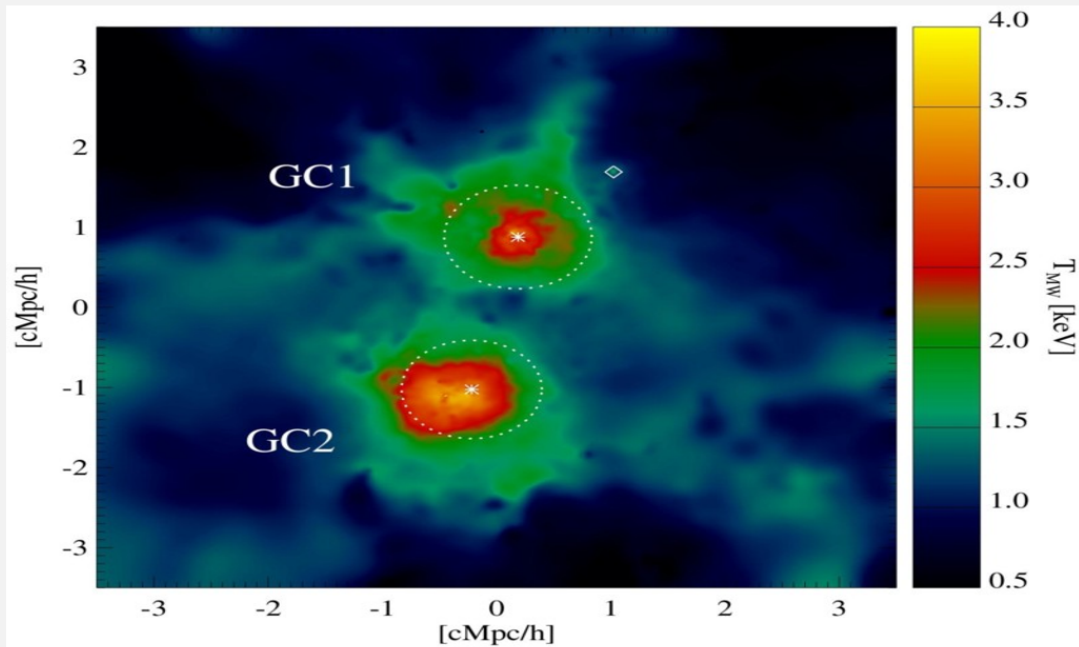
Generate a chart description that aims at presenting all the visual elements of the plot. Answers should be within 100 words.

Answer:

The image contains two side-by-side panels, (a) and (b), showing shaded area plots. Panel (a) displays Δ_{SFA} and Δ_{SFJ} as a function of \log stellar mass, while panel (b) shows them as a function of \log local environment density. Both use pink/magenta for Δ_{SFA} and light blue/cyan for Δ_{SFJ} . The y-axis represents Δ in mag Gyr⁻¹ for both panels. Δ_{SFA} consistently shows higher values than Δ_{SFJ} in both graphs, with both metrics generally decreasing as x-axis values increase.

Figure 33. Example for summary question-answer pair.

Summary Example



Question:

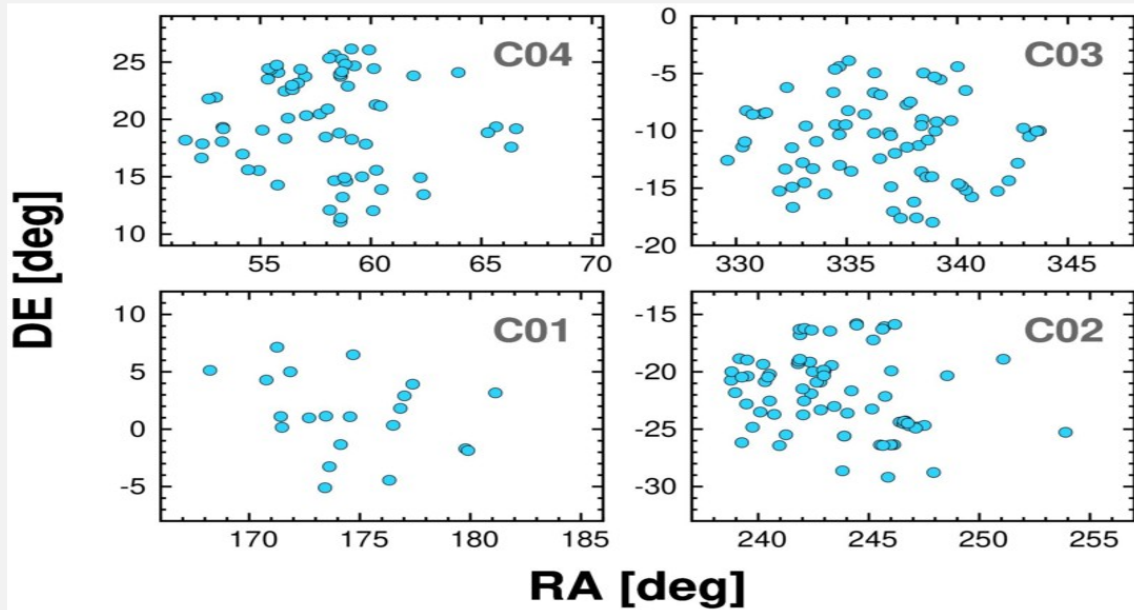
Generate a chart description that aims at presenting all the visual elements of the plot. Answers should be within 100 words.

Answer:

The image shows a projected mass-weighted temperature map of a galaxy cluster pair at $z=0.07$. The map spans 7 cMpc per side, centered on the system's center of mass. Two distinct galaxy clusters, GC1 and GC2, are visible, marked by white dotted circles indicating their r_{500} radii. GC1 is located in the upper half, while GC2 is in the lower half of the image. Both clusters show high-temperature cores (red-orange) surrounded by cooler regions (green-blue). A small diamond symbol in the upper right quadrant marks the position of group B. The temperature scale ranges from 0.5 to 4.0 keV, represented by a color gradient from dark blue to yellow.

Figure 34. Example for summary question-answer pair.

Summary Example



Question:

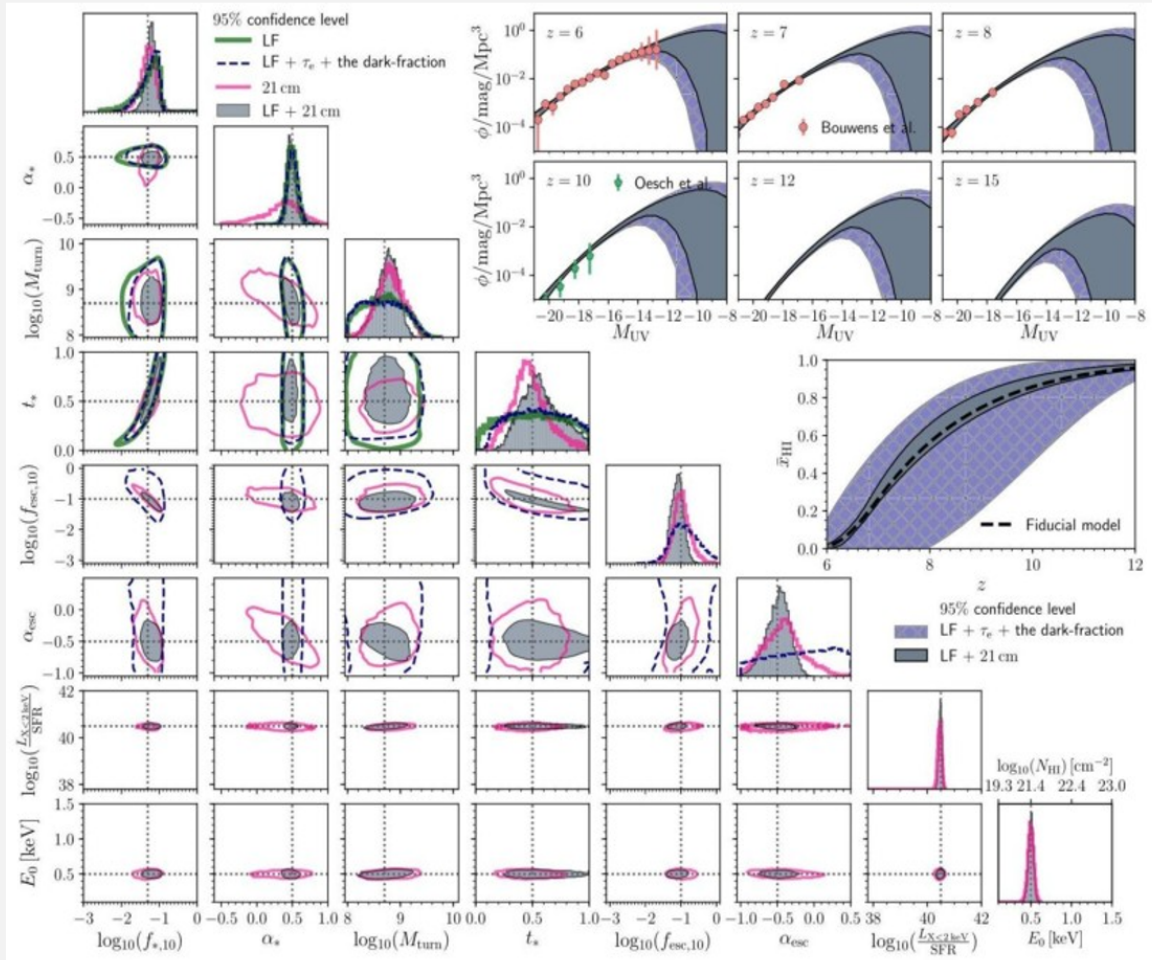
Generate a chart description that aims at presenting all the visual elements of the plot. Answers should be within 100 words.

Answer:

The image consists of four scatter plots arranged in a 2x2 grid, labeled C04, C03, C01, and C02. Each subplot shows light blue data points plotted on axes labeled RA [deg] (x-axis) and DE [deg] (y-axis). The plots display different ranges for both RA and DE values, with C04 and C03 on the top row, and C01 and C02 on the bottom row. The data points in each subplot show varying distributions and densities.

Figure 35. Example for summary question-answer pair.

KB-Inference Example



Question:

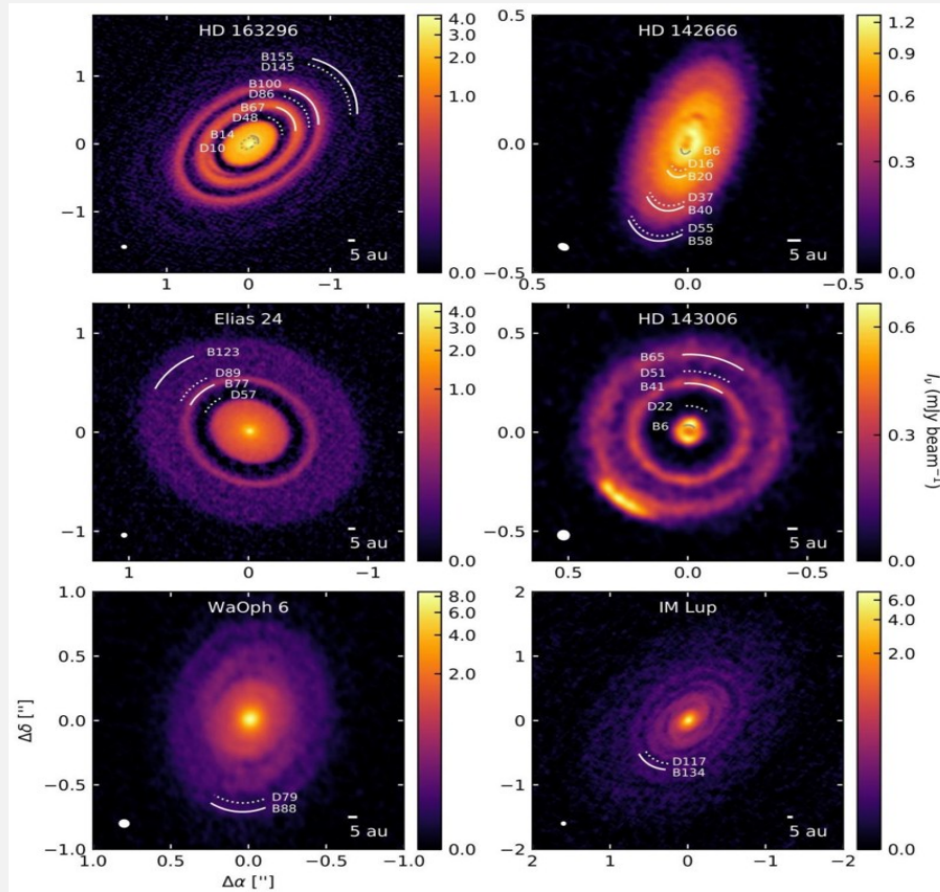
How does the combination of UV luminosity functions and 21-cm data affect the constraints on astrophysical parameters across different redshifts, as shown in the figure?

Answer:

The figure demonstrates that combining UV luminosity functions (LF) with 21-cm data (gray shaded areas) significantly narrows the confidence intervals for astrophysical parameters compared to using LF alone (green contours). This improved constraint is consistent across various redshifts ($z=6$ to $z=15$) shown in the upper right panels.

Figure 36. Example for KB-inference question-answer pair.

KB-Inference Example



Question:

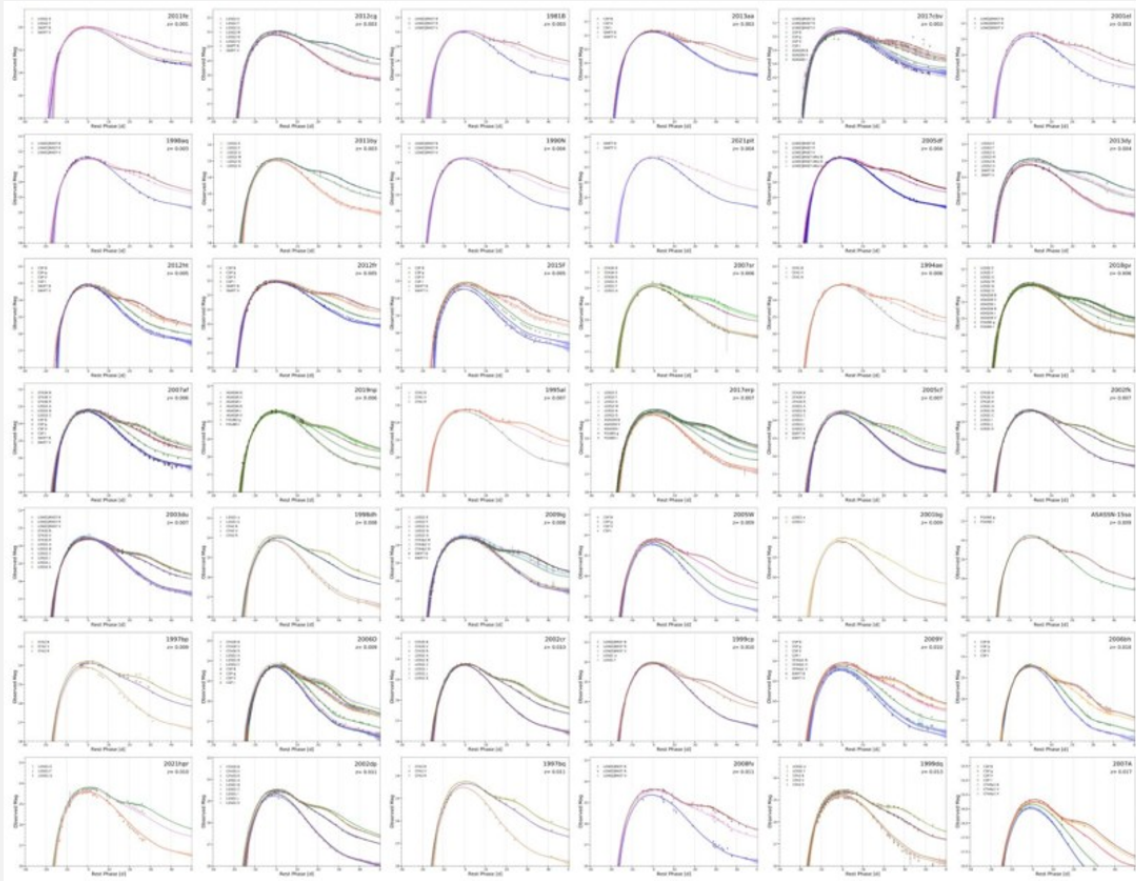
How do the annular substructures in protoplanetary disks vary across different stellar systems, as shown in the image?

Answer:

The image reveals diverse ring and gap patterns in protoplanetary disks around different stars. The structures vary in number, width, intensity, and radial distance from the central star. Some disks, like HD 163296, show multiple distinct rings, while others, like WaOph 6, have fewer visible substructures.

Figure 37. Example for KB-inference question-answer pair.

KB-Inference Example



Question:

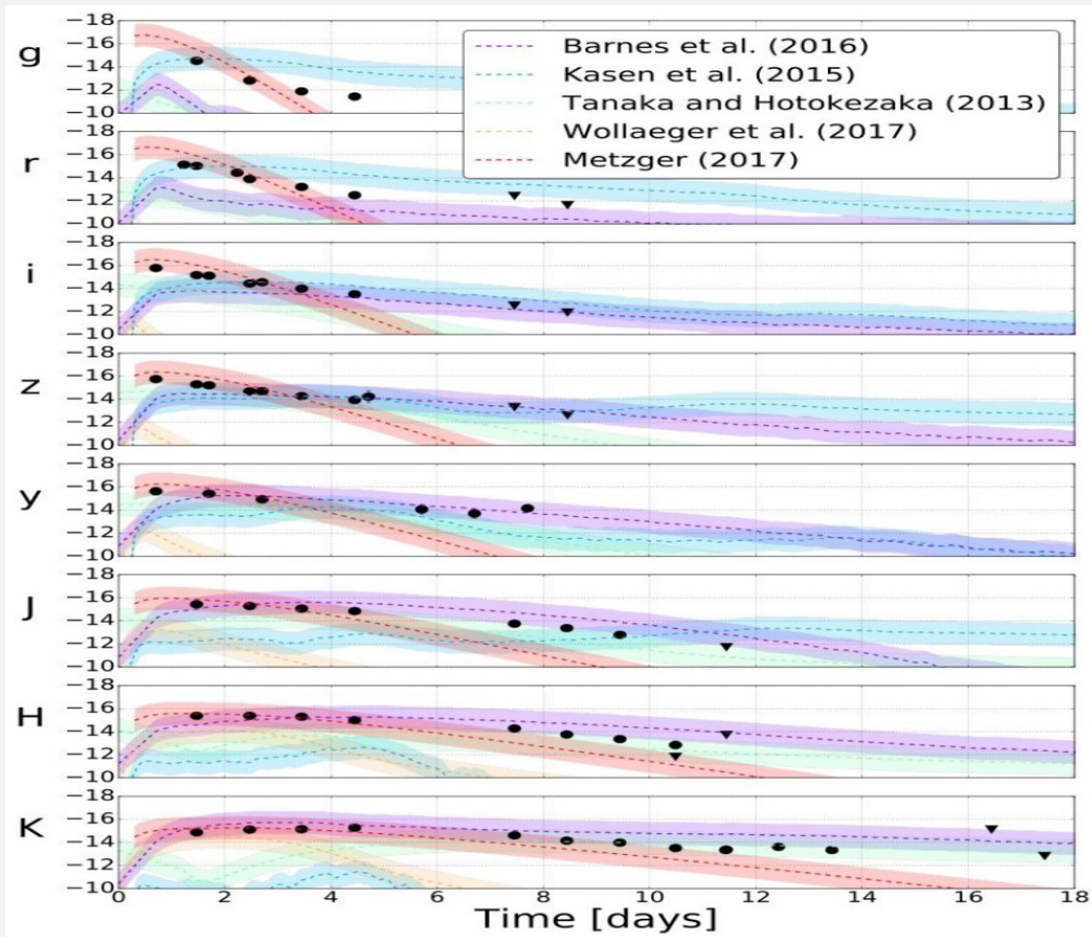
How does the diversity in light curve shapes across different Type Ia supernovae observations contribute to improving the measurement of cosmological parameters?

Answer:

The varied light curve shapes shown in the image reflect the diversity of Type Ia supernovae observations. This diversity, when analyzed across a large dataset, helps refine measurements of cosmological parameters by providing a more comprehensive understanding of supernova behavior and reducing systematic uncertainties.

Figure 38. Example for KB-inference question-answer pair.

KB-Inference Example



Question:

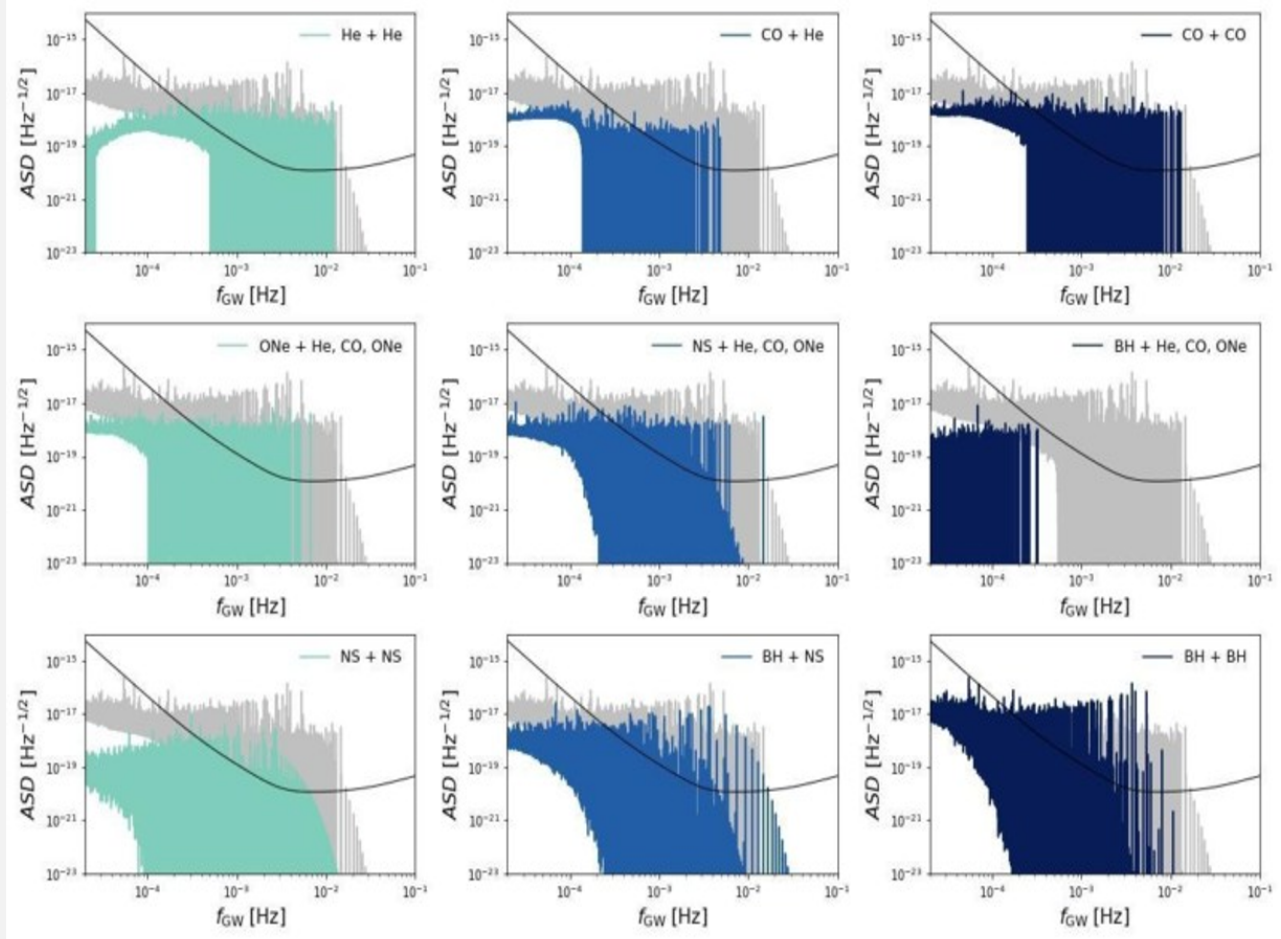
How does the observed data (black dots) in the figure compare to the theoretical models across different wavelength bands, and what does this comparison suggest about the nature of the observed event?

Answer:

The observed data closely follows the theoretical models, particularly those by Barnes et al. and Metzger, across multiple wavelength bands (g, r, i, z, y, J, H, K). This alignment suggests that the observed event exhibits characteristics consistent with kilonova models, supporting the connection between gravitational waves and kilonovae from neutron star mergers.

Figure 39. Example for KB-inference question-answer pair.

KB-Inference Example



Question:

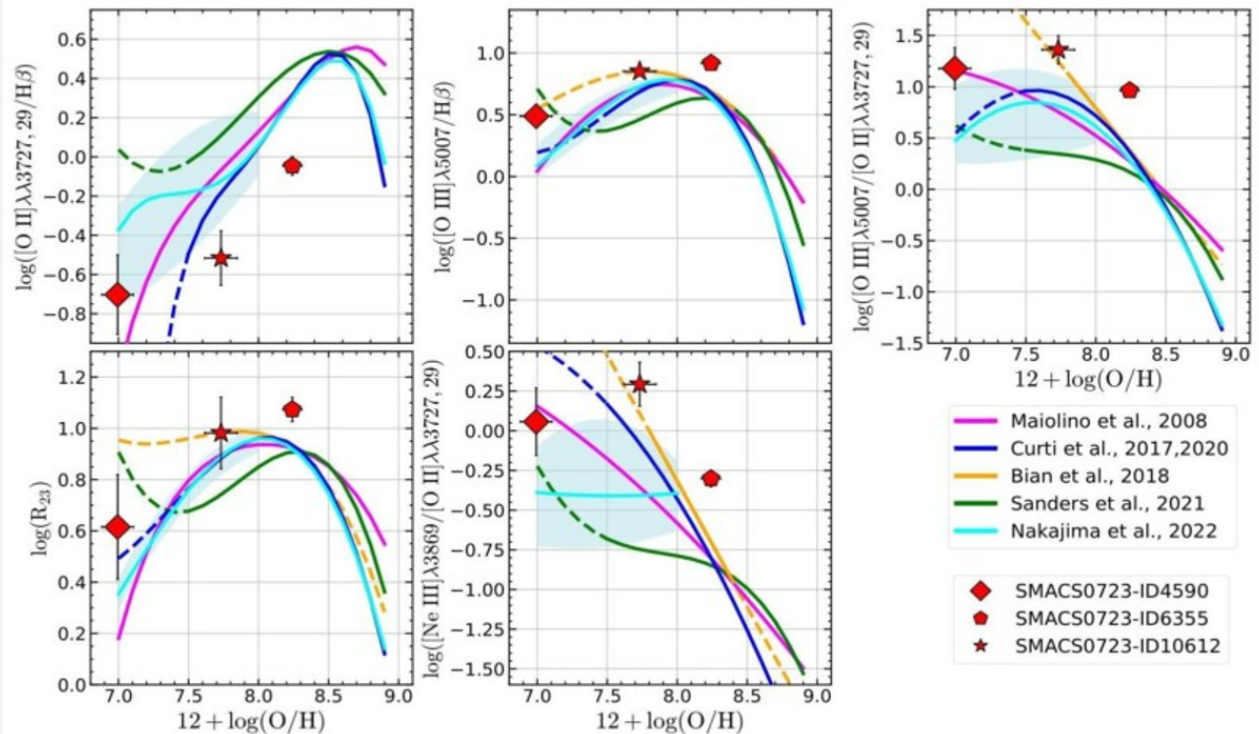
How does the gravitational wave frequency range differ between binary systems containing at least one black hole compared to those without black holes?

Answer:

Binary systems with at least one black hole (BH + He, CO, ONe; BH + NS; BH + BH) show stronger signals at lower frequencies (10^{-4} to 10^{-3} Hz) compared to systems without black holes. This indicates that black hole binaries emit more powerful low-frequency gravitational waves.

Figure 40. Example for KB-inference question-answer pair.

KB-Summary Example



Question:

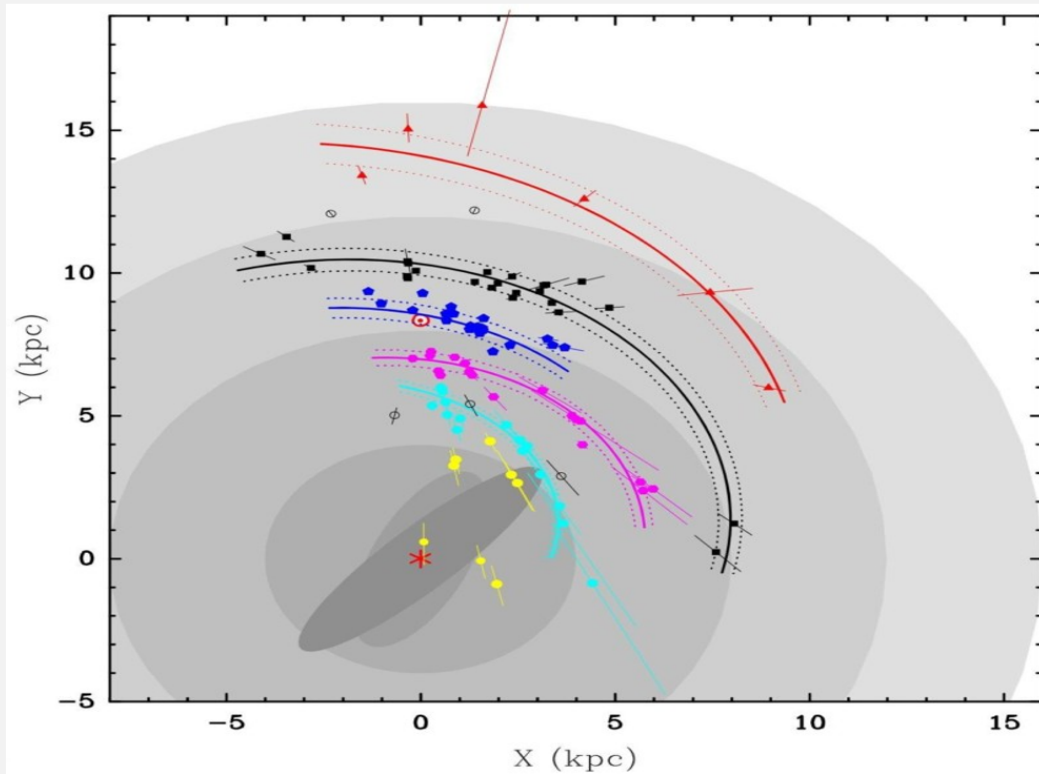
Provide the most important conclusion or inference from this chart

Answer:

The figure presents relationships between various strong-line ratios and metallicity for high-redshift galaxies observed by JWST. It compares these observations (red symbols) with several widely-used abundance calibrations derived from local galaxies (colored lines). Across all panels, there is a clear discrepancy between the observed data points and the predicted trends from existing calibrations. The high-redshift galaxies consistently fall outside the expected ranges, particularly at lower metallicities. This divergence suggests that current strong-line metallicity calibrations may not accurately represent the conditions in early universe galaxies, highlighting the need for recalibration when studying high-redshift objects.

Figure 41. Example for KB-summary question-answer pair.

KB-Summary Example



Question:

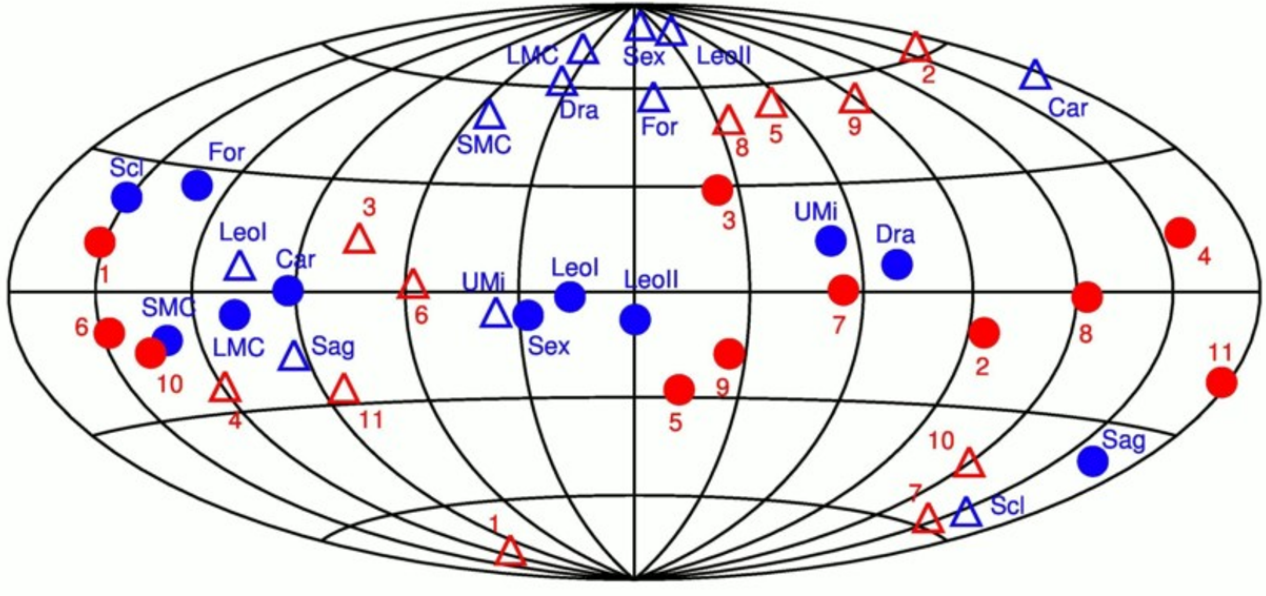
Provide the most important conclusion or inference from this chart

Answer:

The figure presents a top-down view of the Milky Way galaxy, showcasing the distribution of high-mass star forming regions (HMSFRs) across various spiral arms. Colored symbols represent HMSFRs in different arms, with their positions determined by trigonometric parallax measurements. The chart clearly illustrates the spiral structure of our galaxy, with distinct arms curving outward from the galactic center. This visual representation of HMSFR locations provides compelling evidence for the existence and layout of spiral arms in the Milky Way, offering a comprehensive map of our galaxy's structure based on precise distance measurements.

Figure 42. Example for KB-summary question-answer pair.

KB-Summary Example



Question:

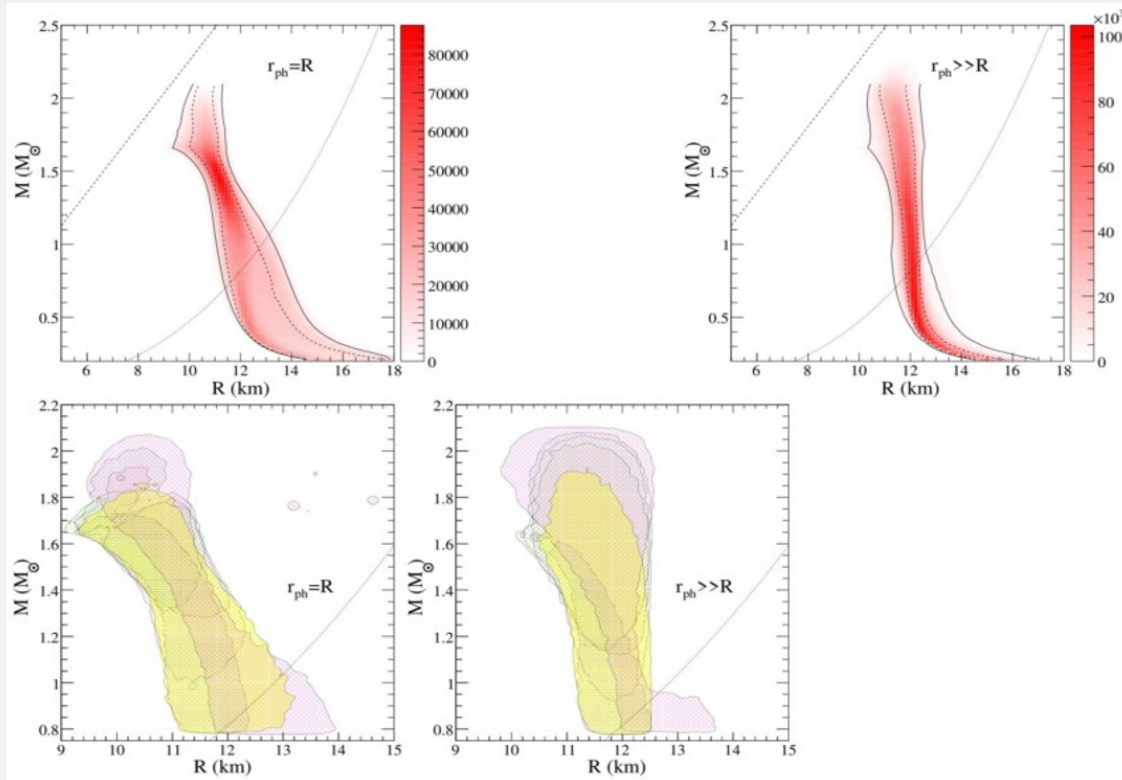
Provide the most important conclusion or inference from this chart

Answer:

The figure compares the spatial distribution and angular momentum of satellite galaxies in a simulated Milky Way-like system (red) with observed Milky Way satellites (blue). Both sets of satellites show a similar planar arrangement, with several exhibiting coherent rotation. The simulated system demonstrates that highly anisotropic satellite distributions, like those observed in the Milky Way, can occur within the Λ CDM framework. This alignment between simulation and observation suggests that the perceived "planes of satellites" issue may be explained by current models without requiring fundamental changes to Λ CDM cosmology.

Figure 43. Example for KB-summary question-answer pair.

KB-Summary Example



Question:

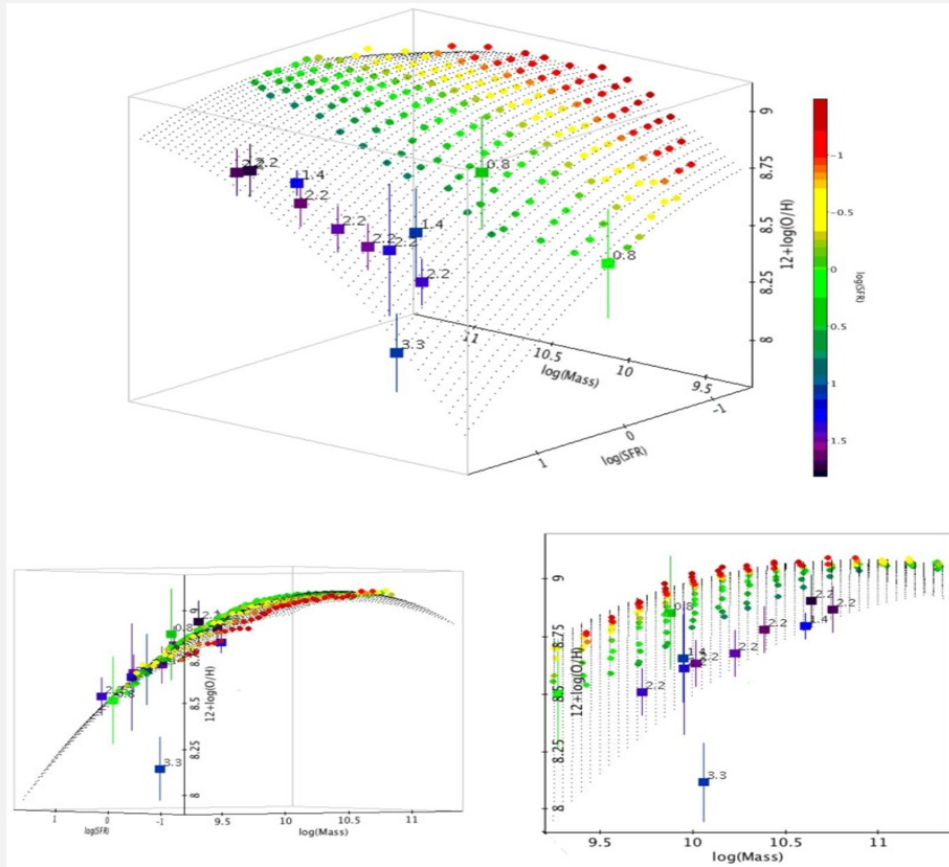
Provide the most important conclusion or inference from this chart

Answer:

The figure presents mass-radius relationships for neutron stars under two conditions: $r_{ph} = R$ and $r_{ph} \gg R$. The upper panels show probability distributions with 1σ and 2σ contours, while the lower panels display 2σ distributions for six specific objects. For 1.4 solar mass stars, radii cluster around 11-12 km. The graphs indicate a trend towards smaller radii as mass increases beyond 1.3-1.4 solar masses. The overlapping distributions in the lower panels demonstrate how multiple measurements constrain individual mass-radius estimates, providing insights into the equation of state for dense matter in neutron stars.

Figure 44. Example for KB-summary question-answer pair.

KB-Summary Example



Question:

Provide the most important conclusion or inference from this chart

Answer:

The figure presents a three-dimensional relationship between stellar mass, star formation rate (SFR), and gas-phase metallicity in galaxies. Colored dots represent local SDSS galaxies, forming a tight surface in the 3D space. Square dots with error bars indicate high-redshift galaxies at various redshifts. The lower-left projection shows most high-redshift data points aligning with the surface defined by local galaxies. The lower-right projection, representing the mass-metallicity relation, demonstrates how increasing SFR at higher redshifts explains the observed metallicity evolution up to $z=2.5$. This visualization effectively illustrates the interconnected nature of these galactic properties across cosmic time.

Figure 45. Example for KB-summary question-answer pair.

E. Expert Proofreading Website Screenshot

We developed a website (Fig. 46) for question-answer pair validation. Validators can log into the website to review the question-answer pairs along with the corresponding research paper excerpts. They can assess the professionalism and accuracy of the pairs by providing scores. If any errors are found, validators can input the correct information as a comment.

AstroCQA Proofreading Annotation

Enter Question ID
0

Question Id: 2527

url

field

title
Massive binaries as the source of abundance anomalies in globular clusters

abstract
Abundance anomalies observed in globular cluster stars indicate pollution with material processed by hydrogen burning. Two main sources have been suggested: asymptotic giant branch (AGB) stars and massive stars rotating near the break-up limit (spin stars). We propose massive binaries as an alternative source. We compute the evolution of a 20 M_{\odot} star in a close binary and find that it sheds about 10 M_{\odot} . The ejecta are enriched in He, N, Na, and Al and depleted in C and O, similar to the abundance patterns observed in globular cluster stars. In contrast to the fast, radiatively driven winds of massive stars, this material is typically ejected with low velocity. We expect that it remains inside the potential well of a globular cluster and becomes available for the formation or pollution of a second generation of stars. We estimate that the amount of processed low-velocity material ejected by massive binaries is greater than the contribution of AGB stars and spin stars combined, assuming that the majority of massive stars in a proto-globular cluster interact. If we take the possible contribution of intermediate mass stars in binaries into account and assume that the ejecta are diluted with an equal amount of unprocessed material, we find that this scenario can provide enough material to form a second generation of low-mass stars, which is as numerous as the first generation of low-mass stars. In this scenario there is no need to make commonly adopted assumptions, such as preferential loss of the first generation of stars, external pollution of the cluster, or an anomalous initial mass function. [Abridged]

summary
We propose massive binaries as a source for the internal pollution of globular clusters. The majority of massive stars are expected to be members of interacting binary systems. These return most of the envelope of their primary star to the interstellar medium during non conservative mass transfer. We show that there may be more polluted material ejected by binaries than by the two previously suggested sources: massive AGB stars and the slow winds of fast-rotating massive stars. After dilution with pristine material, as lithium observations suggest, binaries could return enough material to form a chemically enriched second generation that is as numerous as the first generation of low-mass stars, without the need to assume a highly anomalous IMF, external pollution of the cluster or a significant loss of stars from the unenriched first generation.
In addition to providing a new source of slowly-ejected enriched material, binary interaction also affects the previously proposed scenarios. Binary mass transfer naturally produces a large number of fast-rotating massive stars that may enrich their surroundings even more. Binary interaction will also affect the yields of intermediate-mass stars. Premature ejection of the envelope in 4-9 M_{\odot} stars will result in ejecta with less pronounced anti-correlations, as suggested in the AGB scenario. On the other hand, we expect that binary-induced mass loss may also prevent the dredge-up of helium-burning products.
For a detailed comparison of the chemical predictions of this scenario, binary models [for a range of masses and orbital periods] are needed and population synthesis models are essential to fully evaluate the mass budget of the different sources. [Finally, some peculiar feature, such as the apparent presence of distinct, chemically homogeneous subpopulations in [Lecendre&HGE2008](#) (citep[e.g.,]] [Renzini08] deserves further attention.]

caption
Caption: Composition of the slow ejecta of the modeled binary system (Sec.-3) as a function of the ejected amount of mass. The mass fraction X_i of the main stable isotope of each element is given relative to the initial mass fraction $X_{i,0}$, except for Mg where we added ^{24}Mg , ^{25}Mg and ^{26}Mg . The average X_{av} and the most extreme mass fraction X_{ex} are given in each panel on a logarithmic scale: $|X_i| \equiv \log_{10}(X_i/X_{i,0})$. For helium we show the absolute mass fraction Y instead. Mass ejected during the first and second mass transfer phases is separated by a thin vertical line. (label[fig:chem])

related conclusion for figure
The figure supports the conclusion that massive binary stars can eject large amounts of processed material with low velocity, which remains within the cluster's potential well. This material is enriched in He, N, Na, and Al, and depleted in C and O, matching observed patterns in globular cluster stars. The figure provides direct evidence for the chemical composition changes proposed in the paper's conclusion, supporting the idea that massive binaries could be a significant source of abundance anomalies in globular clusters.

question
How does the abundance of nitrogen in the ejected material change as the ejected mass increases, and what implications does this have for globular cluster composition?

answer
The graph shows nitrogen abundance increasing significantly with ejected mass, reaching $[X_{nv}] = 0.98$ and $[X_{no}] = 1.44$. This indicates that as massive binary stars eject more material, it becomes increasingly enriched in nitrogen, potentially contributing to the nitrogen enhancement observed in globular cluster stars.

Professionalism (Does the question reflect the perspective of an astronomer? 1 = least professional, 5 = most professional)
 null 1 2 3 4 5

Accuracy
 null Correct Unknown Incorrect

Submit

Figure 46. Screenshot of the expert proofreading website for QA validation, where validators review question-answer pairs with research excerpts, rate professionalism, and accuracy, and provide corrections or comments.

F. Details of MLLMs in Evaluation

Tab. 5 summarizes the architecture configurations of the current mainstream open-source MLLMs used for evaluating AstroChart, including model names, Hugging Face checkpoints (HF Checkpoint), LLM branches, and visual branches.

Models	HF Checkpoint	LLM Branch	Visual Branch
TinyChart-3B	mPLUG/TinyChart-3B-768	Phi-2	TinyChart-3B-768-siglip
Deepseek-Janus-Pro-7B	deepseek-ai/Janus-Pro-7B	DeepSeek-LLM-7b	SigLIP-L-384
Llava1.5-7B	liuhaotian/llava-v1.5-7b	Vicuna-13B	CLIP ViT-L-14-336
Llava1.6-Mistral-7B	liuhaotian/llava-v1.6-mistral-7b	Mistral-7B	CLIP ViT-L-14-336
Qwen-VL-Chat-7B	Qwen/Qwen-VL-Chat	Qwen-7B	Openclip ViT-bigG
MiniCPM-Llama3-V2.6-8B	openbmb/MiniCPM-V-2.6	Qwen-7B	SigLip-400M
InternVL2-8B	OpenGVLab/InternVL2-8B	internlm2.5-7b-chat	InternViT-300M-448px
mPLUG-Owl2-8.2B	MAGAer13/mplug-owl2-llama2-7b	LLaMA-7B	ViT-L -0.3B
Llava1.6-Vicuna-13B	liuhaotian/llava-v1.6-vicuna-13b	Vicuna-13B	CLIP ViT-L-14-336
SPHINX-v2-13B	Alpha-VLLM/LLaMA2-Accessory	LLaMA2-13B	DINOv2 ViT-g14 & OpenCLIP ConvNeXt-XXL
Cogvlm2-19B	THUDM/cogvlm2-llama3-chat-19B	Meta-Llama-3-8B-Instruct	EVA2-CLIP-E
Llava1.6-Yi-34B	liuhaotian/llava-v1.6-34b	Nous-Hermes-2-Yi-34B	CLIP ViT-L-14-336
Pixtral-large-124B	mistralai/Pixtral-Large-Instruct-2411	Mistral-Large-Instruct-2407	PixtralViT

Table 5. Open-source MLLM architecture

G. Details of Evaluation Metrics

In this appendix, we detail the evaluation framework used to assess both numerical responses and open-ended responses, as described in the main text.

G.1. Evaluation of Numerical Responses

For numerical responses, we categorize evaluation into data retrieval and data derivation. Data retrieval focuses on extracting specific data points or value ranges from charts. Data derivation involves structural element prediction (e.g., number of bars, colors, legends) and math reasoning.

Data Retrieval Evaluation. To ensure a scale-aware evaluation, we normalize the relative error using the axis range. The scoring process follows Algorithm 3.

Algorithm 3 Numerical Value Extraction and Scoring

Require: Reference values, Predicted values

Ensure: Final Score as S_{final}

```

1: procedure SCOREVALUES(Reference, Prediction)
2:   Extract numerical values from both Reference and Prediction
3:   if Number of reference values > Number of predicted values then
4:     return  $S_{final} = 0$ 
5:   else if Number of predicted values > Number of reference values then
6:     Compute the mean of predicted values
7:   end if
8:   Construct pairs  $V_i = \{(\text{Predict}_i, \text{True}_i)\}$ 
9:   if Chart axis is logarithmic then
10:    Apply logarithmic transformation (or retain exponent)
11:  end if
12:  Initialize  $S_{final} = 0$ 
13:  for each pair  $V_i$  do
14:    Compute relative error  $R_i$ :

```

$$R_i = \frac{|\text{True}_i - \text{Predict}_i|}{D_{range}}$$

where D_{range} is length of the axis.

```

15:    Compute Score  $S_i$ :

```

$$S_i = (1 - R_i) \times I((1 - R_i) > 0.9)$$

```

16:    Accumulate Score

```

```

17:  end for

```

```

18:  Compute Final Score:

```

$$S_{final} = \frac{1}{N} \sum_{i=1}^N \text{Score}_i$$

```

19:  return  $S_{final}$ 

```

```

20: end procedure

```

Data Derivation Evaluation. For data derivation, an LLM extracts numerical values, and correctness is determined by exact numerical matching, ensuring that only fully correct answers are considered accurate.

G.2. Evaluation of Open-ended Responses

We employ an LLM-based judging framework to evaluate open-ended responses. A dedicated judging model assigns a score between 0 and 1 based on predefined criteria, ensuring consistency and scalability. Our approach first extracts key points from both the generated and reference answers, then performs fine-grained matching to assess correctness. The final score is computed using an averaging strategy, providing a more nuanced evaluation. The evaluation prompt design is illustrated in Fig. 47.

Prompt for Evaluation MLLM

You will receive a question, a standard answer, and a model's response. Your task is to assess whether the model's response is correct.

Criteria:

Accuracy (0-1): Evaluate how closely the model's response matches the standard answer.

Final Score: Calculate the average score for all key points.

Steps:

- 1. Understand the Question:** Read and comprehend the question.
- 2. Analyze the Answers:** Read the standard answer and the model's response. Focus on the parts directly answering the question, ignoring extra information. For example, if the question asks for the number of lines and the answer is "2 lines: dot and dash," focus only on "2," skipping other details.
- 3. Compare Responses:** Evaluate similarities and differences between the model's response and the standard answer. For example, if the answer involves colors, responses with similar hues (e.g., blue vs. purple) should be rated higher.
- 4. Assign Accuracy Scores (0-1) for Each Key Point:**
 - 1:** Identical or nearly identical.
 - 0.8-0.9:** Thematically aligned with minor differences.
 - 0.5-0.7:** Partially correct with errors.
 - 0.3-0.4:** Loosely related with some relevant information.
 - 0.1-0.2:** Minimal relevant information.
 - 0:** Completely inaccurate; numerical/OCR responses must match exactly.

Omitted Key Points: If a key point is completely missing from the model's response, it receives a score of 0.
- 5. Compute the Final Score:** Calculate the average accuracy score for all key points.

Example 1:

Question: What line styles are used for A and B?

Standard answer: Blue dash-dot line and red dot line.

Model's response: Dash-dot line style for A and dot line for B.

You should response: 1

Another model's response: Dashed and dot.

You should response: 0.5

Example 2:

Question: What is the title used for the y-axis in the chart?

Standard answer: The y-axis is labeled as $E(v_n)$.

Model's response: $E(r_n)$

You should response: 0

Another model's response: $E(v)$.

You should response: 0

Now start the evaluation:

Question:

{question}

Standard Answer:

{answer}

Model's Response:

{pred}

Your response (score ONLY without reason):

Figure 47. Prompt for evaluation MLLMs.

H. Other Evaluation Metrics and Results

We further evaluate the models using L3Score(Tab. 6), BLEU-4(Tab. 7), and ROUGE-L(Tab. 8), which are commonly used metrics for assessing text generation quality. L3Score captures semantic alignment in long-form answers, BLEU-4 evaluates n-gram precision, and ROUGE-L measures lexical overlap. In the following tables, bold numbers indicate the best-performing model among proprietary and open-source MLLMs, respectively.

Models	Fundamental Question								Advanced Question				Overall	
	Visual					Data			Inference	Summary	KB-Inference	KB-Summary		
	All	Color	Style	Text	Layout	All	Point	Interval						Calculation
Proprietary Multimodal Large Language Models														
GPT-4o	78.14%	75.22%	74.40%	82.13%	81.37%	53.40%	58.65%	61.69%	35.22%	74.04%	81.12%	52.77%	67.02%	70.10%
GLM-4V	68.88%	68.46%	59.19%	74.61%	71.69%	32.79%	31.85%	44.20%	20.39%	43.83%	30.72%	24.02%	15.18%	43.03%
GLM-4V-Plus	65.10%	64.58%	52.74%	73.07%	65.76%	41.63%	44.64%	50.18%	26.57%	50.46%	26.03%	40.00%	43.04%	47.92%
Qwen-VL-Max	61.02%	59.25%	47.30%	69.04%	69.41%	42.59%	40.02%	48.58%	39.31%	59.78%	71.62%	43.78%	58.31%	57.36%
Open-source Multimodal Large Language Models														
TinyChart-3B	23.46%	36.81%	16.05%	15.07%	20.07%	13.35%	20.64%	11.80%	3.95%	8.77%	0.05%	1.07%	0.00%	11.17%
Deepseek-Janus-Pro-7B	58.00%	60.14%	56.43%	56.16%	60.52%	30.51%	34.75%	39.98%	12.45%	43.49%	26.48%	1.07%	9.09%	37.62%
Llava1.5-7B	16.80%	22.13%	13.93%	13.26%	15.47%	10.09%	11.80%	9.45%	8.24%	28.84%	1.03%	8.78%	0.00%	12.54%
Llava1.6-Mistral-7B	33.41%	40.79%	25.68%	30.18%	34.04%	13.29%	16.99%	11.74%	9.44%	27.32%	0.38%	12.57%	0.01%	18.43%
Qwen-VL-Chat-7B	35.19%	39.67%	30.13%	32.01%	41.08%	12.73%	17.69%	8.22%	10.53%	25.12%	0.69%	9.65%	0.14%	18.32%
MiniCPM-Llama3-V2.6-8B	63.93%	64.10%	55.91%	69.45%	57.90%	31.39%	29.32%	45.22%	17.78%	39.46%	29.08%	26.62%	16.38%	40.68%
InternVL2-8B	38.06%	39.98%	28.46%	42.31%	34.27%	23.05%	23.61%	29.19%	14.73%	32.68%	2.56%	15.98%	0.21%	23.09%
mPLUG-Owl2-8.2B	18.17%	21.35%	16.07%	16.11%	17.59%	8.63%	10.38%	8.01%	6.67%	22.51%	0.65%	9.21%	0.00%	11.75%
Llava1.6-Vicuna-13B	38.77%	47.64%	32.01%	35.33%	29.90%	13.96%	19.30%	10.54%	9.87%	27.70%	0.73%	10.77%	0.01%	20.18%
SPHINX-v2-13B	24.17%	32.22%	21.69%	19.18%	14.94%	8.15%	14.85%	1.47%	5.89%	23.82%	0.46%	9.56%	0.00%	13.79%
CogVLM2-19B	57.40%	64.72%	38.90%	62.78%	52.19%	28.68%	32.09%	38.42%	11.56%	38.95%	18.33%	19.31%	4.55%	34.44%
Llava1.6-Vi-34B	41.51%	50.55%	33.03%	39.00%	32.34%	21.48%	19.91%	25.86%	18.57%	33.73%	2.39%	20.97%	0.96%	24.66%
Pixtral-large-124B	79.58%	75.22%	72.85%	86.66%	83.60%	55.32%	57.49%	64.03%	41.37%	72.52%	82.26%	46.81%	63.31%	69.85%

Table 6. Evaluation on AstroChart benchmark using L3Score.

Models	Fundamental Question								Advanced Question				Overall	
	Visual					Data			Inference	Summary	KB-Inference	KB-Summary		
	All	Color	Style	Text	Layout	All	Point	Interval						Calculation
Proprietary Multimodal Large Language Models														
GPT-4o	23.98%	25.40%	21.42%	25.91%	14.67%	13.82%	16.55%	12.31%	11.42%	13.28%	12.35%	15.83%	4.96%	16.10%
GLM-4V	11.52%	10.77%	10.23%	13.05%	10.93%	8.60%	10.94%	8.10%	5.59%	7.32%	6.84%	11.58%	1.92%	8.73%
GLM-4V-Plus	14.73%	16.78%	8.52%	17.62%	8.95%	9.51%	9.29%	8.62%	10.91%	16.71%	7.26%	14.08%	3.39%	11.81%
Qwen-VL-Max	13.87%	13.87%	9.26%	17.84%	8.20%	11.80%	13.94%	10.86%	9.62%	10.88%	11.94%	16.05%	2.57%	11.91%
Open-source Multimodal Large Language Models														
TinyChart-3B	3.23%	5.98%	1.57%	2.06%	0.78%	0.84%	0.18%	1.40%	1.18%	4.12%	1.60%	4.97%	1.66%	2.74%
Deepseek-Janus-Pro-7B	10.55%	9.98%	11.01%	11.43%	7.09%	10.40%	12.93%	8.82%	8.40%	11.59%	9.48%	12.90%	2.95%	10.03%
Llava1.5-7B	1.78%	3.21%	0.41%	1.44%	0.62%	4.89%	2.02%	0.78%	14.31%	15.12%	3.75%	9.42%	2.06%	5.49%
Llava1.6-Mistral-7B	5.46%	7.87%	1.85%	5.69%	3.52%	4.90%	7.86%	3.43%	2.11%	2.70%	3.45%	4.04%	1.46%	4.09%
Qwen-VL-Chat-7B	2.77%	2.42%	0.75%	4.64%	1.37%	1.33%	1.19%	1.48%	1.37%	13.54%	5.71%	7.31%	2.79%	5.13%
MiniCPM-Llama3-V2.6-8B	11.94%	11.86%	8.13%	16.23%	3.26%	6.49%	4.73%	7.79%	7.63%	9.61%	7.89%	12.48%	5.31%	9.45%
InternVL2-8B	10.45%	10.91%	9.51%	11.38%	6.09%	7.85%	8.92%	7.12%	7.10%	9.18%	4.83%	9.38%	0.60%	7.87%
mPLUG-Owl2-8.2B	2.18%	2.94%	0.66%	2.50%	1.51%	5.11%	1.57%	1.22%	15.32%	14.45%	3.33%	8.16%	1.24%	5.27%
Llava1.6-Vicuna-13B	5.36%	7.84%	1.24%	6.18%	1.95%	5.02%	1.19%	1.34%	15.40%	13.06%	3.98%	9.80%	1.43%	6.35%
SPHINX-v2-13B	1.52%	2.12%	0.39%	1.82%	0.58%	1.81%	0.67%	0.07%	5.67%	12.84%	3.15%	8.61%	0.76%	4.24%
CogVLM2-19B	11.15%	9.29%	7.58%	16.32%	5.51%	7.54%	6.02%	6.63%	10.99%	13.48%	8.65%	10.06%	3.20%	9.63%
Llava1.6-Vi-34B	5.53%	8.37%	1.49%	5.74%	2.94%	5.29%	0.97%	2.87%	14.94%	14.00%	4.98%	10.99%	2.18%	6.96%
Pixtral-large-124B	22.27%	25.53%	17.59%	23.98%	12.11%	13.31%	14.62%	14.54%	9.78%	10.40%	13.13%	18.96%	6.21%	15.61%

Table 7. Evaluation on AstroChart benchmark using Bleu-4.

Models	Fundamental Question								Advanced Question				Overall	
	Visual					Data			Inference	Summary	KB-Inference	KB-Summary		
	All	Color	Style	Text	Layout	All	Point	Interval						Calculation
Proprietary Multimodal Large Language Models														
GPT-4o	54.34%	57.19%	53.06%	54.86%	42.12%	40.51%	43.32%	43.15%	32.97%	36.05%	30.51%	37.29%	20.33%	40.36%
GLM-4V	37.15%	36.60%	36.81%	38.31%	34.43%	29.01%	31.13%	32.92%	20.97%	26.77%	23.17%	31.80%	13.29%	29.12%
GLM-4V-Plus	38.31%	42.84%	28.70%	41.95%	29.10%	29.60%	25.52%	34.87%	29.50%	41.23%	24.28%	35.02%	17.90%	32.75%
Qwen-VL-Max	38.57%	40.93%	34.17%	39.57%	35.66%	34.25%	35.31%	37.76%	28.33%	31.93%	30.01%	36.39%	14.15%	32.89%
Open-source Multimodal Large Language Models														
TinyChart-3B	12.25%	20.19%	8.21%	7.37%	9.93%	6.52%	11.34%	8.51%	16.69%	13.51%	21.15%	15.57%	13.43%	
Deepseek-Janus-Pro-7B	34.15%	32.22%	34.55%	36.08%	32.87%	30.93%	32.01%	32.99%	26.77%	33.69%	27.35%	33.69%	17.40%	30.80%
Llava1.5-7B	8.20%	15.41%	2.92%	5.29%	3.57%	14.95%	5.32%	8.21%	38.03%	39.59%	20.45%	29.83%	17.66%	19.28%
Llava1.6-Mistral-7B	18.27%	25.11%	11.36%	16.36%	15.78%	16.86%	19.57%	19.27%	9.76%	11.86%	18.33%	17.47%	13.42%	16.52%
Qwen-VL-Chat-7B	13.65%	15.30%	7.92%	14.61%	17.50%	7.19%	4.49%	10.31%	7.58%	35.39%	22.58%	28.55%	19.06%	19.42%
MiniCPM-Llama3-V2.6-8B	40.66%	45.29%	38.48%	41.28%	23.33%	27.47%	22.85%	34.75%	25.80%	30.56%	25.60%	32.47%	21.77%	31.83%
InternVL2-8B	34.04%	35.23%	32.74%	34.95%	26.61%	28.08%	28.03%	31.44%	24.07%	29.63%	21.37%	29.22%	10.51%	27.58%
mPLUG-Owl2-8.2B	9.80%	14.35%	6.28%	8.17%	6.67%	15.97%	5.51%	11.31%	37.81%	38.85%	20.53%	30.09%	16.18%	19.75%
Llava1.6-Vicuna-13B	17.90%	24.69%	8.88%	17.90%	13.64%	15.79%	3.71%	12.42%	38.58%	35.31%	19.83%	29.68%	13.58%	21.35%
SPHINX-v2-13B	8.93%	12.93%	3.83%	8.36%	8.09%	6.47%	1.73%	1.32%	20.05%	36.03%	19.37%	29.30%	15.15%	17.08%
CogVLM2-19B	33.30%	30.92%	27.90%	39.89%	28.22%	25.51%	19.21%	29.66%	30.21%	36.06%	26.37%	30.19%	20.10%	29.72%
Llava1.6-Vi-34B	21.09%	26.47%	13.50%	21.12%	18.27%	18.59%	6.20%	19.77%	36.36%	36.27%	21.56%	31.50%	15.83%	23.67%
Pixtral-large-124B	51.58%	54.68%	49.71%	51.93%	41.14%	37.26%	38.46%	42.90%	28.56%	31.15%	31.80%	39.72%	22.58%	38.87%

Table 8. Evaluation on AstroChart benchmark using Rouge-L.

I. Failure cases of AstroChart

I.1. Failure cases of Visual question-answer pair

Common errors in visual question-answer pair include incorrect color or pattern recognition and errors in counting or tallying (Fig. 48, Fig. 49, Fig. 50).

I.2. Failure cases of Data question-answer pair

Common errors in data question-answer pair include misreading the numbers. (Fig. 51, Fig. 52, Fig. 53).

I.3. Failure cases of Inference question-answer pair

Common errors in inference question-answer pairs include misinterpreting the question, providing incorrect answers, and making errors in identifying trends or comparisons. (Fig. 54, Fig. 55, Fig. 56).

I.4. Failure cases of Summary question-answer pair

Common errors in summary question-answer pair include incorrect descriptions of the chart's patterns and insufficiently comprehensive descriptions of the chart. (Fig. 57, Fig. 58, Fig. 59).

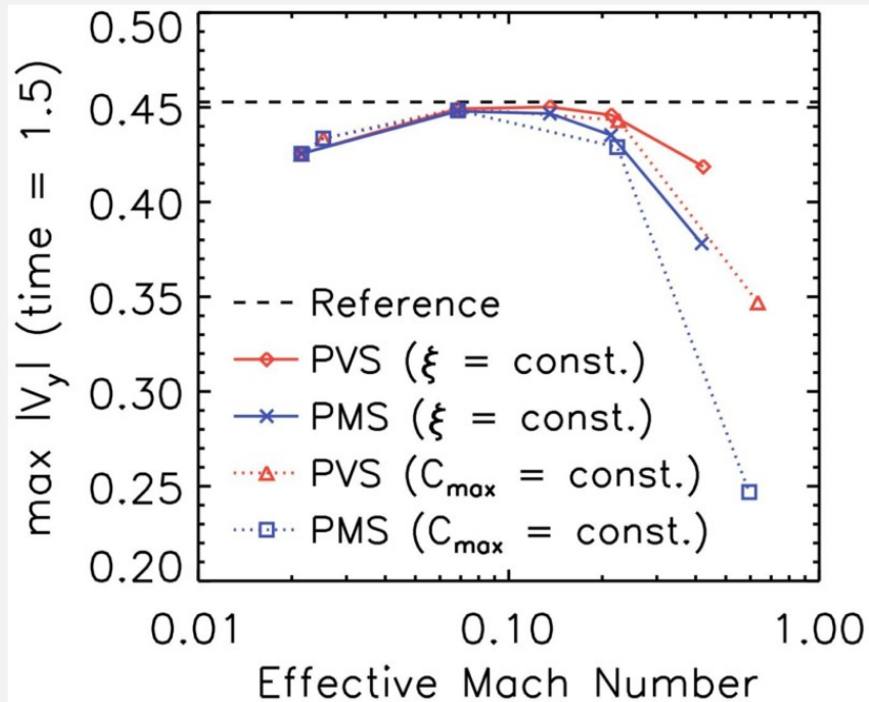
I.5. Failure cases of KB-Inference question-answer pair

Common errors in KB-Inference question-answer pairs include incomplete or incorrect summaries of the chart content and errors or omissions in the inferred conclusions. (Fig. 60, Fig. 61, Fig. 62).

I.6. Failure cases of KB-Summary question-answer pair

Common errors in KB-Summary question-answer pairs include incomplete or incorrect summaries of the chart content and the absence of a high-level summary. (Fig. 63, Fig. 64, Fig. 65).

Example



Question:

How many different line styles are used in the graph?

Answer:

Three line styles: solid, dashed and dotted.

GPT-4o: Four different line styles are used in the graph.

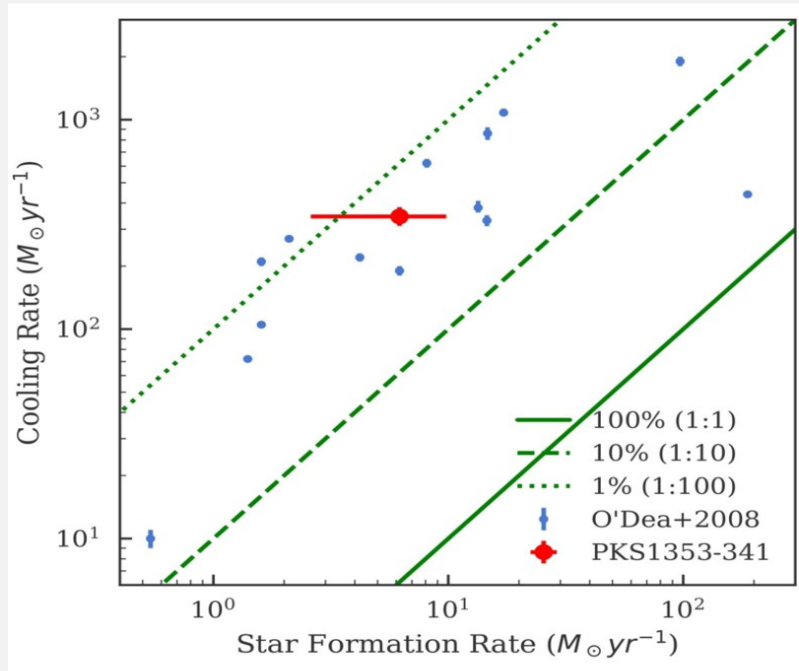
Pixtral-large: Four different line styles are used.

Minicpm: 4.

Deepseek-janus-pro-7b: There are four different line styles used in the graph.

Figure 48. Failure case for visual question-answer pair generation.

Example



Question:

What symbols are used to represent the data points in the chart?

Answer:

Blue dots for O'Dea+2008 data, red filled circle for PKS1353-341.

GPT-4o: Blue dots and a red **diamond**.

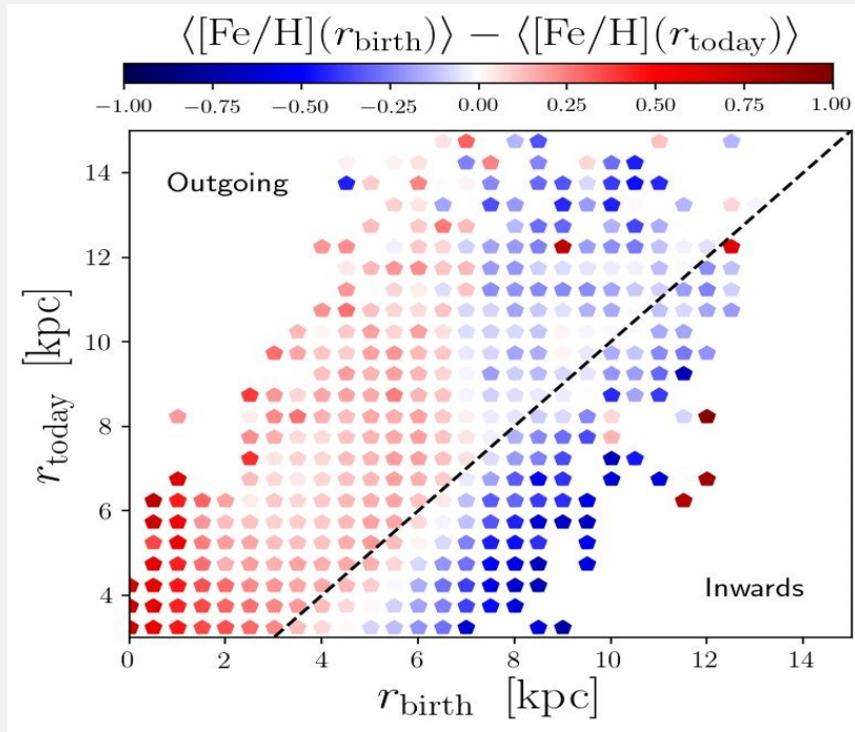
Minicpm: Blue **circles** and red **diamond**.

Pixtral-large: **Crosses**, circles and **square**.

Deepseek-janus-pro-7b: The symbols used to represent the data points in the chart are blue dots and a red **diamond**.

Figure 49. Failure case for visual question-answer pair generation.

Example



Question:

What shape is used to represent data points in the scatter plot?

Answer:

Pentagon-shaped markers are used to represent data points.

GPT-4o: Hexagon.

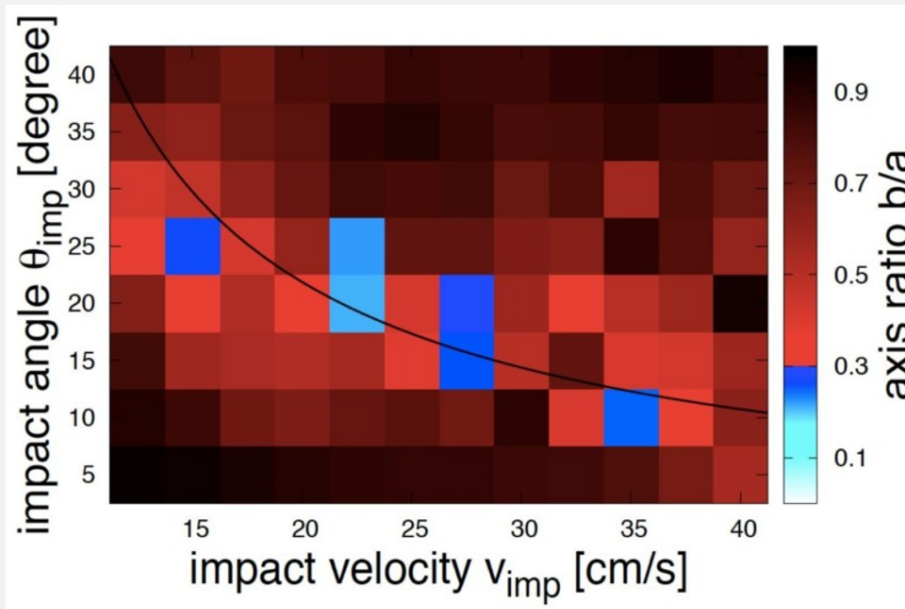
Minicpm: Hexagons.

Pixtral-large: Hexagons are used to represent data points.

Deepseek-janus-pro-7b: The shape used to represent data points in the scatter plot is hexagon.

Figure 50. Failure case for visual question-answer pair generation.

Example



Question:

At what combination of impact velocity and impact angle does the axis ratio b/a reach its lowest values?

Answer:

The axis ratio b/a reaches its lowest values at an impact angle of around 20 degrees and an impact velocity of 22.5 cm/s.

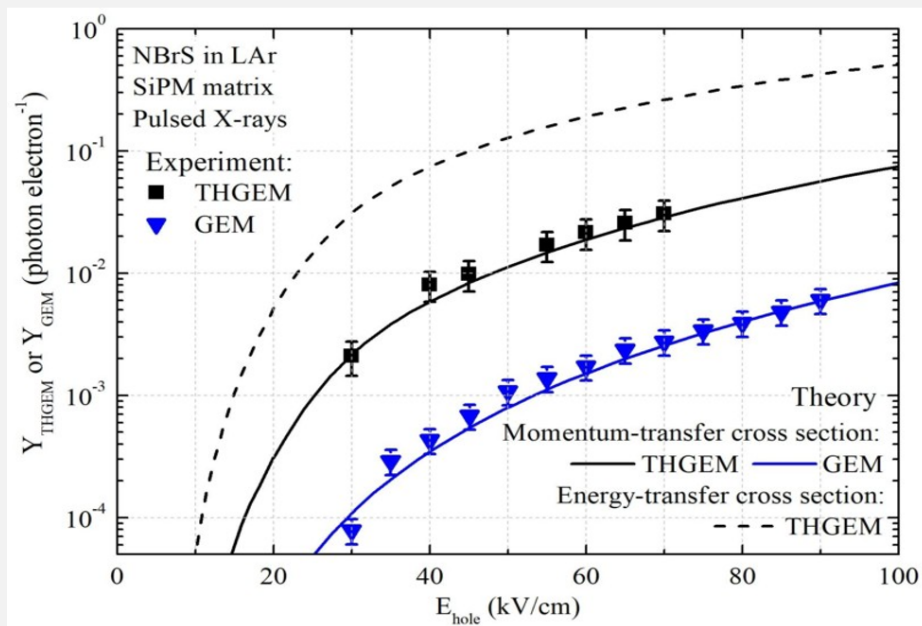
GPT-4o: The axis ratio (b/a) reaches its lowest values at an impact velocity of approximately **25 cm/s** and an impact angle of around **25 degrees**, as indicated by the darkest blue regions on the heatmap.

Minicpm: The lowest values of the axis ratio b/a are indicated by the lightest color, which is found in the lower right corner of the heatmap. This suggests that the combination of impact velocity and impact angle where the axis ratio reaches its lowest values occurs at an impact velocity of approximately **35 cm/s** and an impact angle of around 20 degrees.

Pixtral-large: The axis ratio b/a reaches its lowest values at an impact velocity of approximately **20-25 cm/s** and an impact angle of around **20-25 degrees**, as indicated by the blue regions in the heatmap.

Deepseek-janus-pro-7b: The axis ratio b/a reaches its lowest values at the intersection of the highest impact velocity (around **35 cm/s**) and the lowest impact angle (around **10 degrees**). This is indicated by the lightest blue color on the heatmap.

Example



Question:

At what E_{hole} value do the experimental THGEM data points start?

Answer:

Around 30 kV/cm.

GPT-4o: Approximately 20 kV/cm.

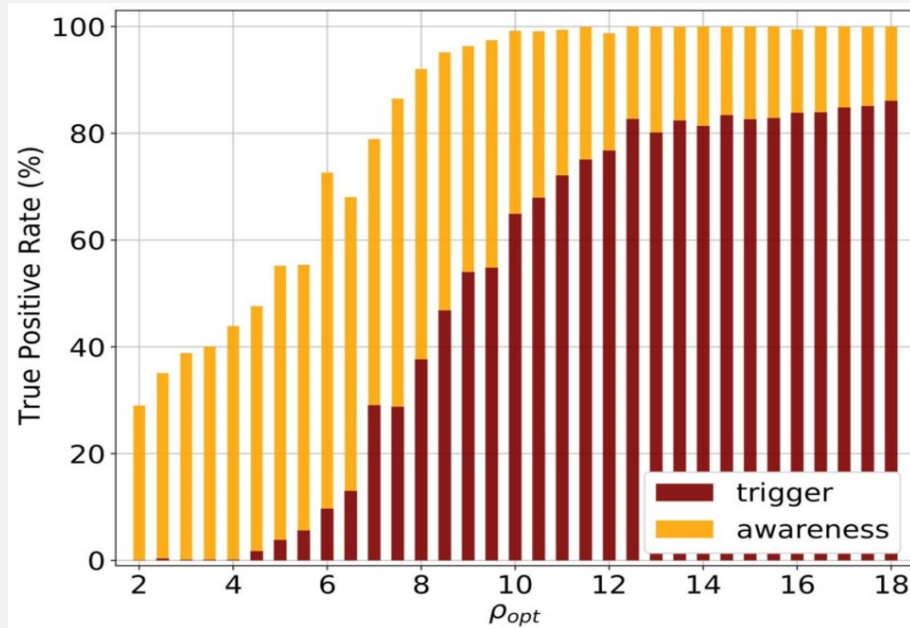
Minicpm: 20 kV/cm.

Pixtral-large: The experimental THGEM data points start at approximately 20 kV/cm.

Deepseek-janus-pro-7b: The experimental THGEM data points start at approximately 20 kV/cm.

Figure 52. Failure case for data question-answer pair generation.

Example



Question:

At what ρ_{opt} value does the total bar height first reach 100%?

Answer:

Around 11.5 on the x-axis.

GPT-4o: At ρ_{opt} value of 10, total bar height reaches 100%.

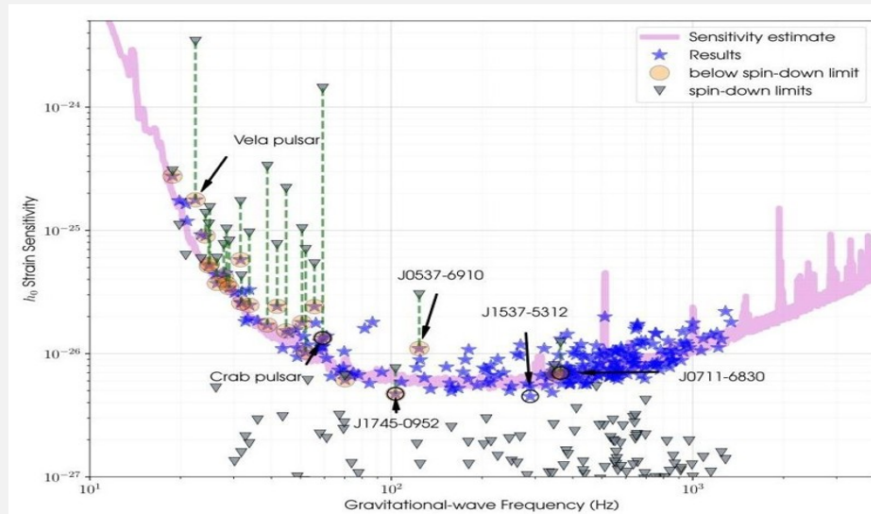
Minicpm: 16.

Pixtral-large: The total bar height first reaches 100% at ρ_{opt} value of 12.

Deepseek-janus-pro-7b: The total bar height first reaches 100% at ρ_{opt} value 10.

Figure 53. Failure case for data question-answer pair generation.

Example



Question:

How does the sensitivity estimate curve compare to the majority of the results?

Answer:

The sensitivity estimate curve (pink line) and the majority of the results (blue stars) essentially overlap.

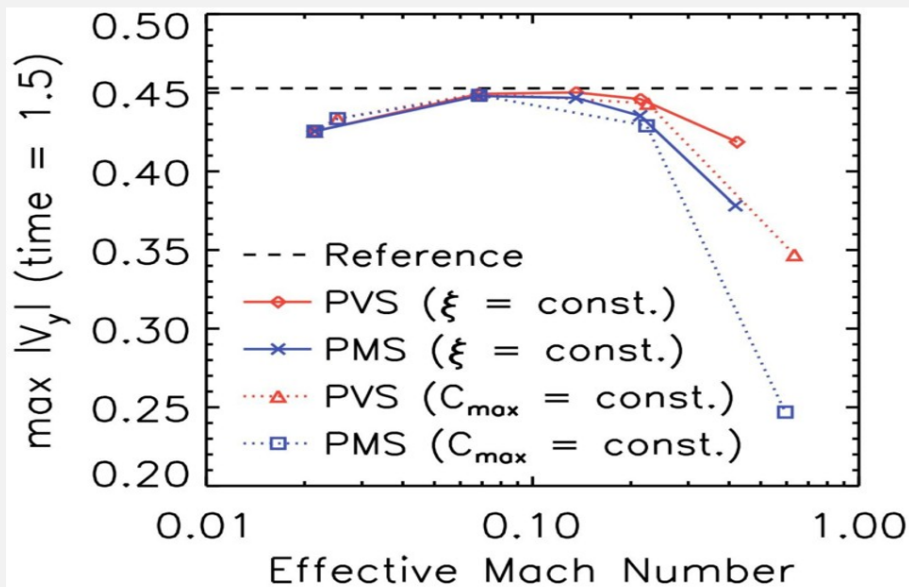
GPT-4o: The sensitivity estimate curve (pink) generally **lies above** the majority of the results (blue stars), indicating that the actual results are more sensitive than the estimated sensitivity across most of the gravitational-wave frequency range.

Minicpm: The sensitivity estimate curve **is above** the majority of the results, indicating that current sensitivity estimates for detecting gravitational waves from pulsars are higher than what has been observed in experiments.

Pixtral-large: The sensitivity estimate curve generally lies **above** the majority of the results, indicating that the actual measurements (blue stars) achieved better sensitivity than the estimated limits. This is particularly evident at frequencies between 10^1 and 10^3 Hz.

Deepseek-janus-pro-7b: The sensitivity estimate curve (purple) generally follows the trend of the results (blue stars) **but is consistently above them**, indicating higher sensitivity estimates than the majority of the results.

Example



Question:

How do the PVS and PMS curves compare at the highest Mach number?

Answer:

PVS curves have higher values than PMS curves at the highest Mach number.

GPT-4o: At the highest Mach number, both PVS and PMS curves show a significant drop, with PMS ($\xi = \text{const.}$) and PMS ($C_{\text{max}} = \text{const.}$) having lower values compared to their PVS counterparts.

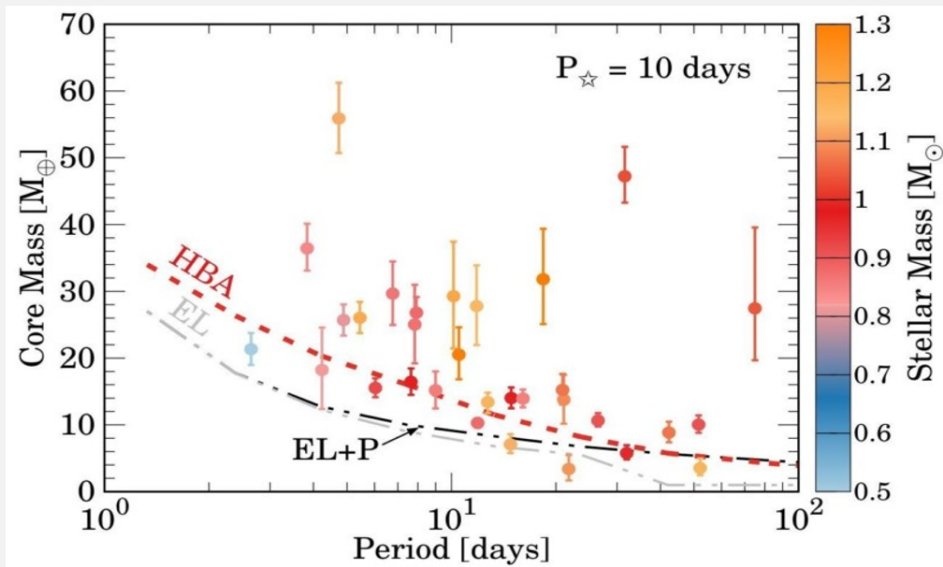
Minicpm: At the highest Mach number, the PVS and PMS curves for both const. and $C_{\text{max}} = \text{const.}$ conditions converge, indicating similar performance or behavior at this point.

Pixtral-large: At the highest Mach number, both PVS and PMS curves show a significant drop in the maximum absolute value of velocity ($|V_y|$). The PVS curve (red triangles) drops to approximately 0.35, while the PMS curve (blue squares) drops to around 0.25, indicating that PMS experiences a more pronounced decrease. (Missing the comparison between PVS and PMS)

Deepseek-janus-pro-7b: At the highest Mach number, the PVS and PMS curves show similar values, both slightly above 0.45.

Figure 55. Failure case for inference question-answer pair generation.

Example



Question:

How does the EL+P model compare to the HBA model at orbital periods greater than 40 days?

Answer:

The EL+P model agrees with the HBA model at orbital periods greater than 40 days, where mass loss is mostly due to boil-off.

GPT-4o: At orbital periods greater than 40 days, the EL+P model **predicts lower core** masses compared to the HBA model, as indicated by the black dashed line being below the red dashed line.

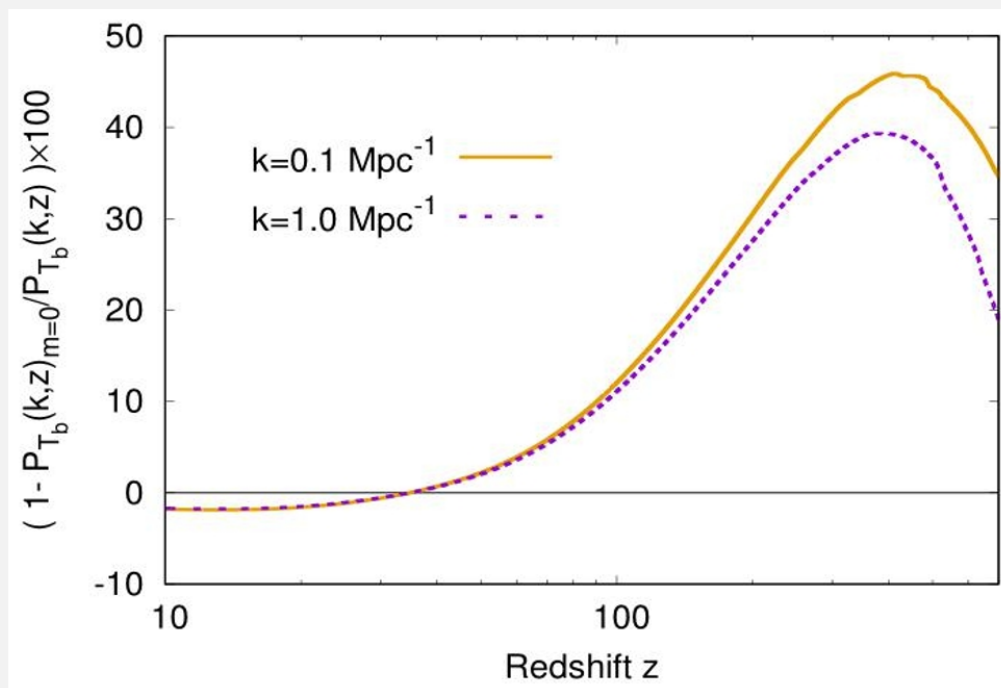
Minicpm: At orbital periods greater than 40 days, the EL+P model **lies above** the HBA model. This indicates that the core mass estimated by the EL+P model is higher than those predicted by the HBA model in this regime.

Pixtral-large: At orbital periods greater than 40 days, the EL+P model predicts **lower core** masses compared to the HBA model. The EL+P model's curve (black dashed line) remains below the HBA model's curve (red dashed line), indicating smaller core masses for longer periods.

Deepseek-janus-pro-7b: The EL+P model shows **a lower core** mass compared to the HBA model at orbital periods greater than 40 days, as indicated by the dashed lines and data points.

Figure 56. Failure case for inference question-answer pair generation.

Example



Question:

Generate a chart description that aims at presenting all the visual elements of the plot.

Answer:

This line graph shows the redshift evolution of changes in the HI 21-cm power spectrum due to inhomogeneous CMBR heating. It compares two k -modes: 0.1 and 1.0 Mpc^{-1} . Both curves start negative at low redshifts, rise steeply after $z=100$, peak around $z=300-400$, and then decline. The lower k -mode (0.1) shows a higher amplitude and peaks later than the higher k -mode (1.0). The y-axis represents percentage change, while the x-axis uses a logarithmic scale for redshift.

GPT-4o: The chart displays the relationship between redshift (z) and the quantity $((1 - \frac{P_{T_b}(k,z)}{P_{T_b}(k,z)_{m=0}}) \times 100)$. The x-axis represents the redshift (z) on a logarithmic scale from 10 to 100, while the y-axis ranges from -10 to 50. Two curves are plotted: a solid yellow line for $(k = 0.1 \text{ Mpc}^{-1})$ and a purple dashed line for $(k = 1.0 \text{ Mpc}^{-1})$. Both curves rise from near zero, peak, and then decline, with the yellow curve peaking higher and later than the purple one.

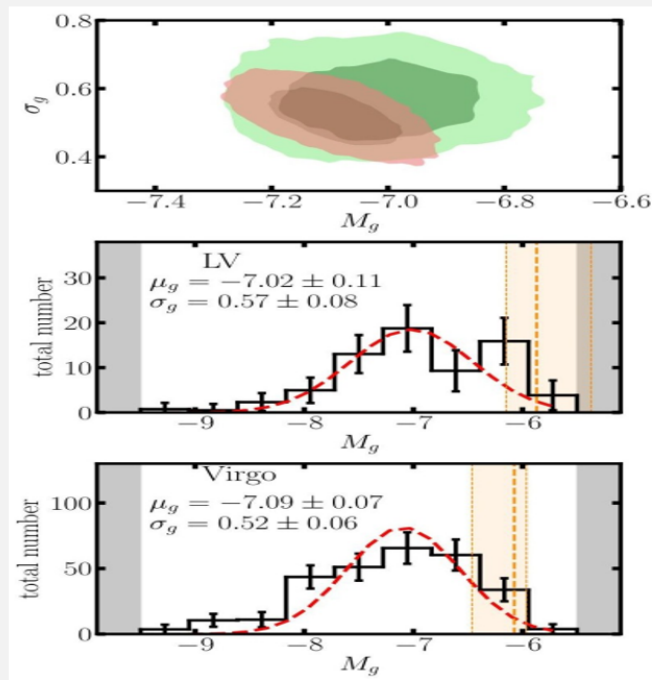
Minicpm: The graph displays a comparison of the probability (P_b) for two different values of k , which are 0.1 Mpc^{-1} and 1.0 Mpc^{-1} , as functions of redshift z . The y-axis represents the normalized probability difference from the mean, while the x-axis indicates the redshift range from 0 to approximately 250. Both lines show an increasing trend in probability with redshift up until around redshift 60-80, after which there is a decline followed by a rise again towards higher redshifts. The line for $k=0.1 \text{ Mpc}^{-1}$ starts at a lower value and increases more gradually compared to the line for $k=1.0 \text{ Mpc}^{-1}$, which begins higher and reaches a peak before declining. This suggests that the effect on P_b varies significantly depending on the scale k .

Pixtral-large: The chart is a line graph depicting the percentage change in a quantity, denoted as $(1 - P_{T,b}(k,z)/m=0/P_{T,b}(k,z))$, multiplied by 100, as a function of redshift (z) on a logarithmic scale. The x-axis represents redshift (z) ranging from 10 to 1000, while the y-axis shows the percentage change from -10 to 50. Two data series are plotted: a solid yellow line for $k=0.1 \text{ Mpc}^{-1}$ and a dashed purple line for $k=1.0 \text{ Mpc}^{-1}$. Both lines show an increasing trend, peaking around a redshift of 500, and then decreasing. The chart indicates that the percentage change is more pronounced at higher redshifts and varies with the value of k .

Deepseek-janus-pro-7b: The chart depicts the relationship between redshift (z) and the quantity $(1 - P_{10}(k,z)) \times k_{21}(z) \times P_{10}(k,z)$, with two curves representing different values of k . The solid orange line corresponds to $(k = 0.1 \text{ Mpc}^{-1})$, while the dashed purple line corresponds to $(k = 1.0 \text{ Mpc}^{-1})$. The x-axis is labeled "Redshift (z)" and spans from 10 to 1000, while the y-axis shows the values of the plotted quantity, ranging from -10 to 50. Both curves start near zero at low redshift values and rise to a peak before declining. The orange curve peaks slightly higher than the purple curve, indicating a difference in behavior between the two values of k .

Figure 57. Failure case for summary question-answer pair generation. (Continued)

Example



Question:

Generate a chart description that aims at presenting all the visual elements of the plot.

Answer:

The image consists of three panels. The top panel shows overlapping contour plots for LV (green) and Virgo (red) samples, representing confidence regions for GCLF parameters. The middle and bottom panels are histograms with Gaussian fits for LV and Virgo samples respectively, showing the distribution of globular cluster magnitudes. Each histogram includes statistical information and vertical dashed lines. The overall layout compares GCLF characteristics between the two samples.

GPT-4o: The chart consists of three panels. The top panel is a contour plot showing the relationship between (M_g) and (σ_g) with three nested regions in green, brown, and red. The middle and bottom panels are histograms of (M_g) for LV and Virgo, respectively, with total number on the y-axis. Both histograms feature black bars with error lines, red dashed Gaussian fits, and shaded regions on the left and right. The middle panel includes text annotations for (μ_g) and (σ_g) values. The x-axis is labeled (M_g) and the y-axis is labeled "total number." (Incomplete answer, missing the description of the vertical dashed lines in the histogram.)

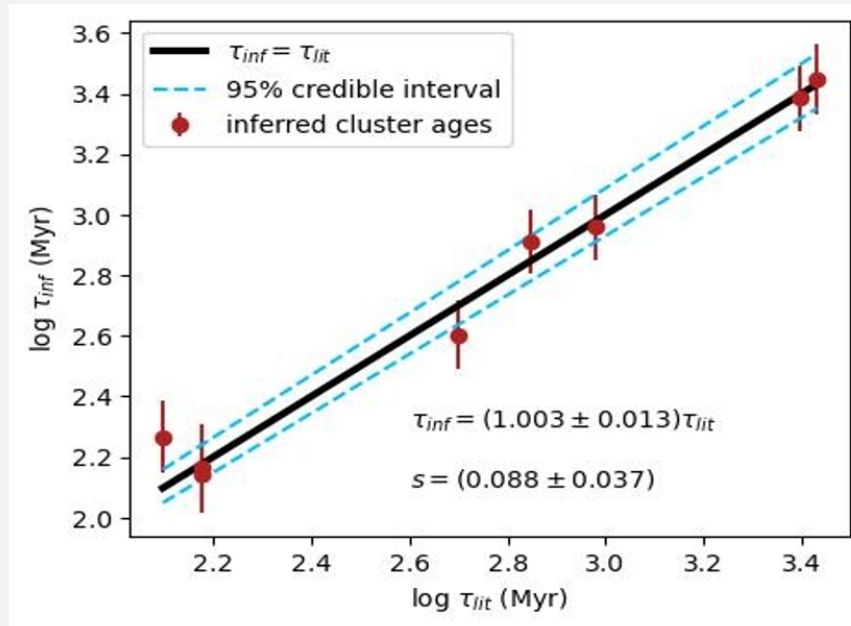
Figure 58. Failure case for summary question-answer pair generation.

Minicpm: The top plot is a contour plot showing the distribution of the absolute magnitude (M_g) and the standard deviation in absolute magnitude (σ_g) for two different groups, LV and Virgo. The contours represent 68%, 95%, and 99% confidence intervals, with the innermost line indicating the highest confidence level. The bottom plots are histograms displaying the number of galaxies within each group along the M_g axis, alongside a red dashed curve that represents a fit to the data. Both groups have their mean (μ_g) and standard deviation (σ_g) values provided, with LV having a slightly higher mean and standard deviation compared to Virgo. The shaded areas on the right side indicate the range from -7.2 to -6.6 in absolute magnitude, which may correspond to observational limits or another relevant parameter set by the study's methodology. (Incomplete answer, not specifying which panel corresponds to the LV and Virgo histograms.)

Pixtral-large: The chart consists of three panels. The top panel is a contour plot showing the relationship between the absolute magnitude (M_g) and the standard deviation (σ_g) for a dataset, with overlapping green and brown contours indicating density regions. The middle and bottom panels are histograms displaying the distribution of M_g for two different datasets labeled "LV" and "Virgo," respectively. Each histogram includes a red dashed line representing a fitted Gaussian distribution. The mean (μ_g) and standard deviation (σ_g) values with uncertainties are provided for each dataset. Vertical orange lines with shaded regions indicate specific ranges of interest. The histograms show the total number of occurrences for each M_g bin, with error bars indicating variability. (Incomplete answer, not clearly defining the confidence regions for the GCLF parameters.)

Deepseek-janus-pro-7b: The image consists of three panels. The top panel is a scatter plot with contours showing the relationship between (σ_8) and (M_k) . The middle panel is a histogram of (M_k) with a red dashed line representing a fitted distribution, along with error bars and a vertical shaded region. The bottom panel is another histogram of (M_k) with a similar red dashed line, error bars, and a vertical shaded region. The histograms are labeled "LV" and "Virgo," with corresponding mean values and standard deviations. The vertical shaded regions in the histograms indicate a range of interest. (Incomplete answer, missing the description of the vertical dashed lines in the histogram.)

Example



Question:

Generate a chart description that aims at presenting all the visual elements of the plot.

Answer:

The figure shows the accuracy of inferred cluster ages versus literature ages. The black line represents a 1:1 relationship, with the 95% credible interval in blue dashed lines and inferred cluster ages as red points.

GPT-4o: The chart is a scatter plot with a linear regression line. The x-axis represents "log τ_{fit} (Myr)" ranging from 2.2 to 3.4, and the y-axis represents "log τ_{inf} (Myr)" ranging from 2.0 to 3.6. Red dots with error bars indicate inferred cluster ages. A solid black line represents the linear fit (τ_{inf} = τ_{fit}), and two dashed blue lines show the 95% credible interval. The equation of the fit is τ_{inf} = (1.003 ± 0.013)τ_{fit}, with a scatter (s) of 0.088 ± 0.037. A legend in the top left corner explains the visual elements.

Figure 59. Failure case for summary question-answer pair generation.

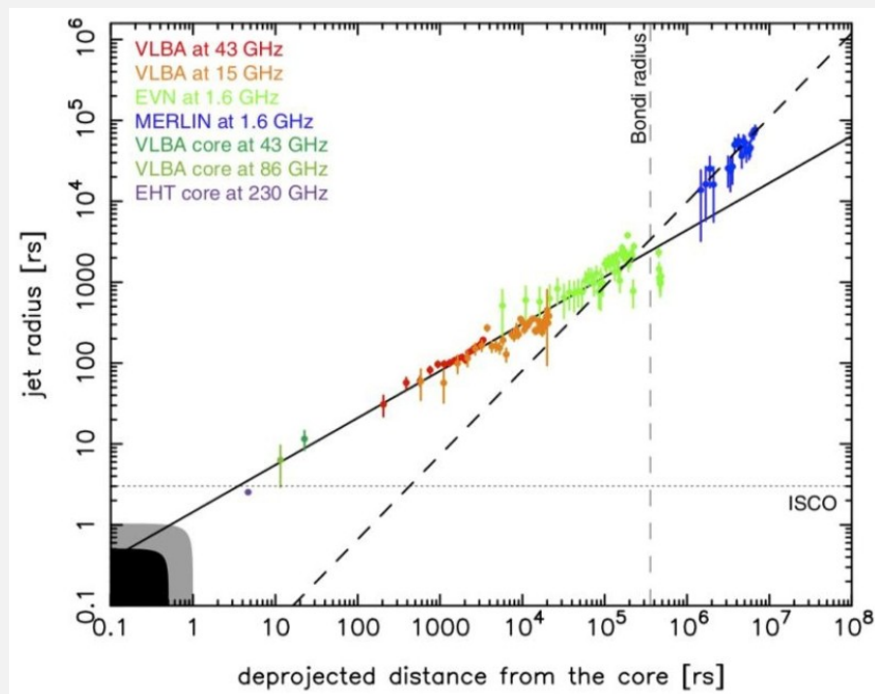
Minicpm: The chart displays a relationship between two variables, with the x-axis labeled as " $\log \tau_{\text{it}}$ " (in Myr) and the y-axis labeled as " $\log \tau_{\text{inf}}$ " (in Myr). The data points are represented by red circles, each accompanied by error bars indicating a 95% credible interval. A solid black line represents an inferred linear regression fit to these data points, suggesting that $\log \tau_{\text{inf}}$ is proportional to $\log \tau_{\text{it}}$. There's also a formula for the slope of the regression line ($s = (0.088 \pm 0.037)$) provided at the bottom right corner of the plot.

Pixtral-large: The chart is a scatter plot comparing inferred cluster ages ($\log \tau_{\text{inf}}$ in Myr) to literature ages ($\log \tau_{\text{lit}}$ in Myr). The x-axis represents the logarithm of literature ages, while the y-axis represents the logarithm of inferred ages. Red dots indicate the inferred cluster ages with error bars showing uncertainties. A solid black line represents the line of equality ($\tau_{\text{inf}} = \tau_{\text{lit}}$), and dashed blue lines denote the 95% credible interval. The plot includes an equation ($\tau_{\text{inf}} = (1.003 \pm 0.013)\tau_{\text{lit}}$) and a slope value ($s = 0.088 \pm 0.037$), indicating a close agreement between inferred and literature ages, with a slight positive bias.

Deepseek-janus-pro-7b: The chart is a log-log plot showing the relationship between the logarithm of cluster ages ($\log \tau_{\text{cl}}$) and the logarithm of cluster ages ($\log \tau_{\text{cl}}$). The x-axis represents $\log \tau_{\text{cl}}$ (Myr), while the y-axis represents $\log \tau_{\text{cl}}$ (Myr). The data points, marked with red circles, represent inferred cluster ages. A black solid line indicates the best-fit linear relationship, with the equation $T_{\text{int}} = (1.003 \pm 0.013)T_{\text{cl}}$. The blue dashed line shows the 95% credible interval, and the error bars on the data points indicate uncertainties. The slope of the line is $s = (0.088 \pm 0.037)$, suggesting a linear relationship between the variables.

Figure 59. Failure case for summary question-answer pair generation. (Continued)

Example



Question:

How does the relationship between jet radius and distance from the core change as we move from smaller to larger scales, and what does this suggest about the jet's structure?

Answer:

The graph shows the jet radius increases more slowly than the distance from the core, indicating collimation. At larger scales, the relationship becomes more linear, suggesting the jet becomes less collimated and accelerates. This change in structure supports the understanding of jet dynamics in M87.

GPT-4o: As the distance from the core increases, the jet radius expands **linearly**, suggesting a **conical structure**. This **linear relationship** indicates a **steady expansion** of the jet, maintaining a **consistent opening angle** across different scales.

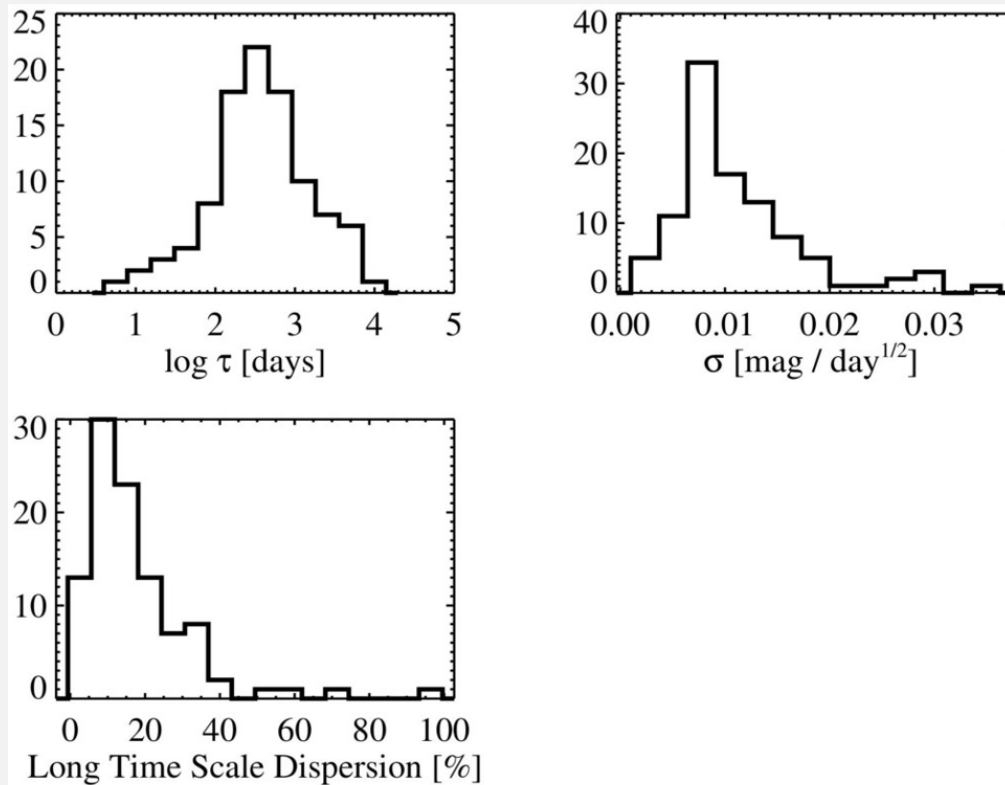
Minicpm: As we move from smaller to larger scales, the data points generally follow a trend that suggests an increase in jet radius with increasing distance from the core. This implies that the jet's structure may be more extended and diffuse at larger distances from the central source, potentially indicating regions of **lower density or less energetic material further out. (...)**

Pixtral-large: The jet radius increases with the deprojected distance from the core, following a power-law relationship. This suggests that the jet expands as it moves away from the core, indicating a **conical or parabolic structure**. The data points from different frequencies align with this trend, reinforcing the jet's expanding nature.

Deepseek-janus-pro-7b: The relationship between jet radius and distance from the core is linear on a log-log scale, indicating a power-law relationship. As the distance increases, the jet radius also increases, suggesting that the jet's structure is consistent across different scales, with the core being the central region and the jet expanding outward. (...**Incompleted answer, no description on larger scale.**)

Figure 60. Failure case for KB-Inference question-answer pair generation. (Continued)

Example



Question:

How does the distribution of characteristic time scales in the graph relate to the stochastic process underlying quasar variability?

Answer:

The graph shows a wide range of characteristic time scales from 10 to 10,000 days ($\log \tau$ from 1 to 4), with a peak around 540 days ($\log \tau \approx 2.7$). This distribution suggests that quasar variability occurs across multiple timescales, consistent with a single stochastic process driving both short and long-term fluctuations.

GPT-4o: The distribution of characteristic time scales suggests that quasar variability is driven by a stochastic process with a dominant timescale around **100 days**, indicating a random walk or damped random walk process, where variability is more pronounced over intermediate timescales.

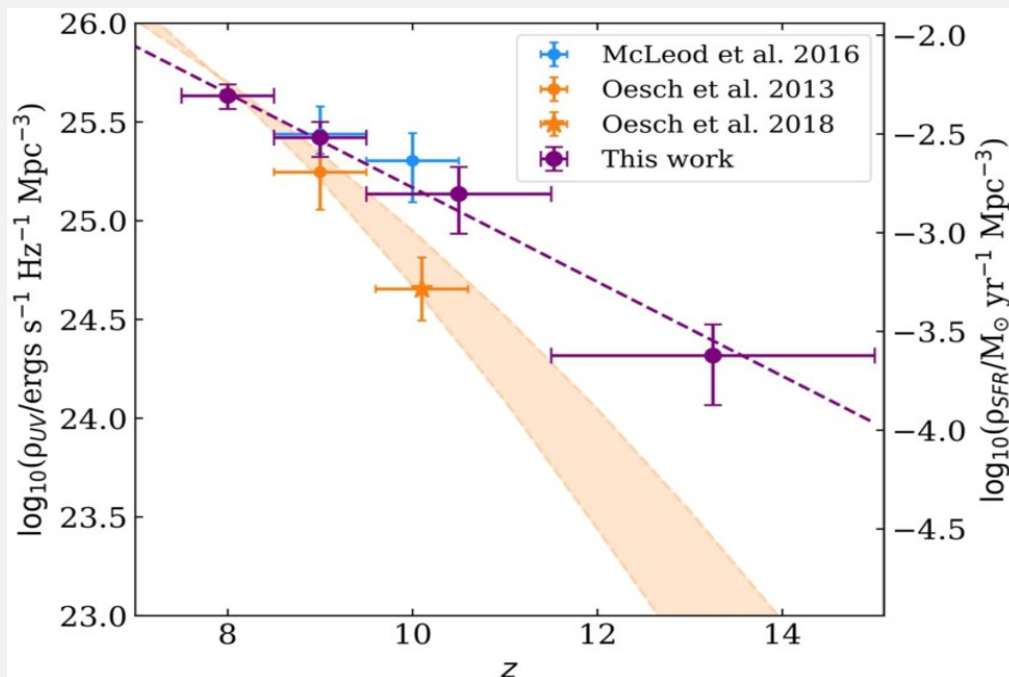
Minicpm: The distribution of characteristic time scales indicates a broad range of variability times, which is typical for stochastic processes. This suggests that the quasar's variability is likely driven by multiple underlying mechanisms with different timescales, contributing to its overall variability. (... No specific data from the chart.)

Pixtral-large: The distribution of characteristic time scales ($\log \tau$ [days]) peaks around 2-3 log days, suggesting that quasar variability is dominated by processes with time scales of approximately **100-1000 days**. This indicates a typical timescale for the underlying stochastic process driving quasar variability.

Deepseek-janus-pro-7b: The distribution of characteristic time scales in the graph shows that most variability occurs within **a short time frame**, indicating that the stochastic process underlying quasar variability is likely to be **short-term** and non-stationary.

Figure 61. Failure case for KB-Inference question-answer pair generation. (Continued)

Example



Question:

How does the trend in star formation rate density at high redshifts ($z > 8$) in this study compare to previous findings, and what implications does this have for our understanding of early galaxy evolution?

Answer:

The new data shows a more gradual decline in star formation rate density at high redshifts compared to earlier studies, particularly Oesch et al. 2018. This suggests a more continuous and steady evolution of early galaxies, rather than a rapid drop-off, providing new insights into the process of galaxy formation in the early universe.

GPT-4o: This study shows a higher star formation rate density at high redshifts ($z > 8$) compared to previous findings, suggesting **more active** early galaxy formation. This implies that galaxies formed and evolved earlier than previously thought, impacting our understanding of cosmic reionization and early universe structure formation.

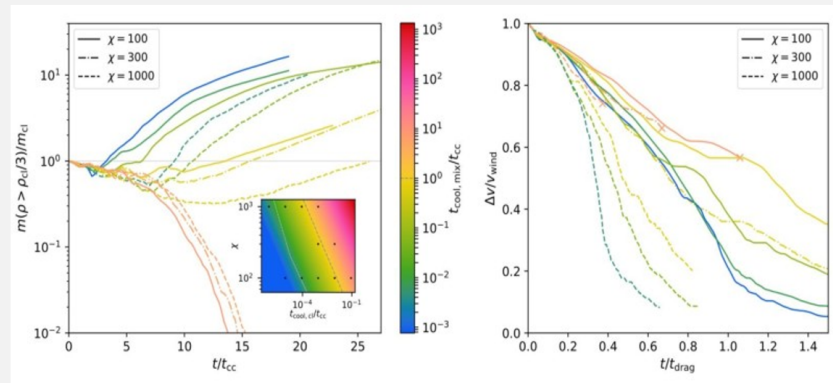
Minicpm: The trend in star formation rate density at high redshifts ($z > 8$) in this study is **consistent with previous findings**, as indicated by the **overlapping data points and similar slopes**. This suggests that the early universe had a stable environment for star formation, supporting models of continuous galaxy evolution without significant disruptions during the cosmic epoch of reionization.

Pixtral-large: The trend in this study (purple) shows a decline in star formation rate density at high redshifts ($z > 8$), **consistent with previous findings** (blue and orange). This suggests that star formation activity decreases in the early universe, implying that early galaxy evolution may have been less vigorous than previously thought.

Deepseek-janus-pro-7b: The trend in star formation rate density at high redshifts ($z > 8$) in this study **shows a steeper decline** compared to previous findings by McLeod et al. 2016 and Oesch et al. 2013, as indicated by the purple data points and the dashed line. This suggests that early galaxies evolve **more rapidly** in terms of their star formation rates, implying a **more rapid** quenching of star formation in high-redshift galaxies.

Figure 62. Failure case for KB-Inference question-answer pair generation. (Continued)

Example



Question:

Provide the most important conclusion or inference from this chart.

Answer:

The figure illustrates the mass evolution and velocity differences of gas clouds with varying densities and cooling times. In the left panel, clouds with shorter cooling times (blue/green lines) show significant mass growth, exceeding their initial mass. Conversely, clouds with longer cooling times (red/orange lines) experience mass loss. The right panel demonstrates that velocity differences between hot and cold phases decrease more rapidly for denser clouds (dashed lines) compared to less dense ones (solid lines). These trends align with the theoretical predictions about the relationship between cooling efficiency and cloud mass growth in mixed warm gas environments.

GPT-4o: The chart consists of two panels showing different aspects of a physical system characterized by the parameter χ (chi), with values of 100, 300, and 1000, represented by different line styles (solid, dashed, and dotted lines, respectively). The color of the lines corresponds to the ratio $(t_{cool, mix})/t_{cc}$, as indicated by the color bar. 1. **Left Panel**: This panel plots the normalized mass $(m(\rho > \rho_{cl}/3)/m_{cl})$ against the normalized time (t/t_{cc}) . - For all values of χ , the mass initially decreases, reaching a minimum before increasing again. - The rate of increase and the final mass value depend on both χ and the color-coded parameter $(t_{cool, mix})/t_{cc}$. - **Higher χ values tend to show a slower initial decrease and a more pronounced increase in mass over time.** 2. **Right Panel**: This panel shows the velocity difference $(\Delta v/v_{wind})$ against the normalized time (t/t_{drag}) . - For all χ values, the velocity difference decreases over time. - The rate of decrease is influenced by both χ and the color-coded parameter, with higher χ values generally showing a slower decrease in velocity difference. Overall, the chart illustrates how the mass and velocity characteristics of the system evolve over time, influenced by the parameters χ and $(t_{cool, mix})/t_{cc}$. Higher χ values tend to stabilize the system, resulting in slower changes in both mass and velocity.

Figure 63. Failure case for KB-Summary question-answer pair generation.

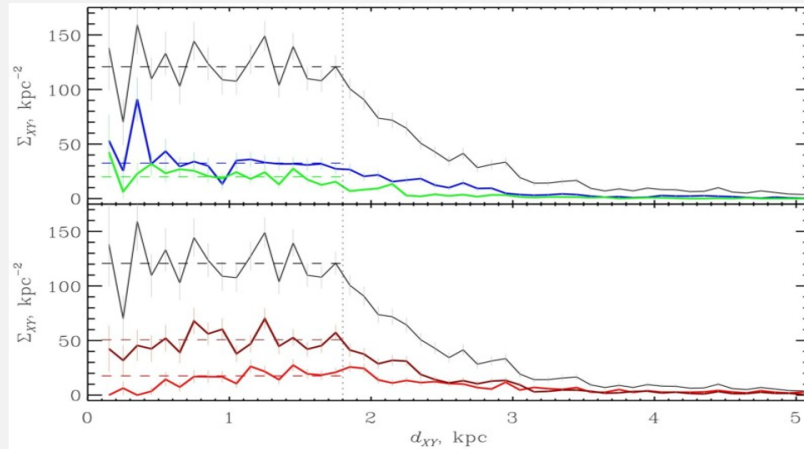
Minicpm: The left panel of the image shows how the mass fraction $(m(\rho > \rho_{cl}/3) / m_{cl})$ evolves over time, normalized by (t_{cc}) , for different values of a parameter (χ) . As time progresses and (χ) increases from 100 to 1000, **the curves generally show a decrease in the mass fraction**. The inset provides a color-coded map of $(t_{cool, cl}/t_{cc})$ versus (x) , indicating variations in cooling times relative to the collapse time. The right panel displays the ratio $(\Delta V / V_{wind})$ as a function of time, normalized by (t_{drag}) . Similar to the left panel, this graph also shows trends for three different values of (χ) . Across all values of (χ) , there is a general decline in the ratio, suggesting that the difference between the volume occupied by the material and the wind's volume decreases over time.

Pixtral-large: The chart consists of **two line graphs**, each depicting different aspects of cloud evolution over time. The left graph shows the evolution of the mass-weighted average density of clouds as a function of time normalized by the cloud crushing time (t/t_{cc}) . The y-axis represents the mass-weighted average density $(m/\rho_{cl} > \rho_{cl}/3)/m_{cl}$ on a logarithmic scale, while the x-axis represents time normalized by t_{cc} . The right graph illustrates the evolution of the mass-weighted average velocity of the clouds as a function of time normalized by the drag time (t/t_{drag}) . The y-axis shows the mass-weighted average velocity $(\Delta v/v_{wind})$ on a linear scale, and the x-axis represents time normalized by t_{drag} . Both graphs include multiple lines representing different overdensity values $(\chi = 100, 300, 1000)$ and cooling times $(t_{cool, mix}/t_{cc})$, with colors corresponding to a color bar indicating the ratio of $t_{cool, mix}/t_{cc}$. **The left graph shows that higher overdensity values and shorter cooling times result in higher average densities over time.** The right graph indicates that higher overdensity values and shorter cooling times lead to slower velocity decay. The inset in the left graph provides a color-coded legend for the cooling times. The key takeaway is that both the density and velocity evolution of clouds are significantly influenced by the overdensity and cooling time, with higher overdensities and shorter cooling times leading to higher densities and slower velocity decay.

Deepseek-janus-pro-7b: The chart consists of two plots. The left plot shows the relationship between $(\frac{m_p}{m_i})$ and $(\Omega_{xi_{KT}})$ for different values of (ν) , with the y-axis on a logarithmic scale. The right plot shows the relationship between $(\frac{m_p}{m_i})$ and $(\Omega_{xi_{KG}})$ for different values of (ν) , again with the y-axis on a logarithmic scale. In both plots, the curves for different values of (ν) (100, 300, 1000) are shown. The general trend is that as $(\Omega_{xi_{KT}})$ or $(\Omega_{xi_{KG}})$ increases, the value of $(\frac{m_p}{m_i})$ decreases. The rate of decrease varies with the value of (ν) . **Higher values of (ν) (e.g., 1000) show a steeper decline in $(\frac{m_p}{m_i})$ compared to lower values of (ν) (e.g., 100).** The color bar in the left plot indicates the range of (ν) , with blue representing lower values and red representing higher values. The right plot also uses a color bar to indicate the values of (ν) , but the scale is different. Overall, the charts illustrate how the mass ratio $(\frac{m_p}{m_i})$ changes with different parameters $(\Omega_{xi_{KT}})$ and $(\Omega_{xi_{KG}})$ for varying values of (ν) . **(Incomplete answer, missing the description of the right panel.)**

Figure 63. Failure case for KB-Summary question-answer pair generation. (Continued)

Example



Question:

Provide the most important conclusion or inference from this chart.

Answer:

The figure illustrates the distribution of star cluster surface density across different distances from the Sun. It shows a consistent density for clusters up to about 1.8 kpc, indicated by a vertical dotted line. Beyond this point, the density decreases significantly. The graph displays data for clusters of various ages, represented by different colors. Younger clusters (blue and green lines) show higher densities closer to the Sun, while older clusters (brown and red lines) have more uniform distributions. This comprehensive representation of cluster populations at different distances and ages demonstrates the thoroughness of the survey within the specified range.

GPT-4o: The chart displays two panels with similar trends, showing a measure labeled Σ_{xy} (in kpc^{-2}) plotted against d_{xy} (in kpc). In both panels, the black line represents the highest values, starting above 100 kpc^{-2} and gradually decreasing as d_{xy} increases, with noticeable fluctuations. The colored lines (blue and green in the top panel, red in the bottom panel) start at lower values and also decrease with increasing d_{xy} , but they remain consistently below the black line. The dashed lines indicate some form of average or baseline for each color. Overall, the trend shows a decrease in Σ_{xy} with increasing d_{xy} , with the black line consistently having the highest values and the colored lines showing similar decreasing patterns but at lower magnitudes. (Incomplete answer, missing the description of the vertical dotted line, does not explicitly state that different colors represent star clusters of different ages.)

Figure 64. Failure case for KB-Summary question-answer pair generation.

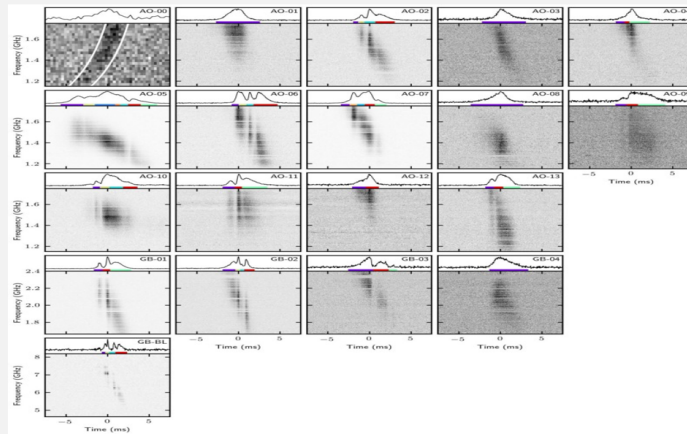
Minicpm: The chart displays two sets of data, each plotted against the distance (d_{XY}) in kiloparsecs (kpc). The upper plot shows three different lines with varying levels of fluctuation across the range of distances. The black line has significant peaks and troughs, suggesting variability or noise at higher distances. The blue and green lines show less variation but still exhibit some fluctuations. In contrast, the lower plot features four distinct lines, with the red and brown lines showing more pronounced and consistent trends compared to the dashed and solid lines. Overall, the charts indicate that the values of (Σ_{XY}) vary depending on the distance and possibly other factors not depicted here. (Incomplete answer, missing the meaning of colors, only describing the fluctuations of the curves without explaining the distribution differences between younger clusters (blue, green) and older clusters (brown, red), missing to emphasize that it represents the highest overall density and the most significant declining trend.)

Pixtral-large: The chart consists of two line graphs, each displaying the surface density of objects as a function of distance from the Sun. The x-axis represents the distance in kiloparsecs (kpc), while the y-axis represents the surface density in objects per square kiloparsec. The top graph shows three data series: black, blue, and green lines, representing different samples of objects. The bottom graph also shows three data series: black, dark red, and red lines, representing different samples of objects. Both graphs include dashed horizontal lines indicating the mean surface density for each sample. The black lines in both graphs show a decreasing trend in surface density with increasing distance, while the other colored lines show more stable trends with some fluctuations. The vertical dotted line at approximately 1.8 kpc marks a significant point where the black line's surface density notably decreases. The key insight is that the surface density of objects generally decreases with distance from the Sun, with variations depending on the sample of objects being considered.

Deepseek-janus-pro-7b: The chart consists of two subplots, each showing the relationship between (d_{DM}) (x-axis) and $(2\pi \cdot \text{kpc}^2)$ (y-axis) for different data sets. The top subplot features three lines: a blue line, a green line, and a black line. The bottom subplot also has three lines: a red line, a green line, and a black line. In both subplots, the black line shows a high initial value and a steep decline as (d_{DM}) increases, eventually stabilizing at a low value. The blue and green lines in both subplots start at lower values and exhibit a more gradual decline, with the blue line generally being higher than the green line. The red lines in both subplots are consistently lower than the other lines and show a less pronounced decline. Overall, the chart suggests that the black line has the highest initial value and the most significant decline, while the red line has the lowest initial value and the least pronounced decline. The blue and green lines fall in between these two extremes. (Incomplete answer, missing the description of the vertical dotted line)

Figure 64. Failure case for KB-Summary question-answer pair generation. (Continued)

Example



Question:

Provide the most important conclusion or inference from this chart.

Answer:

The figure presents dynamic spectra of multiple bursts from FRB 121102, showcasing complex time-frequency structures. Each burst exhibits unique patterns of sub-bursts with varying bandwidths, typically drifting from higher to lower frequencies over time. The bursts display diverse morphologies, ranging from single, narrow-band emissions to multi-component structures with intricate frequency drifts. This variability in burst characteristics suggests a complex emission mechanism or propagation effects in the source's local environment, highlighting the intricate nature of FRB 121102's burst behavior across different frequency ranges and time scales.

GPT-4o: The chart displays a series of spectrograms, each representing a different observation labeled from AO-00 to AO-13 and GB-01 to GB-BL. The spectrograms show frequency on the y-axis and time on the x-axis, with varying intensity levels depicted in grayscale. Key characteristics include: 1. ****Frequency Range****: The AO series covers a frequency range from 1.2 GHz to 1.6 GHz, while the GB series spans from 2.2 GHz to 2.8 GHz, with GB-BL extending up to 8 GHz. 2. ****Signal Patterns****: Most spectrograms exhibit vertical streaks, indicating bursts or pulses at specific frequencies over short time intervals. 3. ****Intensity Variation****: The intensity of the signals varies across different observations, with some showing more pronounced and darker streaks, suggesting stronger signals. 4. ****Time Alignment****: The signals are centered around time zero, with symmetrical patterns on either side, indicating a focus on the burst event. 5. ****Diversity in Signal Structure****: There is a noticeable diversity in the structure and clarity of the signals across different observations, suggesting variability in the source or conditions of the observations. Overall, the chart highlights the detection of transient signals across different frequency bands and observations, with variations in intensity and structure. (Incomplete answer, doesn't mention the complex time-frequency structures or the varying bandwidths of sub-bursts. The standard answer emphasizes diverse morphologies, such as sub-bursts with varying bandwidths and frequency drifts.)

Figure 65. Failure case for KB-Summary question-answer pair generation.

Minicpm: The data shows a series of spectral measurements with varying intensity and frequency over time, indicating different conditions or events. The spectral analysis across the rows suggests fluctuations in signal strength and characteristics, potentially related to specific operational states labeled as AO-00 through AO-13 and GB-01 through GB-04. (Incomplete answer, doesn't describe the complexity and variety of burst morphologies, nor does it indicate frequency drifts or mention the complex nature of FRB 121102's bursts.)

Pixtral-large: The chart is a collection of dynamic spectra plots, each representing a different burst event. The x-axis denotes time in milliseconds (ms), ranging from -5 to 5 ms, while the y-axis represents frequency in gigahertz (GHz), with varying ranges depending on the plot. Each subplot includes a grayscale heatmap showing the intensity of the signal over time and frequency, with darker areas indicating higher intensity. Above each heatmap, there is a line plot showing the frequency-averaged burst profile, with colored bars indicating different time intervals: blue for the pre-burst interval, red for the burst interval, and green for the post-burst interval. The data series in the heatmaps show the evolution of the signal intensity over time and frequency, while the line plots provide a summary of the burst's temporal profile. Notable trends include the presence of distinct bursts around the 0 ms mark in most plots, with varying intensities and frequency ranges. The bursts appear as vertical streaks in the heatmaps, indicating a rapid change in signal intensity over a short period. The line plots generally show a peak corresponding to the burst interval, highlighting the burst's temporal localization. The key takeaway is the clear visualization of burst events across different frequencies and times, with the dynamic spectra and averaged profiles providing a comprehensive view of each burst's characteristics. (Incomplete answer, the answer fails to highlight the complexity in time-frequency structure and varying bandwidths, which are essential aspects mentioned in the standard answer.)

Deepseek-janus-pro-7b: This chart consists of multiple subplots, each showing the relationship between frequency and time for different datasets. The datasets are labeled as A0, A0/2, A0/3, A0/4, A0/5, A0/6, A0/7, A0/8, A0/9, A0/10, A0/11, A0/12, A0/13, A0/14, A0/15, and GB. 1. ****A0 Dataset**:** The first row shows the A0 dataset, which has a distinct pattern with a peak at a specific frequency and a gradual decline in frequency as time progresses. 2. ****A0/2, A0/3, A0/4, A0/5, A0/6, A0/7, A0/8, A0/9, A0/10, A0/11, A0/12, A0/13, A0/14, A0/15**:** These subplots show variations of the A0 dataset with different parameters or conditions. The patterns are similar, with a peak at a specific frequency and a decline over time. 3. ****GB Dataset**:** The last row shows the GB dataset, which has a different pattern compared to the A0 dataset. The frequency decreases over time, but the decline is more gradual and less pronounced than in the A0 dataset. Overall, the chart demonstrates that the A0 dataset has a distinct peak at a specific frequency, which gradually declines over time. The variations of the A0 dataset with different parameters or conditions maintain this trend, while the GB dataset shows a different pattern with a more gradual decline in frequency over time. (Incomplete answer, doesn't mention the sub-bursts with varying bandwidths, the drift in frequency, or the variability of bursts across different time scales and frequencies, which are key aspects of the standard answer.)

Figure 65. Failure case for KB-Summary question-answer pair generation. (Continued)